

DESIGN AND MANUFACTURE OF A LINEAR FRESNEL REFLECTOR PROTOTYPE FOR COFFEE DRYING APPLICATIONS IN PUERTO RICO

by

LUIS ALEXIS DE JESÚS DIAZ

A project report submitted in partial fulfillment of the requirements for the degree of

MASTER OF ENGINEERING
in
MECHANICAL ENGINEERING

UNIVERSITY OF PUERTO RICO
MAYAGÜEZ CAMPUS
2014

Approved by:

Agustín Irizarry Rivera, Ph.D, P.E.
President, Graduate Committee

Date

Francisco Rodríguez, Ph.D
Member, Graduate Committee

Date

David Serrano, Ph.D
Member, Graduate Committee

Date

Carlos Marín, Ph. D
Graduate School Representative

Date

Ricky Valentín, Ph.D
Chairperson of the Department

Date

Abstract

DESIGN AND MANUFACTURE OF A LINEAR FRESNEL REFLECTOR PROTOTYPE FOR COFFEE DRYING APPLICATIONS IN PUERTO RICO

By

Luis A. De Jesús Díaz

December 2014

Chair: Dr. Agustín Irizarry Rivera

Major Department: Mechanical Engineering

The need and desire to use renewable, sustainable, and efficient energy have led to increased research in this field as the long term consequences of not doing so will affect the environment. As an alternative to drying particulate materials using gas and electricity we decided to design, manufacture, and evaluate the performance characteristics of two air collectors for a Linear Fresnel Reflector (LFR) prototype, intended to dry ripe coffee beans to a desired temperature of 50 °C.

A steady-state thermal network analysis and computational modeling techniques were conducted to predict the thermal performance of the desired collectors. They were manufactured and assembled along with the optical frame of the prototype in order to carry out the required experiments to test the system.

The thermal network analysis and that of the computation modeling for one of the designs agreed with one another. The second design was then analyzed by computational model and showed a better performance than the first collector. The experiments showed that both collectors reached the desired air temperature at the outlet with the second collector outperforming the first design demonstrating that the LFR might be a viable system to dry coffee beans.

Resumen

DESIGN AND MANUFACTURE OF A LINEAR FRESNEL REFLECTOR PROTOTYPE FOR COFFEE DRYING APPLICATIONS IN PUERTO RICO

By

Luis A. De Jesús Díaz
December 2014

Chair: Dr. Agustín Irizarry Rivera

Major Department: Mechanical Engineering

La necesidad y el deseo de utilizar la energía renovable de forma eficiente ha dado lugar a un aumento en su investigación ya que las consecuencias a largo plazo de no hacerlo afectará al medio ambiente. Como alternativa al secado de materiales particulados utilizando la quema de gas y la electricidad decidimos diseñar, fabricar y evaluar las características térmicas de dos colectores de aire para un prototipo de un Reflector Linear de Fresnel (LFR) destinado a secar los granos de café maduros a una temperatura deseada de 50 °C.

Se llevó a cabo un análisis de la red térmica en estado estacionario a la vez que se utilizó técnicas de modelado computacional para predecir el comportamiento térmico de los colectores deseados. Estos fueron fabricados y montados junto con el marco óptico del prototipo con el fin de llevar a cabo los experimentos requeridos para probar el sistema.

Los resultados del análisis de la red térmica y la de la modelización computacional para uno de los diseños fueron bien similares. Con esto, el segundo diseño fue analizado por el modelo computacional y mostró un mejor rendimiento térmico que el primer colector. Los experimentos mostraron que ambos colectores alcanzar la temperatura de aire deseada, con el segundo colector superando el primer diseño, lo cual demuestra que el LFR podría ser un sistema viable para secar granos de café.

Copyright © 2014

By

Luis A. De Jesús Díaz

A dedication to my parents, Luis Alfredo De Jesus Diaz and Gloria Diaz Vila, for their unconditional love and support throughout my life. Thank you for all your lessons and good wishes. And to my wife, Julian Andrea Bueno Vera, whom have been a big motivation throughout this process. Thank you for everything.

Acknowledgement

First of all I want to extend my sincere gratitude to the University of Puerto Rico / Mayagüez Campus specifically to the departments of Mechanical and Electrical Engineering who gave me the opportunity to be a member of this prestigious family and filled me with knowledge to face new professional challenges.

Thanks for the continued support of my advisor Dr. Agustín Irizarry Rivera that besides being my biggest support in the academic field he always behaved as a colleague and friend. Adding to this, I want to give thanks to my team, with the lead of Carlos Garcia, who contributed in one way or another in the formation of this manuscript.

Finally, I deeply appreciate the most important things in my life, my family, headed by my father, Alfredo De Jesus, and my mother, Gloria Diaz, as well as my brother and sister, and my friends Jorge Acosta, Freddy Hernandez, and Francisco Valentín which I always received a word of encouragement and motivation during this process.

Thanks to all who contributed from a smile to the most outstanding scientific contribution in this work. It remains for me to say good luck and thanks again to the people who support me “¡antes, ahora, y siempre, Colegio!”.

Table of Contents

I.	Introduction.....	1
II.	Theoretical Background	3
2.1	Solar energy.....	3
2.1.1	Concentrating solar thermal systems.....	4
2.1.2	Thermal Radiation	6
2.1.3	Solar radiation - Definition	10
2.1.4	Solar radiation – Sun’s Position.....	12
2.1.5	Solar radiation - beam and diffuse radiation	14
2.1.6	Solar radiation - Incident on a the mirrors.....	16
2.1.7	Solar Tracking	17
2.2	Thermal conduction	20
2.3	Thermal convection.....	20
2.4	Numerical Simulation	23
2.4.1	Numerical simulation - Finite volume method.....	24
2.4.2	Numerical simulation - Reynolds-Averaged Navier-Stokes turbulence model.....	25
2.4.3	Numerical simulation - $k - \epsilon$ model.....	26
2.4.4	Numerical simulation – Realizable $k - \epsilon$ model.....	27
2.4.5	Numerical simulation – Radiation	28
III.	Literature Review.....	31
IV.	Objectives.....	38
V.	Method and Results	39
5.1	Design and Manufacture of Linear Fresnel Reflector.....	40
5.2	Radiation and Temperature Measurements.....	43
5.2.1	Weather station measurements	43
5.2.2	Radiation incident on the collector	45
5.3	Solar collector design	46
5.3.1	Solar collector design - Flat-Plate equation formulation	49

5.3.2	Solar Collector design - Computational modeling of the receivers.....	58
5.4	Solar collector design – Collector manufacturing	66
5.5	Experiment and results	70
VI.	Conclusion.....	79
VII.	Appendix.....	80
7.1	Solar Tracking Angles.....	80
7.2	Solar Tracking Algorithm	82
7.3	Solar beam radiation algorithm	84
7.4	Bending and Deformation Calculations.....	89
7.5	EES equations	92
7.6	Input Values for EES and Star CCM+ Simulation	94
VIII.	References.....	95

List of Figures

Figure 1: Linear Fresnel Reflector	5
Figure 2: Spectrum of electromagnetic radiation.....	6
Figure 3: Variation of Extraterrestrial Radiation over the course of a year.....	11
Figure 4: Sun's Geometrical Angles.....	12
Figure 5: Solar Angles.....	17
Figure 6: Figure used for incident angle calculation and the ratio of beam radiation on tilted surface. ...	18
Figure 7: East-West view of the Linear Fresnel Reflector with its mirrors.. ..	19
Figure 8: Turbulent and laminar flow for internal flow.	21
Figure 9: Radiation exchange between two surfaces.	29
Figure 10: Methodology diagram.....	39
Figure 11: Modeled parts using Siemens NX software.	42
Figure 12: Design and manufacture of the frame and optics system.....	43
Figure 13: Weather Station.....	44
Figure 14: Siemens NX design of solar collector: a) Top view, b) Bottom view.....	48
Figure 15: Thermal Network for a collector of 6 tubes, with a glass cover, and insulation in the back and sides of the tubes.....	50
Figure 16: Output temperature vs total mass flow rate plot for the two-inch rectangular tubes design.	53
Figure 17: Output temperature vs velocity inlet plot for the two-inch rectangular tubes design	53
Figure 18: Temperature output vs total mass flow rate plot for the one-inch rectangular tubes design.	54
Figure 19: Temperature output vs velocity inlet for the one-inch rectangular tubes design.....	55
Figure 20: Temperature output vs total mass flow rate for the half-inch rectangular tubes design	55
Figure 21: Temperature output vs velocity inlet for half-inch rectangular tubes design.....	56
Figure 22: Temperature output vs pressure drop for each one-inch rectangular tube in atm.	57
Figure 23: Temperature output vs pressure drop for each half-inch rectangular tube in atm.	57
Figure 24: Three dimensional representation model of the volume mesh.	59
Figure 25: Results for the thermal network analysis for a total mass flow rate of 0.01929 kg/s (0.003215 kg/s for each tube). These results are obtained from the Equations Engineer Solver (EES) software.....	60
Figure 26: Temperature distribution at outlet of each one-inch tube.	61
Figure 27: Shows how the temperature of the air changes when it passes through the tubes.....	61
Figure 28: Air temperature when passing through the tubes, without the geometric outline of the collector.	62
Figure 29: Velocity behavior inside the tubes.....	63
Figure 30: Pressure Drop.....	63
Figure 31: Volume mesh three dimensional representation of the model.	64
Figure 32: Air temperature at the outlet of each tube for the collector that has glass cover on the bottom and at the top.	64
Figure 33: Velocity inside the tube.	65
Figure 34: Pressure drop that occurs inside the tube.....	66
Figure 35: One end of the collector during the process of manufacturing	67
Figure 36: The collector during the process of manufacturing.....	67

Figure 37: Complete assembly of the Linear Fresnel Reflector System.....	68
Figure 38: Solar air collector.	69
Figure 39: Measuring the inlet of the tubes with an anemometer probe.....	70
Figure 40: Collector with a glass cover on the top.....	71
Figure 41: First set of experimental results for the collector with 2 glasses.	72
Figure 42: Second set of experimental results for the collector with 2 glasses.	73
Figure 43: Outlet air temperature and solar radiation data for the first set of experiments two.	74
Figure 44: Outlet air temperature and solar radiation data for the second set of experiments two, with the two cover glass collector.	74
Figure 45: Outlet air temperature and solar radiation data for the first set of experiments three, with the collector with one glass cover, in the bottom.	75
Figure 46: Outlet air temperature and solar radiation data for the second set of experiments three, with the collector with one glass cover, in the bottom.	76
Figure 47: Outlet air temperature and solar radiation data for the first set of experiment four, with the collector with one glass cover, in the bottom.	77
Figure 48: Outlet air temperature and solar radiation data for the second set of experiment four, with the collector with one glass cover, in the bottom.	78

List of Tables

Table 1: Material Properties of Stainless Steel 304 and Aluminum Alloy 6061.....	41
Table 2: Spectral radiative properties for commercial glass	46

I. Introduction

Sustainability is one of the main topics circulating the world today and with it comes the need for renewable energies. When mentioning renewable energy most people think of electric energy; they tend to think of big wind turbines, solar farms, hydroelectric dams that generate electricity for a whole city. Another option is to harness renewable energy at a smaller scale to impact a local community.

Solar energy was the renewable source chosen for the investigation for several reasons. First, it is abundant in Puerto Rico. At the same time it is easier to harvest than other renewable sources in the sense that it is more locally available, it can be harnessed in almost any locality in Puerto Rico. Lastly, this source of energy is inexhaustible, very predictable and if theory related to the sun is known one might be able to manipulate its irradiation for a specific purpose.

In order to use this energy, regardless of its purpose, one has to design a collector, which may differ in technology, to be able to harness it. Many systems have been created over the centuries in order to harness this energy efficiently. These collectors may use the solar energy to generate electricity, as mentioned, heat water, to cook or as in our case to dry organic matter, like coffee.

Coffee has been an important product of Puerto Rico for centuries, since it was introduced to the island, but at this time it is a declining industry [1]. Another motivation for the work is to help this industry providing an alternative method to dry coffee. In Puerto Rico, the drying process is mostly mechanized, using fuel (propane) to produce heat and generate electricity to blow air thru the gas flame. The heated air in turn dries the coffee. An alternative is to use patio solar drying, which takes too long and is labor intensive, or a solar mechanized dryer. Some mechanized dryers have been developed but the literature do not mention a solar concentrator as a system used in this process [2], [3]. If a compromise between the expense of conventional mechanical drying and the time it takes by

patio drying is found by using a Linear Fresnel Reflector (LFR) then this technology might be a viable tool to help the coffee industry.

A Linear Fresnel Reflector is analyzed since its use have been known to be efficient at moderate temperatures [3-4]. Our literature review shows that this technology has not been used in Puerto Rico or in agriculture. Our work is also innovative on its use of air as the working fluid for the Linear Fresnel Reflector system since there is no mention of gases as working fluid for these devices in the literature. Furthermore, the use of uncontaminated heat air to dry coffee should keep the quality of dried coffee above the one obtained by burning gas to heat air.

This document describes the different steps taking to fulfill the objectives of this work. It starts by giving an understanding of the theory behind the system, which is mentioned in Chapter II. This chapter is focused on giving an insight of the three modes of heat transfer, what is a concentrated solar collector, and the important aspects of the Sun's radiation, like its position and how to track it. In addition, it discusses the basic concepts and equations used in the Star-CCM+ software that is used as a tool to help with the design of the collector. Chapter III discusses many articles written by different authors regarding the work done for this report. Here, a brief summary of investigations performed on Linear Fresnel Reflector and Flat-Plate collectors is given. Afterwards, the main objectives that were fulfilled are mentioned to give you, the reader, a better perspective of what the final goal of the work is about.

The method used in the study is discussed in Chapter V, where the description of the different steps taken are explained. These steps include the design and manufacture of the optical frame of the Linear Fresnel Reflector, the installation of the weather station, the design and manufacture of two collectors, and the experiments performed to test and compare their results. The final section of the report present our conclusions.

II. Theoretical Background

Heat transfer is the single most important process used in all solar thermal collectors. It is defined as the thermal energy in transit due to a temperature difference [5]. The objective of this chapter is to present some fundamental concepts of the three main types of heat transfer processes, also known as modes. The chapter starts with the definition of the main source of energy used in this work, solar energy. Then, explanation of solar thermal systems is given, specifically concentrated solar collectors. Afterwards, the three modes of heat transfer (thermal radiation, thermal conduction, and convection heat transfer) are explained. Solar radiation concepts are described in depth under thermal radiation.

The order presented in the chapter has the purpose of presenting the reader with the order of how this type of energy is harnessed and transferred to the working fluid of the solar thermal system. This might simplify the understanding of what is heat.

2.1 Solar energy

Solar energy is defined as the radiant energy emitted by the Sun [6]. Solar radiation can be harnessed for it to be used as energy in many different forms for many different uses. Through thermal and photovoltaic processes the energy can be used for electricity generation, water pumping, space heating and cooling purposes, among other uses [7].

Knowing that solar thermal systems is used to convert solar radiation into useful energy, main emphasis is given to study this type of system. It is noteworthy to mention that a solar thermal systems' key element is that of the absorber, where all the solar energy is captured. For many applications it is desirable to increase the amount of energy that enters the absorber, which it is done by concentrating solar radiation to the absorber with the use of reflectors (mirrors). These systems are better explained in the following sections.

2.1.1 Concentrating solar thermal systems

Concentrating solar thermal systems are those that capture solar irradiation for usable thermal energy by the use of optical concentration, normally with mirrors, so that there is a greater intensity of solar radiation available at the absorbing surface [8]. Concentration of solar radiation is necessary for efficient photo-thermal as well as photovoltaic conversion of solar energy [7]. Concentrating Solar Power Systems have been designed in the past several years, such as parabolic dish, linear Fresnel, parabolic trough and central receivers. These systems are mainly used in the energy industry where the majority of beam solar electricity worldwide is generated in nine large solar thermal electric plants in California, with designs and major solar components produced by Luz Industries Israel (LII) [9]. Concentrating type collectors of the conventional design such as compound parabolic and cylindrical parabolic concentrator require very large areas of reflecting surface compared to the actual aperture which contributes to the collection of incident solar radiation[10]. Adding to that is the fact that parabolic concentrators are expensive to manufacture.

On the other hand, and a main objective of this research study, Linear Fresnel Reflector (LFR) concentrators have the advantage of having a relatively simple construction, it is fabricated with narrow flat mirrors and constituent materials (component materials) for its fabrication as well as replacement are readily available in the market [11]. A Linear Fresnel Reflector concentrator (LFR) consists of an array of flat mirror reflectors assembled in a horizontal frame which are aiming all the incident solar rays to an elevated linear absorber as seen in Figure 1. These types of absorber have been around for 50 years, where it was first discussed by Francia in 1963 [12]. Since then, many studies have been made to improve its thermal efficiency and to evaluate its technical feasibility in various applications[9], [13-14].

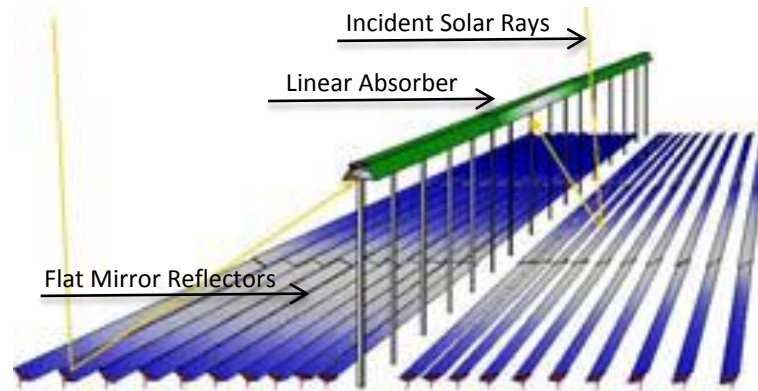


Figure 1: Linear Fresnel Reflector. Manos, S. (2002). Small segment of a large CLFR. Retrieved from <http://www.physics.usyd.edu.au/app/research/solar/clfr.html> . Edited by De Jesús, L. (2014).

The most studied application for a Linear Fresnel Reflector is in energy conversion, either to use it as a pre-heater in a conventional energy production system or as the power plant itself [9], [15], [16], [14], [17], [18]. Another application in which it is used is in absorption refrigeration systems [14], [19]. In both cases each has a heat carrier fluid, which is the component that flows through the receiver and absorbs heat. In many cases water is used, but thermal oils are still the main technology in use (in any linear concentrators). There is also a possibility of using other fluids for cooling the receiver, such as gas and molten salts, but they have been addressed at a very preliminary stage [20].

In any case it is important to study the capacity and performance of the collectors in order to design an efficient collector for a Linear Fresnel Reflector, since the one of the goal of this work is to design a collector for a Linear Fresnel Reflector, which also depends on the solar radiation concentrated in the collector. Many thermal principles are present in the design and analysis of a collector, these are thermal radiation, thermal conduction, and convection; therefore it is necessary to define the fundamental properties that govern the conversion of this solar energy.

To better understand these fundamental concepts they will be explained separately in the foregoing sections.

2.1.2 Thermal Radiation

Thermal Radiation is electromagnetic radiation emitted by a body by virtue of its temperature and at the expense of the molecular and atomic agitation associated with their internal energy. Thus thermal radiation is of the same nature of visible light, x rays, and radio waves, where the difference between them is in their wavelengths and the source of generation [21]. With this in mind, thermal radiation is that radiation detected as heat or light, and is located in the intermediate wavelength range [22]. Figure 2 shows the electromagnetic spectrum and the region of interest, the thermal radiation region. Knowing what is the radiation spectrum, interaction of incident radiant energy with matter can be considered.

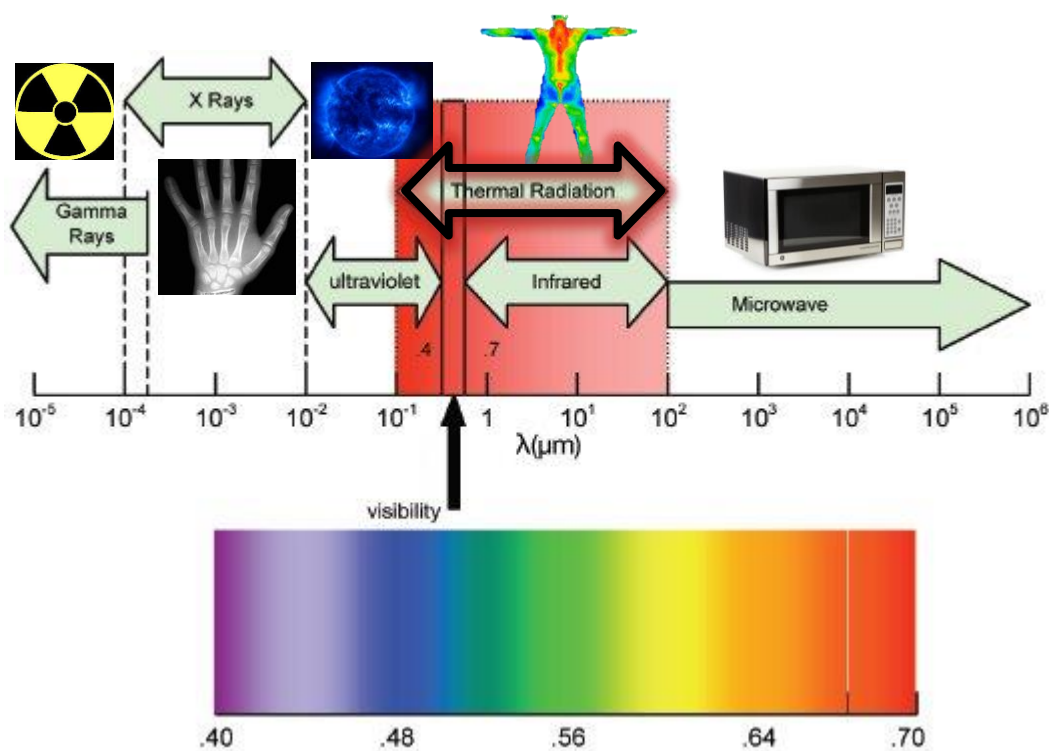


Figure 2: Spectrum of electromagnetic radiation. Scopatz S, Mazzetta J. A portion of the electromagnetic spectrum. Retrieved from http://www.nasatech.com/PTB/features/2009/feat1_0909.html. Edited by De Jesús, L. (2014)

Radiation leaving a surface from any matter can propagate in all possible directions and radiation incident upon any surface may also come from any direction. These directions are important since the

manner in which a surface responds to radiation depends on them. To treat these directional effects it is then important to introduce the concept of radiation intensity, which may be expressed either as $I_{\lambda,e}$ ($\text{W}/\text{m}^2 \cdot \text{sr} \cdot \mu\text{m}$) or I_e ($\text{W}/\text{m}^2 \cdot \text{sr}$). The first expression is called the spectral intensity and depends on the wavelength λ^1 , the latter takes all possible wavelengths into account and is called the total intensity and both may be written as

$$I_{\lambda,e} = \frac{dq_{\lambda}}{dA \cos \theta \sin \theta d\theta d\phi} \quad (\text{II-1})$$

$$I_e = \int_0^{\infty} I_{\lambda,e} d\lambda = \frac{dq}{dA \cos \theta \sin \theta d\theta d\phi} \quad (\text{II-2})$$

where θ and ϕ are the zenith and azimuthal angles, respectively, and $dq_{\lambda} \equiv (dq/d\lambda)$. By rearranging equation (II-1) the spectral radiation flux associated with dA may be written as

$$dq_{\lambda}'' = I_{\lambda,e}(\lambda, \theta, \phi) \cos \theta \sin \theta d\theta d\phi \quad (\text{II-3})$$

by integrating this equation the heat flux associated with emission into any finite solid angle or over any finite wavelength may be determined.

To include emission of radiation of a surface in all directions equation (II-3) may be written as

$$E_{\lambda}(\lambda) = q_{\lambda}''(\lambda) = \int_0^{2\pi} \int_0^{\pi/2} I_{\lambda,e}(\lambda, \theta, \phi) \cos \theta \sin \theta d\theta d\phi \quad (\text{II-4})$$

this is the spectral emissive power E_{λ} ($\text{W}/\text{m}^2 \cdot \mu\text{m}$) and is based on the actual surface area, whereas $I_{\lambda,e}$ is based on the projected area. From here the above integrand may be solved for a diffuse emitter, which is a surface for which the intensity of the emitted radiation is independent of direction, $I_{\lambda,e}(\lambda, \theta, \phi) = I_{\lambda,e}(\lambda)$. Equation (II-4) then becomes, after integration,

$$E_{\lambda}(\lambda) = \pi I_{\lambda,e}(\lambda) \quad (\text{II-5})$$

¹ All nomenclatures with a sub-index λ mean that it depends on wavelength.

for the total emissive power the equation is expressed in equation (II-6).

$$E = \int_0^{\infty} E_{\lambda}(\lambda) d\lambda = \pi I_e \quad (\text{II-6})$$

Another important concept is the radiation that originates from emission and reflection occurring at other surfaces and may be called incident radiation. This radiation will have spectral and directional distributions determined by the spectral intensity $I_{\lambda,i}(\lambda, \theta, \phi)$. This intensity may be related to a radiative flux, termed irradiation, and similar to emission, it is incident in all directions. Following the same set of steps for spectral and total emissive power, spectral and total irradiation is expressed in the following equations.

$$G_{\lambda} = \pi I_{\lambda,i}(\lambda) \quad (\text{II-7})$$

$$G = \pi I_i \quad (\text{II-8})$$

One important behavior that should be discussed is that of a blackbody and will be briefly explained before we can continue, since it is the standard with which to compare the performance of real radiating bodies. A blackbody is an ideal body that allows all the incident radiation to pass into it and internally absorbs all the incident radiation and it is also the best possible emitter of radiant energy, at every wavelength and direction. A blackbody's total emissive power is expressed as

$$E_b = \sigma T^4 \quad (\text{II-9})$$

where σ is the Stefan-Boltzmann constant and has the following numerical value

$$\sigma = 5.670 \times 10^{-8} \text{ W/m}^2 \cdot \text{K}^4 \quad (\text{II-10})$$

knowing that the emission of a blackbody is diffused, it follows that the total intensity associated with a blackbody is

$$I_b = \frac{E_b}{\pi} \quad (\text{II-11})$$

Emission from real surfaces can never emit more radiation than a blackbody at the same temperature. This is why a blackbody is chosen as a reference in describing emission from real surfaces. The ability of a surface to emit radiation in comparison with the ideal emission by a blackbody is defined as the emissivity of the surface. Emissivity can be defined on a spectral, directional, or total basis. Accordingly, spectral, directional emissivity, $\varepsilon_{\lambda,\theta}(\lambda, \theta, \phi, T)$, is

$$\varepsilon_{\lambda,\theta}(\lambda, \theta, \phi, T) = \frac{I_{\lambda,e}(\lambda, \theta, \phi, T)}{I_{\lambda,b}(\lambda, T)} \quad (\text{II-12})$$

where λ and θ designate interest in a specific wavelength and direction for the emissivity. All other definitions of emissivity (spectral, hemispherical emissivity, total, hemispherical emissivity) may be found by substituting the intensities and solving the integrands that define the different emissive powers [5], [21].

Absorption, reflection, and transmission are other important processes that need to be considered in thermal radiation analysis. These processes occur when irradiation interacts with a medium where its radiation balance follows

$$G_{\lambda} = G_{\lambda,ref} + G_{\lambda,abs} + G_{\lambda,tr} \quad (\text{II-13})$$

In general these properties depend on surface material and finish, surface temperature, and the wavelength and direction of the incident radiation. In most engineering applications the medium is opaque to the incident radiation, hence $G_{\lambda,tr} = 0$. It should be known that glass, although transparent to most short wave radiation, is opaque to long wave radiation [5].

Absorptivity is the property that defines the fraction of the irradiation absorbed by a surface. The spectral, hemispherical absorptivity $\alpha_{\lambda}(\lambda)$ is the property mostly used in engineering calculations. Accordingly,

$$\alpha_{\lambda}(\lambda) \equiv \frac{G_{\lambda,abs}}{G_{\lambda}(\lambda)} \quad (II-14)$$

The other process, reflectivity, is a property that determines the fraction of the incident radiation reflected by a surface. This process is inherently bidirectional, which means that it depends on the direction of the incident radiation and on the direction of the reflected radiation. This complication is avoided by working with a reflectivity that represents an integrated average over the hemisphere associated with the reflected radiation. Accordingly, the spectral, directional reflectivity, $\rho_{\lambda,\theta}(\lambda, \theta, \phi)$, is

$$\rho_{\lambda,\theta}(\lambda, \theta, \phi) = \frac{I_{\lambda,i,ref}(\lambda, \theta, \phi)}{I_{\lambda,i}(\lambda, \theta, \phi)} \quad (II-15)$$

As in emissivity, all other definitions may be found by substituting for the intensities and solving the integrands that define the different irradiations [5].

These fundamental definitions of radiation can now help in the understanding of solar radiation. Solar radiation comes from the Sun and is essential to all life on earth, it also has the potential of being used for electricity and process heat through thermal and photovoltaic processes [5]. A basic explanation of solar radiation follows.

2.1.3 Solar radiation - Definition

With an average diameter of 1.39×10^9 m and about 1.5×10^{11} m from earth, the sun emits radiation in the wavelength range of 250 to 3000 nm. It has an effective blackbody temperature of 5777 K, where the temperature in the central interior regions is estimated at 8×10^6 to 40×10^6 K. The energy produced here must be transferred through temperature and density gradients and out to the surface. With this in mind, the emitted solar radiation is then the composite result of the several layers that emit and absorb radiation of various wavelengths (hence, does not function as a blackbody). The total solar radiation reaching the earth's surface is therefore the sum of beam and diffuse contributions [5], which is known as the global horizontal radiation (G_G).

The World Radiation Center indicates that the maximum average solar radiation intensity at the outer surface of the earth's atmosphere is $1,367 \text{ W/m}^2$, G_{sc} , called the solar constant. As it enters the Earth's atmosphere it is divided in several components: beam (direct) and diffuse, as mentioned above, and scattered, absorbed, and reflected (to space) radiation. The diffuse component is the radiation received by the sun after scattering by the atmosphere. It can be composed by the radiation emitted and reflected by the water vapor, gases, and clouds from the atmosphere and from the ground.

Before continuing, it is imperative to mention that the radiation intensity at the outer surface of earth's atmosphere, known as Extraterrestrial Radiation, varies due to the earth-sun distance changes. This effect can be observed in Figure 3. An accurate equation, with 0.01% of uncertainty, to calculate extraterrestrial radiation incident on the plane normal to the radiation is given by equation (II-28).

$$G_{on} = G_{sc} (1.000110 + 0.034221 \cos B + 0.001280 \sin B + 0.000719 \cos 2B + 0.000077 \sin 2B) \quad (\text{II-16})$$

where B is given by equation (II-29), where n is the day of the year, $1 \leq n \leq 365$.

$$B = (n - 1) \frac{360}{365} \quad (\text{II-17})$$

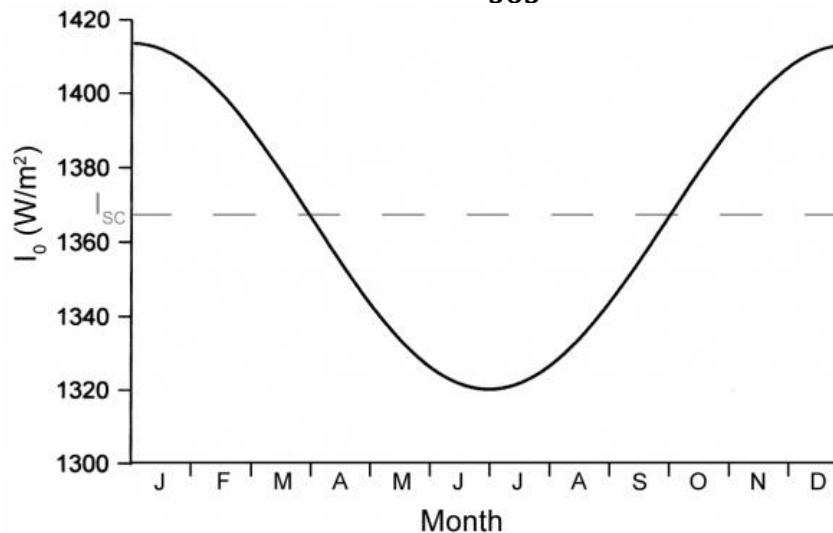


Figure 3: Variation of Extraterrestrial Radiation over the course of a year. Solar energy reaching the earth's surface. The variation in I_0 over the course of a year. Retrieved from <http://www.itacanet.org/the-sun-as-a-source-of-energy/part-2-solar-energy-reaching-the-earths-surface/>.

2.1.4 Solar radiation – Sun’s Position

The solar radiation incident on Earth’s surface and its components can be quantified, to do this an understanding of the Sun’s position is necessary. Figure 4 shows the angles that define the Sun’s position. The zenith (θ_z), declination (δ), solar azimuth (γ_s), and solar altitude (h_s) angles depend heavily on the day of the year, where Earth’s Obliquity (Axial tilt) and the Celestial Equator change continuously when traveling in its orbit around the Sun. Luckily, the human race has been studying this behavior for centuries. This knowledge mixed with technological advances makes it possible to predict its path with very small uncertainties.

A MatLab function written by Vincent Roy [23] is used to compute the sun position, zenith (θ_z) and solar azimuth (γ_s) angles at the observer’s location. This function is an implementation of the algorithm presented by Reda and Andreas (2004) [24] and has an uncertainty of $\pm 0.0003^\circ$. It is based on numerical approximation of astronomical equations of which are explained next.

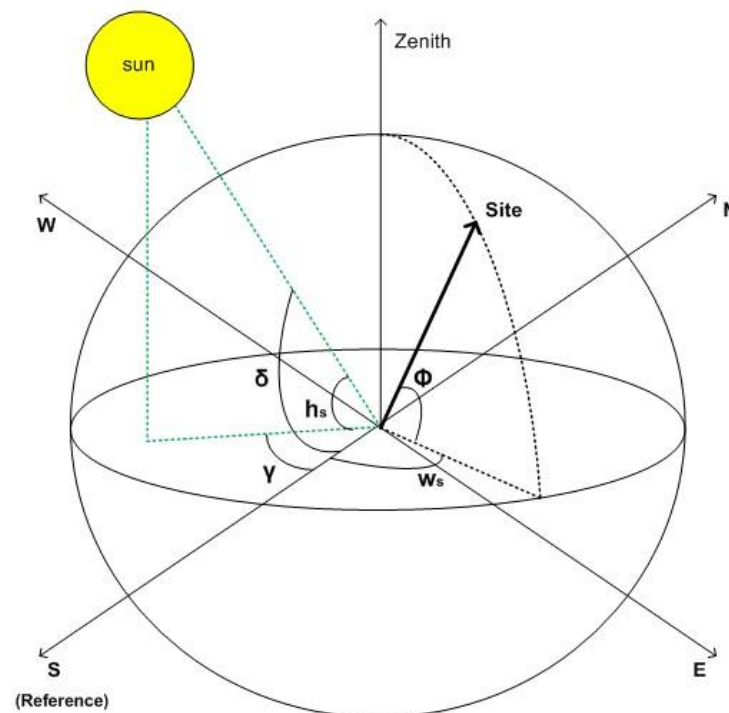


Figure 4: Sun's Geometrical Angles

The solar altitude (h_s) is the angle that lies between the horizontal plane and the Sun's vector. This angle can be calculated as follows²:

$$\sin(h_s) = \sin \phi \sin \delta + \cos \phi \cos \delta \cos \omega_s \quad (\text{II-18})$$

This angle varies from 0 to 90 degrees and it is the complement of the zenith angle. Subsequently, the solar azimuth angle (γ_s) can be defined as the angular displacement from south to the projection of the beam radiation that lies on the horizontal plane. The solar azimuth can be expressed as:

$$\gamma_s = \text{sign}(\omega_s) \left| \cos^{-1} \frac{\cos \theta_z \sin \phi - \sin \delta}{\sin \theta_z \cos \phi} \right| \quad (\text{II-19})$$

where the sign function, $\text{sign}(\omega_s)$, indicates +1 if the hour angle (ω) is positive or -1 if it is negative, and δ is declination. The declination angle can be described as the angle between a line joining the Sun and Earth and the plane of the equator. It is a daily variation where, in the Northern Hemisphere³, its maximum angle is 23.45° at the summer solstice and -23.45° in the winter solstice and it can be calculated by applying the following equation⁴:

$$\delta = 23.45 \sin \left(360 \frac{284+n}{365} \right) \quad (\text{II-20})$$

Accordingly, the hour angle is the angle that positions the sun east or west of the local meridian. The angle increases 15° every hour the Earth rotates on its axis, where morning is negative and the afternoon is positive. The hour angle may be expressed as:

$$\omega = 15 (\text{Solar Time} - 12) \quad (\text{II-21})$$

where *Solar Time* is the time based on the Sun's position in the sky. It is necessary to convert standard time (local time) to solar time for all of the sun-angle relationships. To convert the standard time to

² In all trigonometric functions in this chapter we measure angles in degrees.

³ All equations are focused for the Northern Hemisphere. Although equations are general, careful care should be applied if using these equations for other areas.

⁴ Duffie and Beckman cite another, more precise, equation.

local time it is necessary to implement two corrections, a longitudinal and an equation of time correction. These are implemented in the conversion shown in equation (II-22).

$$\mathbf{Solar\ time = standard\ time + 4 (L_{st} - L_{loc}) + E} \quad (\text{II-22})$$

where L_{st} is the standard meridian for the local time zone, and L_{loc} is the longitude of the location in question. E is the equation of time (in minutes), which is expressed as:

$$\mathbf{E = 229.2 (0.000075 + 0.001868 \cos B - 0.032077 \sin B - 0.014615 \cos 2B - \sin 2B)} \quad (\text{II-23})$$

where B is found using equation (II-17). Note that these two corrections, longitudinal and time equation, are both in minutes and care must be exercised in applying these corrections, more so if using daylight savings.

Considering all the abovementioned angles and definitions, the solar extraterrestrial (outside the atmosphere) radiation incident on a horizontal plane can be calculated by:

$$I_o = \frac{12 * 3600}{\pi} G_{sc} \left(1 + 0.033 \cos \frac{360n}{365} \right) \left[\cos \phi \cos \delta (\sin \omega_2 - \sin \omega_1) + \frac{\pi(\omega_2 - \omega_1)}{180} \sin \phi \sin \delta \right] \quad (\text{II-24})$$

where ω_1 and ω_2 represent the limits of a time period. As mentioned earlier, when the solar radiation enters the atmosphere it is subject to scattering and absorption by the atmosphere causing attenuation of the solar radiation and dividing the solar radiation into beam and diffuse components. It is of great interest to know the radiation that reaches the Earth's surface taking into account the different components that affect it.

2.1.5 Solar radiation - beam and diffuse radiation

Most radiation measurements available are that of global radiation on horizontal surfaces, I , but for

many applications, the diffuse and direct (beam) radiation components, I_d and I_b^5 , respectively, are needed. For this reason, many models have been developed to establish correlations between the diffuse component and various predictors.

The firsts to study this subject, Liu and Jordan (1960)[25], determined a relationship between the diffuse and global radiation on clear days for a horizontal surface, known as the clearness index, k_T . The clearness index is the ratio of the measured solar radiation value to the extraterrestrial solar radiation. This dimensionless index can be defined in different time intervals (eg. monthly, daily, hourly) and can be determined by equation (II-25).

$$k_T = \frac{I}{I_o} \quad (\text{II-25})$$

where I is the global radiation measured by a pyranometer (instrument used to measure solar radiation) and I_o is the extraterrestrial solar radiation.

The clearness index is used in many of the models used to estimate the fractions (components) of the global horizontal radiation, which are diffuse and beam radiation. These models differ from each other in many ways; by their mathematical methods, the type of variables or predictors they use, the quantity of them, among others. To this date there is not a best method to use. Its accuracy may differ from place to place as discussed by Fabienn Lanini [26]. For simplicity, and because the decomposition and explanation of these models is out of the scope of this thesis, the Erbs et al. (1982)[27] correlation is used. This correlation was compared to Orgill and Hollands (1977)[28] and Reindl et al. (1990)[29] and were essentially identical [7], meaning that the correlation produces results that are good for practical purposes. Erbs et al. correlation is as follows:

$$\frac{I_d}{I} = \begin{cases} 1.0 - 0.09k_T & \text{for } k_T \leq 0.22 \\ 0.9511 - 0.1604k_T + 4.388k_T^2 - 4.388k_T^3 + 12.336k_T^4 & \text{for } 0.22 \leq k_T \leq 0.80 \\ 0.165 & \text{for } k_T > 0.8 \end{cases} \quad (\text{II-26})$$

⁵ I is used for energy quantities integrated over an hour (MJ). It may also be defined for a time other than an hour.

where I_d is the diffuse solar radiation. From this equation it is possible to determine the beam radiation on a flat surface, I_b , from a measured global radiation. It is important to mention that for the purpose of this thesis it is of interest to calculate the incident beam radiation that is incident on the tracking mirrors of the Linear Fresnel Reflectors. For this we need the direction from which the beam component reaches the surface of interest, the mirrors.

2.1.6 Solar radiation - Incident on a the mirrors

The mirrors in the Linear Fresnel Reflector redirect the beam solar radiation to the absorbing surface, the collector. When beam solar radiation strikes a mirror at an incident angle it is reflected at an angle equal to the incident angle with respect to the surface normal. For this reason the direct beam radiation, $G_{b,n}$ is needed and is expressed in the following equation (II-27).

$$G_b = G_{b,n} \cos \theta_z \quad (\text{II-27})$$

Here, the zenith angle, θ_z , is the angle of incidence of beam radiation on a horizontal surface, angle between the normal of a horizontal surface and the line to the Sun. The angle of incident is the angle that lies between the beam radiation on the surface and the normal to that surface. For this case the zenith angle, θ_z , is the incident angle for a horizontal flat surface and G_b (or I_b , depending if using rates W/m^2 or energy quantities MJ) is the beam radiation calculated in the previous section. $G_{b,n}$ is the energy flux of the incoming solar radiation normal to its direction.

A concentrating solar collector needs be tracking the sun on a continuous basis since the beam it uses, the direct beam radiation, depends on the zenith angle, which changes constantly through out the day. For this reason, the mirrors should be able to track the sun using the combination of equations already explained in the sections above along with other geometric considerations that is explained the following section.

2.1.7 Solar Tracking

In order to be able to concentrate solar radiation to the absorber in a Linear Fresnel Reflector solar tracking is necessary. This is done in order to capture the direct solar radiation from the sun. This method is best explained in the following section where it explains in more details the different methods of solar tracking and important angles necessary to calculate the sun's position.

Solar tracking can be done in different ways; with sensors or by optical calculations by knowing where the sun is at a certain time and date. In a LFR each mirror row should be positioned depending on the sun's position and should change as the sun changes position. The inclination of these mirrors is calculated by using optical geometry relations combined with the solar position at a moment, where the latter is calculated using a set of astronomical equations. Figure 5 shows the geometric relation of important solar angles used in solar tracking.

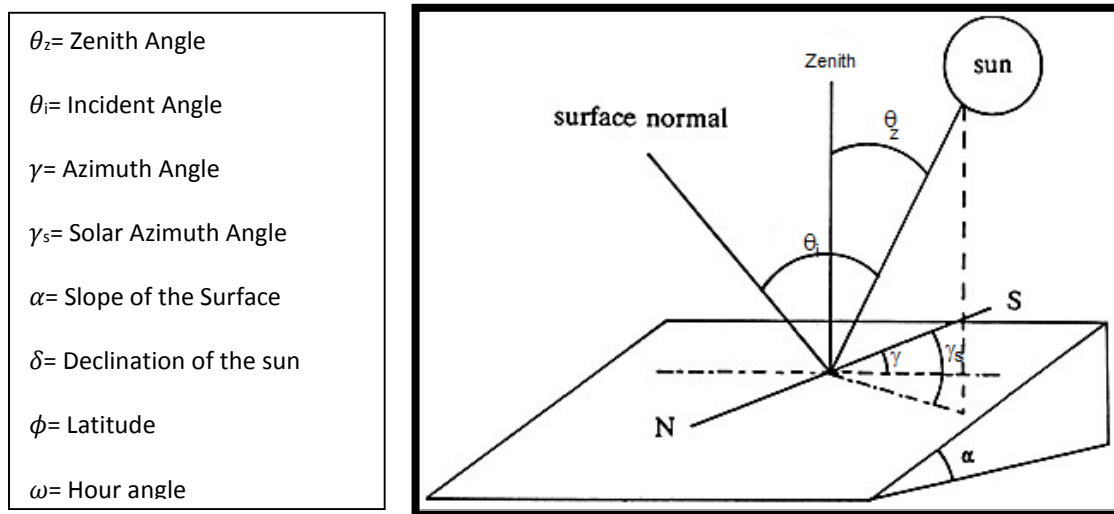


Figure 5: Solar Angles. Jacobsen, A. (1993). Solar incidence angle. Retrieved from <https://tidsskrift.dk/index.php/geografisktidsskrift/article/viewFile/2341/4119>. Edited by De Jesús, L. (2014).

These angles are also related by the following general equation:

$$\cos \theta_i = \sin \delta \sin \phi \cos \alpha - \sin \delta \cos \phi \sin \alpha \cos \gamma + \cos \delta \cos \phi \cos \alpha \cos \omega + \cos \delta \sin \alpha \sin \gamma \sin \omega \quad (\text{II-28})$$

This equation may be simplified depending on various reasons like the hemisphere where the calculation is desired, by how the system is oriented, if the surface is tilted, among others.

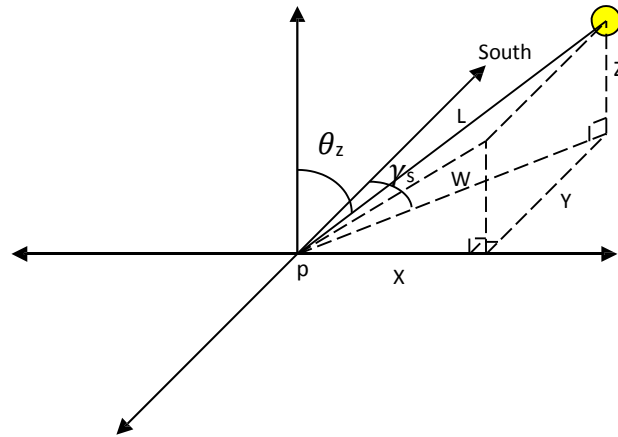


Figure 6: Figure used for incident angle calculation and the ratio of beam radiation on tilted surface. Rivera Jiménez and Correa Torres. (2010). Retrieved from *Diseño de un Sistema Lineal Fresnel*. Edited by De Jesus, L. (2014).

In order to concentrate the beam solar radiation to the Linear Fresnel Reflector's collector the inclination (α) of the mirrors need to be known. The inclination of the mirrors can be calculated by the use of geometric principles using the angles from Figure 6. By changing the plane view of the figure above other angles of interest can be best appreciated, as seen in the figure below.

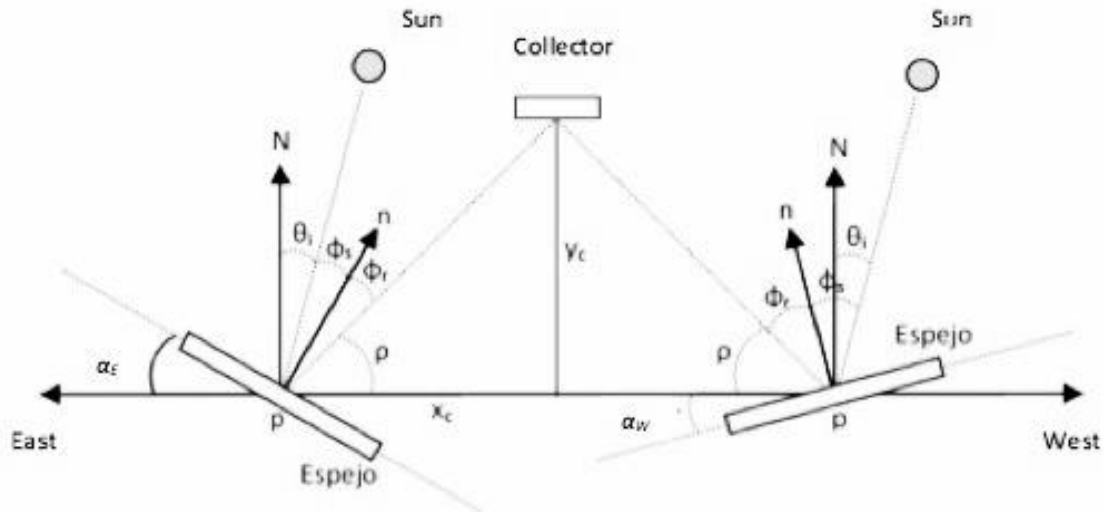


Figure 7: East-West view of the Linear Fresnel Reflector with its mirrors. Rivera Jiménez and Correa Torres. (2010). Retrieved from *Diseño de un Sistema Lineal Fresnel*. Edited by De Jesus, L. (2014).

Figure 7 shows the angles of interest for the inclined mirrors from both sides of the LFR. These angles (from Figure 6 and Figure 7) can be related by the following equations:

$$\tan(\theta_i) = \tan(\theta_z) \sin(\gamma_s) \quad (\text{II-29})$$

$$\alpha_E = \frac{\theta_i - \tan^{-1}\left(\frac{y_c}{x_c}\right) + 90}{2} \quad (\text{II-30})$$

$$\alpha_W = \frac{\theta_i + \tan^{-1}\left(\frac{y_c}{x_c}\right) + 90}{2} \quad (\text{II-31})$$

Where θ_i , α_E , and α_W are the incident angle on the horizontal surface and inclination angle for the mirror positioned on the east and west side, respectively. In the same equations we see y_c and x_c which, respectively, are the vertical and horizontal distance of the mirrors from the collector. The full derivation of these equations can be found in Appendix 7.4. An important note is that the incident angle on the horizontal surface, θ_i , is the zenith angle to be used in equation (II-27) mentioned in the previous section (2.1.6).

Reda's function along with equations (II-29), (II-30), and (II-31) give the inclination angles needed for each mirror at a specific time. These set of equations are written in a MatLab code (Appendix 7.2) that is set up to write the inclination angles for each mirror, for a specific date, for a certain amount of hours (8 hours) every few number of minutes (4). The data written from the MatLab code is then fed to a LabView code that controls the motors that move the mirrors. This will be explained further.

2.2 Thermal conduction

Thermal conduction refers to the heat transfer that occurs across a medium due to temperature gradient, the medium being a solid or a stationary fluid. Conduction can also be viewed as the transfer of energy from the more energetic particles to those of less energetic particles of a substance. This mode of heat transfer is govern by a rate equation known as *Fourier's Law* and is expressed as

$$q_x'' = \frac{q_x}{A} = -k \frac{dT}{dx} \quad (\text{II-32})$$

where k is the proportionality constant known as the thermal conductivity (W/m-K), a material property, and A is the area perpendicular to the direction of the transfer. This equation is a simplified condition, one-dimensional, steady state conduction, where the temperature distribution is deduced as linear, it can be applied to transient, complex geometries for which the nature of the temperature distribution is not evident [5].

2.3 Thermal convection

Convection is heat transfer that occurs between a surface and a moving fluid at different temperatures [5]. Here, the bulk or gross motion of fluid particles is the dominant contributor of the energy transfer. This mode of heat transfer may be classified as forced convection or free, natural, convection. Forced convection is when external forces, such as fans or pumps, cause the flow. Natural convection arises from density differences, caused by temperature gradient, in the fluid.

The rate equation associated with the convection heat transfer process is known as *Newton's Law of Cooling*:

$$q'' = h(T_s - T_\infty) \quad (\text{II-33})$$

h , being the local convection coefficient, and T_s and T_∞ are the surface and fluid temperature, respectively. Likewise, this equation may be integrated to obtain the total heat transfer rate, since q'' and h vary along the surface. By doing so we obtain an average convection coefficient \bar{h} for the entire surface, and the equation is similar to equation (II-33).

An important aspect of convection is whether a fluid motion has a laminar or turbulent boundary layer. A laminar flow has highly ordered flow, whereas a turbulent flow is highly irregular, as observed in Figure 8. The existence of either of these conditions is important to know, since surface friction and convection heat transfer rates depend strongly on them.

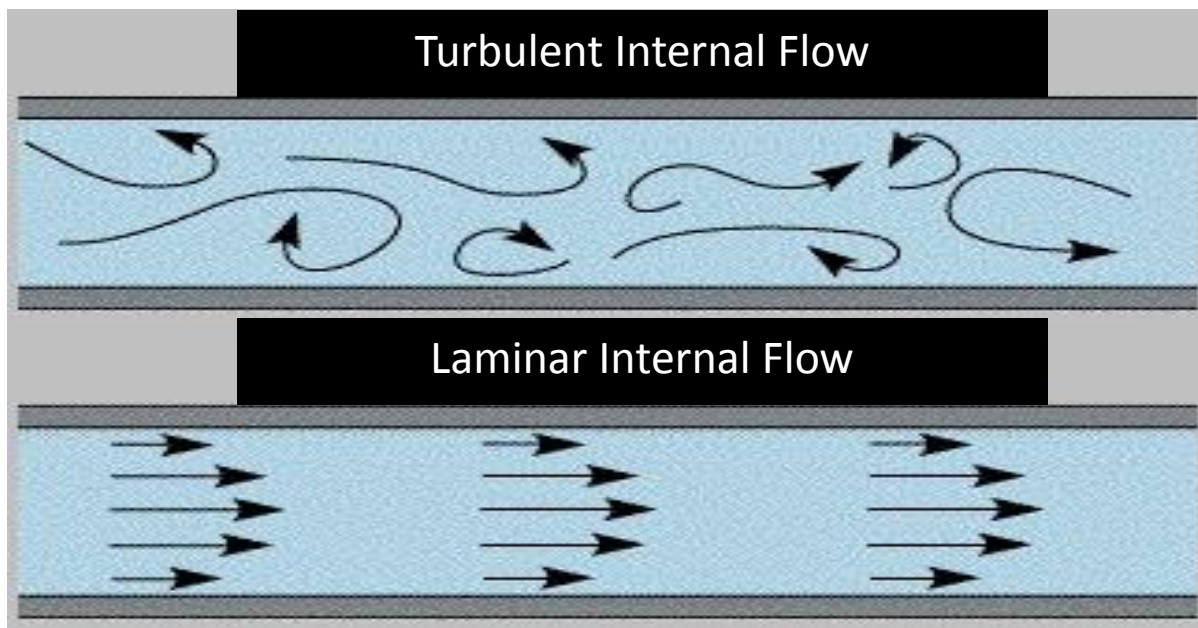


Figure 8: Turbulent and laminar flow for internal flow. University of Cambridge. Hydrodynamics. Retrieved from <http://www.ceb.cam.ac.uk/research/groups/rg-eme/teaching-notes/hydrodynamic-voltammetry>. Edited by De Jesús, L. (2014).

Calculation of this behavior is determined by a dimensionless coefficient called the Reynolds

number, expressed in equation (V-2). For external flows (e.g. flow over a flat plate) values under 10^6 may be considered laminar, this value may be called the critical Reynolds number. Values above this number may be considered turbulent (though it may vary from 10^5 to 3×10^6).

$$Re = \frac{\rho u_{\infty} L}{\mu} \quad (\text{II-34})$$

Many heat transfer books give various correlations to calculate heat transfer coefficients [5], [7]. Correlations are inferred from empirical measurements and may be within fifteen percent of accuracy. They differ depending on the application. For laminar flows a correlation for isothermal properties was recommended by Churchill and Ozoe, the local convection may be obtained from

$$Nu_x = \frac{h_x}{k} = 0.332 Re_x^{1/2} Pr^{1/3} \quad Pr \geq 0.6 \quad (\text{II-35})$$

where Nu_x and Re_x are the local Nusselt number and the critical Reynolds number (where L is the characteristic length x of where the transition starts to occur), respectively. Pr is the Prandtl number (a characteristic of the fluid). The average Nusselt number can be calculated by integrating coefficient, h_x , over the length of the plate resulting in $\overline{Nu}_x = 2Nu_x$. For turbulent flow the following correlation may be used

$$Nu_L = 0.037 Re_L^{4/5} Pr^{1/3} \quad 0.6 < Pr < 60 \quad (\text{II-36})$$

assuming turbulent flow over the entire plate.

For internal flows the critical Reynolds number differs, for laminar flow the value is under 2300. For fully turbulent conditions the value is much larger, 10000. So, careful care should be taken when using the following correlations for internal flow in the fully developed region.

$$Nu_D = \frac{hD}{k} = 4.36 \quad q_s'' = \text{constant} \quad (\text{II-37})$$

$$Nu_D = \frac{hD}{k} = 3.66 \quad T_s = \text{constant} \quad (\text{II-38})$$

Equations (II-37) and (II-38) are used for fully developed laminar flow, for uniform surface heat flux and constant surface, respectively. In this case the critical length is the tube diameter, D . For turbulent flows for $0.5 < Pr < 2000$ and $3000 < Re_D < 5 \times 10^6$ the correlation given by Gnielinski is expressed as

$$Nu_D = \frac{\left(\frac{f}{8}\right)(Re_D - 1000)Pr}{1 + 12.7\left(\frac{f}{8}\right)^{1/2}(Pr^{2/3} - 1)} \quad (\text{II-39})$$

where f is the friction factor for smooth surface given by equation (II-40). This correlation applies for uniform surface heat flux and temperature.

$$f = (0.790 \ln Re_D - 1.64)^{-2} \quad 3000 \leq Re_D \leq 5 \times 10^6 \quad (\text{II-40})$$

It is important to understand that these correlations are approximations. More complex solutions are available; major convection parameters may be obtained by solving the appropriate form of boundary layer equations: Continuity, Momentum, and Energy equations.

Basic concepts of heat transfer were explained. These concepts may be used to design and analyze most solar thermal projects or at least start with a good approximation. When using these concepts assumptions should be made in order to simplify the problem. In other situations numerical analysis may be used in order to solve more complex and time consuming problems.

2.4 Numerical Simulation

For an incompressible flow the governing equations are the continuity and Navier-Stokes equations. In a Cartesian coordinate system they are expressed as

$$\frac{\partial \rho}{\partial t} = \nabla \cdot (\rho \vec{V}) = 0 \quad (\text{II-41})$$

$$\frac{\partial \mathbf{u}}{\partial t} = (\mathbf{u} \cdot \nabla) \vec{V} = -\nabla p + \nabla^2 \mathbf{u} \quad (\text{II-42})$$

$$\frac{\partial v}{\partial t} = (\mathbf{v} \cdot \nabla) \vec{V} = -\nabla p + \nabla^2 \mathbf{v} \quad (\text{II-43})$$

$$\frac{\partial w}{\partial t} = (\mathbf{w} \cdot \nabla) \vec{V} = -\nabla p + \nabla^2 \mathbf{w} \quad (\text{II-44})$$

The analytical solution of these sets of equations is too complex to solve for most problems. For that reason computational techniques have been developed in order to allow engineers and scientist to acquire important information that would otherwise be too difficult to obtain by analytical solutions.

2.4.1 Numerical simulation - Finite volume method

Finite Volume Method is the method used in cd-Adapco Star CCM+™ to represent and evaluate the transport equations mentioned in the previous section. The solution domain is subdivided into a finite number of control volumes that corresponds to the cells of a computational grid, where the numerical integration of the continuum transport equations (the fluid flow) is discretized. The following sets of equations describe the basic discretization methods, for a dimensional steady-state diffusion. The governing equations for fluid flow are

$$\int_{\Delta v} \frac{d}{dx} \Gamma \frac{d\phi}{dx} dV = \int_{\Delta v} S dV = (\Gamma A \frac{d\phi}{dx})_e - (\Gamma A \frac{d\phi}{dx})_w = \bar{S} \Delta V = 0 \quad (\text{II-45})$$

where \bar{S} is the average of the source over the control volume, ΔV is the volume, A is the cross-sectional area, Γ is the diffusive coefficient, and ϕ is the scalar quantity being diffused. Also, e and w are the right and west nodes of the nodal point, respectively. The diffuse terms, Γ , can be expressed as

$$(\Gamma A \frac{d\phi}{dx})_e = \Gamma_e A_e \left(\frac{\phi_e - \phi_p}{\partial x_{pe}} \right) \quad (\text{II-46})$$

$$(\Gamma A \frac{d\phi}{dx})_w = \Gamma_w A_w \left(\frac{\phi_p - \phi_w}{\partial x_{wp}} \right) \quad (\text{II-47})$$

p being the nodal point. The source term, \bar{S} , can be written next, as

$$\bar{S}\Delta V = S_u + S_p\phi_p \quad (\text{II-48})$$

Substituting these terms into equation (II-45) and re-arranging, the following equation is then obtained

$$\left(\frac{\Gamma_e A_e}{\partial x_{pe}} + \frac{\Gamma_w A_w}{\partial x_{wp}} - S_p\right)\phi_p = \left(\frac{\Gamma_w A_w}{\partial x_{wp}}\right)\phi_w + \left(\frac{\Gamma_e A_e}{\partial x_{pe}}\right)\phi_e + S_u \quad (\text{II-49})$$

The result for the sets of equations explained is a three-diagonal matrix. The reason for this that were dealing with a left and right node that are connected to point node in the center, p . A penta and heptagonal matrix is constructed for two and three-dimensional problems. For this case in particular the Reynolds-Averaged Navier-Stokes turbulence model is used.

2.4.2 Numerical simulation - Reynolds-Averaged Navier-Stokes turbulence model

The Reynolds-Averaged Navier-Stokes turbulence model (RANS) is a method that uses the Reynold's decomposition theorem to obtain an equation for the mean velocity profile of the flow [30]. This decomposition is the mathematical technique that separates the sum of the mean and the fluctuating part. This is based on observations in experiments that have shown that a particle under the same boundary conditions for different experiments does not behave the same. However, by tracking the velocity it is shown that the fluctuations of the particle stay within a certain range and the statistical quantities are repeatable. The Reynolds decomposition is expressed as

$$\mathbf{u} = \mathbf{U} + \tilde{\mathbf{u}} \quad (\text{II-50})$$

This decomposition is then used to obtain an equation for the fluid flow. The process consists of substituting equation (II-50) into equation (II-45), and perform a time averaging to obtain the equations in terms of the mean flow properties. After the process of substituting and averaging is finished the resulting equations are

$$\vec{\nabla} \cdot \mathbf{U} = 0 \quad (\text{II-51})$$

$$\frac{\partial u}{\partial t} + \bar{\nabla}(u\bar{V}) = -\frac{1}{\rho} \frac{\partial P}{\partial x} + \nu \bar{\nabla}(\bar{\nabla}(U)) + \frac{1}{\rho} \left[\frac{\partial(-\rho\overline{u^2})}{\partial x} + \frac{\partial(-\rho\overline{uv})}{\partial y} + \frac{\partial(-\rho\overline{uw})}{\partial z} \right] \quad (\text{II-52})$$

$$\frac{\partial u}{\partial t} + \bar{\nabla}(v\bar{V}) = -\frac{1}{\rho} \frac{\partial P}{\partial y} + \nu \bar{\nabla}(\bar{\nabla}(U)) + \frac{1}{\rho} \left[\frac{\partial(-\rho\overline{uv})}{\partial x} + \frac{\partial(-\rho\overline{v^2})}{\partial y} + \frac{\partial(-\rho\overline{vw})}{\partial z} \right] \quad (\text{II-53})$$

$$\frac{\partial u}{\partial t} + \bar{\nabla}(w\bar{V}) = -\frac{1}{\rho} \frac{\partial P}{\partial z} + \nu \bar{\nabla}(\bar{\nabla}(U)) + \frac{1}{\rho} \left[\frac{\partial(-\rho\overline{uw})}{\partial x} + \frac{\partial(-\rho\overline{vw})}{\partial y} + \frac{\partial(-\rho\overline{w^2})}{\partial z} \right] \quad (\text{II-54})$$

Six additional terms are added after the averaging process. These are composed by three normal stresses and three shear stresses. These stresses are known as Reynolds Stresses and are non-zero for turbulent flows. One of these stresses is a 2nd order symmetric tensor known as the Reynolds stress tensor. RANS model has different methods for predicting this stress tensor. One of these methods is the $k - \epsilon$ model.

2.4.3 Numerical simulation - $k - \epsilon$ model

The $k - \epsilon$ model is the most widely used turbulence model in the industry. This is due to the success of the model's predictions in confined flows where the Reynolds shear stresses are most important [31]. It has two equations that need to be solved, one for the mean kinetic energy of the flow, k , and the dissipation rate of turbulence, ϵ .

This method is based on the assumption that an analogy between the viscous stresses and the action of the Reynolds stresses in the mean flow. Newton's Law of viscosity the viscous stresses are proportional to the rate of deformation of the fluid elements. This model is also based on the assumption proposed by Boussinesq, where the Reynolds stresses might be proportional to the mean rates of deformation, hence we have the following equation

$$\tau_{ij} = -\rho\overline{u_i u_j} = \mu \left[\frac{\partial U_i}{\partial x_j} + \frac{\partial U_j}{\partial x_i} \right] - \frac{2}{3} \rho k \delta_{ij} \quad (\text{II-55})$$

where $k = \frac{1}{2} \overline{u_i^2 u_i^2}$ is the turbulent kinetic energy per unit mass [30]. The Reynolds stresses are calculated using this equation.

A velocity scale v and a length scale that is representative of a large scale turbulence l is defined by k and ϵ as follows

$$v = k^{0.5} \quad (\text{II-56})$$

$$l = \frac{k^{1.5}}{\epsilon} \quad (\text{II-57})$$

From these local values a local turbulent viscosity can be expressed as shown in equation (II-58). Here, $C_\mu = 0.09$ and the kinematic turbulent viscosity is described in equation (II-59).

$$\mu_T = \frac{C_\mu \rho k^2}{\epsilon} \quad (\text{II-58})$$

$$v_T = \frac{\mu_T}{\rho} \quad (\text{II-59})$$

With these previous definitions and equations in mind, the standard equations for k and ϵ are written as

$$\frac{\partial(\rho k)}{\partial t} + \vec{\nabla} \cdot (\rho k \vec{V}) = \vec{\nabla} \cdot \left[\frac{\mu_T}{\sigma_k} \vec{\nabla} k \right] + 2\mu_t S_{ij} \cdot S_{ij} - \rho \epsilon \quad (\text{II-60})$$

$$\frac{\partial(\rho \epsilon)}{\partial t} + \vec{\nabla} \cdot (\rho \epsilon \vec{V}) = \vec{\nabla} \cdot \left[\frac{\mu_T}{\sigma_\epsilon} \vec{\nabla} \epsilon \right] + C_1 \epsilon \frac{\epsilon}{k} 2\mu_t S_{ij} \cdot S_{ij} - C_2 \rho \frac{\epsilon^2}{k} \quad (\text{II-61})$$

The standard $k - \epsilon$ model explained above has certain constraints and weaknesses that are addressed using the realizable $k - \epsilon$ model. This model will be best explained in the next section.

2.4.4 Numerical simulation – Realizable $k - \epsilon$ model

As mentioned the realizable $k - \epsilon$ addresses some weaknesses that the standard $k - \epsilon$ contains. One of these weaknesses consists of giving negative values for the normal stress $\overline{u^2}$ for certain conditions. Another one lies in the equation for the dissipation rate. These weaknesses are addressed by adopting a

new viscosity formula where the constant C_μ is variable and creating a new model equation for the dissipation based on the dynamic equation of the mean squared vorticity fluctuation.

A feature of this model is that the equation for the dissipation does not involve the production of k .

A second feature of this model is that the destruction term does not have singularity.

2.4.5 Numerical simulation – Radiation

The radiative transfer model in CCM+™ defines the overall solution method for the governing Radiative Transfer Equation. The Surface-to-Surface radiative heat transfer is used for modeling non-participating media and in effect has two radiation spectrum models, the gray thermal radiation and the multiband thermal radiation.

The gray thermal radiation model is used to model wavelength-independent radiation properties, the full thermal wavelength domain is considered as a whole. While for the multi band thermal radiation model the full-thermal spectrum can be divided into spectral bands. When solving in this last model, the transfer model is applied to each spectral band. The resulting solution of the individual spectral band is then added to have the total radiative transfer.

Star-CCM+™ operates the Surface-to-Surface radiation model by first calculating the view factors by the use of ray tracing. Then, it calculates the radiosity and irradiation on all surfaces. The radiation that is exchanged between the surfaces depends on the emission from the surfaces and the position and orientation of the surfaces relative to each other, as well as any surface that can alter the transfer between these surfaces. These properties are accounted for by the view factor, which is the fraction of the diffuse radiation leaving a surface that directly reaches another surface. For surfaces of finite size the view factor is expressed as

$$F_{2-1} = \frac{1}{A_2} \int_{A_1} \int_{A_2} \frac{\cos(\theta_1) \cos(\theta_2)}{\pi L^2} dA_1 dA_2 \quad (\text{II-62})$$

where F_{2-1} is the view factor for two surfaces where the radiation exchange is from a surface 2 to a surface 1. θ_1 and θ_2 are the zenith angle for each surface and A_1 and A_2 are the area of surface one and surface two, respectively, it can be best appreciated by observing Figure 9.

In Star-CCM+™, the boundary surfaces are discretized into small elements, where the view factors are calculated for each pair of these elements. Ray tracing is used to approximate the double integral of equation (II-62). A predefined number of rays are set per each element; their directions and weights are based on discretization of an ideal hemisphere over the patch.

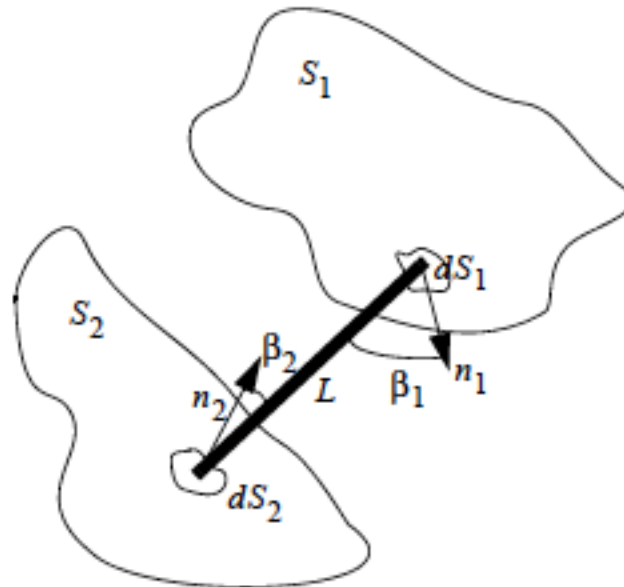


Figure 9: Radiation exchange between two surfaces. User Guide Star-CCM+ Version 8.04. (2013). Radiation Exchange Between Two Finite Surfaces. p. 3406.

After the surfaces are divided into elements and the view factors are computed for each patch pair, the radiant fluxes between the surfaces are obtained. The radiation between the surfaces is obtained by enforcing radiation equilibrium between them. This means that the energy received by a surface element must be sent from another surface element.

It is important to point out that Star-CCM+™ uses Kirchhoff's law in thermal radiation model, where for any surface in an enclosure the total, hemispherical emissivity of a surface is equal to its total, hemispherical absorptivity.

$$\boldsymbol{\varepsilon} = \boldsymbol{\alpha} \quad (\text{II-63})$$

III. Literature Review

Throughout the years, since its first description, there have been many alternatives for practical embodiment of absorber designs [4], [9], [11], [32], [33], starting with Francia's. Francia's elevated absorber consisted of 12 steel pipes, 8 m long, placed 20 m above the mirror array, insulated above and below by a cellular borosilicate glass structure. Although Francia was the first to implement this new concept of a linear concentrator he did not give performance figures for it [12]. Since then many authors have contributed seeking better thermal performance by changing the geometry of the absorber, the materials used, the size and type of tubes used, among others.

As mentioned, several designs exist but typically a horizontal type is favored and a particular design is often utilized due to its simplicity and low cost. A trapezoidal cavity receiver, most of the times, is comprised of insulated absorber pipes and a cover glazing forming a cavity where rays are collected and heat loss is minimized, in some occasions a reflector plate is also used. Despite the different geometrical designs, a well-designed receiver can increase the performance considerably [13].

In 1999 Singh et al. [10] analyzed an absorber that consisted of an aluminum pipe (0.075 m diameter and 0.53 m long, small compared with Francia's) painted with dull black paint and was covered by a trapezoidal shape cover with mirrors on each of the three sides. The cover was insulated with 25 mm of thick glass wool with the bottom portion closed with a 15 cm wide plane glass to allow entry of light and trap infrared radiation. The absorber tube was filled with Hytherm-500 oil and withstood up to 232°C in this analysis. Singh et al. found that increasing the number of mirrors (concentration) the overall efficiency of the system tended to decrease. With this deduction he then concluded that the Linear Fresnel Concentrator is preferable for medium temperature heat application, which may be around 225°C and in the range of our application [10].

In 2004 Reynolds et al. [34] focused on the absorber and cavity arrangement and aimed to optimize the design of the cavity to achieve maximum thermal efficiency and to develop a model of the collector in order to predict and control the steam condition at the collector exit. The receiver consists of a trapezoidal cavity where a flat plate absorber forms the uppermost surface of it. It is enclosed by a glass window in the bottom of the cavity to minimize convection losses due to the wind and to let solar radiation from the mirror array to enter the cavity in order to absorb its energy. The sides and top are insulated to minimize conduction and convection losses to the environment. Radiation losses are also important to look out for since they present most of the heat loss in these types of absorbers.

Reynolds et al. (2004) [34] also developed an experiment to validate results produced by a computational model using the Fluent v.5 commercial package. The experiment apparatus consisted of a cavity 1.55 m long and 0.42 m deep, where the upper surface is 0.52 m wide and the lower surface is 0.93 m wide. To approximate an isothermal surface an aluminum plate is attached to the underside of heaters. For the computational model, the heater surface is modeled as isothermal while the wall sides have convection boundary conditions. The bottom surface is modeled as a combined convection/radiation boundary to account for the heat transfer at the window.

Reynolds et al. (2004) [34] found excellent agreement between the experimentally observed flow patterns and those predicted by the computational model. Even though the patterns were very similar the total heat loss between the two methods showed an obvious discrepancy which could be attributed to the need of a more controlled experiment and/or a more detailed computational model [34].

Later in the same year (2004), Dey [12] discussed how to maximize the heat transfer between the absorbing surface and the steam pipes while minimizing the overall losses of the absorber, maximizing the optical efficiency of the absorption of the incident flux and maintaining the absorber surface temperature sufficiently uniform to prevent degradation of the selective surface. The absorber

investigated consisted of several pipes attached to a plate absorber, coated with a selective surface to minimize the radiation loss, and a non-convective air cavity below this plate. A coated absorber plate attached to the pipes was necessary since coating long pipes was difficult to do.

Dey (2004) used Finite Element Analysis (FEA) to analyze the receiver. He modeled several designs that consisted in changing the thickness of the absorber plate and the size of the pipes. Assuming the temperature of the fluid is 540 K, he found that acceptable difference in temperature between the absorber plate and the fluid inside the pipes can be achieved for a bar thickness of approximately 6 mm and the closest allowable spacing between the pipes [12].

These last two authors did their observations on the receiver assuming the temperature of the fluid or the absorber plate. Singh et al. (2009) on the other hand made experiments by manufacturing a fully functioning LFR prototype where it heated water up to 100°C and Hytherm-500 oil to 175°C. The prototype consisted of 132 mirrors of 0.535 m of longitude and 0.1 m of width in four (4) rows. It also consisted of a trapezoidal cavity receiver with six mild steel round tubes (OD 16mm, 2.5mm of thickness, and 2.17 m of length) brazed together making the absorber tubes 0.1 m wide. These pipes were painted with ordinary matt black paint and another set was coated with black nickel selective surface. Similarly, two rectangular pipes were also fabricated and both were painted and coated as the round pipes. The rectangular pipes measured 0.1 x 0.023 m and 2.17 m long. The sidewalls had 0.005m thick ceramic tile plates and glass wool insulation of 0.1 m thick was provided at the upper top and sides of the absorber pipe.

Singh et al. (2009) experiments were done at different concentration ratios and revealed that the concentration ratio and the selective surface coating in the absorbers influenced the thermal efficiency. The thermal efficiency decreased as the concentration ratio increased, this is due since the greater the temperature of the receiver the greater the radiation heat loss of it. At the same time the authors found

that the thermal efficiency in round pipes was greater (2-8% higher) than rectangular pipes and even more so with black nickel selective surface coating (30 % difference). Singh et al. also developed correlations where the deviations with the experimental data were within a $\pm 12\%$ limit.

Facção and Oliveira (2011) were involved in a study that did not include experimentation. They used ray tracing and CFD simulations to optimize a new trapezoidal cavity. Simplified ray trace simulation was used to figure out the number of absorber tubes needed and the inclination of the sidewalls. The CFD simulations were performed by the use of Fluent software and was employed to optimize the cavity's depth and the insulation thickness by means of evaluating the global heat transfer coefficient. The system is composed of 10 rows of 4 mirrors with 0.4 m of width and 3 m in length. The absorber consists of a trapezoidal cavity with 6 half-inch ID pipes.

A total of eighteen (18) combinations were simulated; changing the pipe temperatures: 110°C, 170°C, and 230°C, the depth of the cavity, the external air temperatures, and the external heat transfer coefficient. From the ray tracing simulation Facção and Oliveira (2011) found that 50° of inclination from the walls was found optically acceptable and that using 6 absorber tubes with an ID of $\frac{1}{2}$ in collects all the concentrated beam radiation. Now, with the CFD simulation they concluded that a cavity with a 0.045m depth presents the lowest global heat transfer coefficient and that 0.035 m of insulation (rock wool) thickness is a good compromise between insulation and shading [35].

Finally, Sahoo et al. (2012) also investigated the heat loss in a trapezoidal cavity by a two dimensional computational modeling using Fluent software. The closed trapezoidal cavity proposed for the study consists of 8 tubes of Stainless Steel (SS) 304 material. The cavity, even though closed, is filled with air and the outer walls are covered with glass wool insulation. Simulations were run with different cavity depths taking into account the wind speed below the glass, the emissivity of the tubes, and the

gaps between the tubes. The temperatures of the tubes were simulated between 350 and 450 K and were simulated as isothermal boundary conditions.

The results of these models were compared and validated with experimental data and showed a very good match between them. The validated model was used for simulation of the trapezoidal cavity for different parameters. Sahoo et al. (2012) observed that radiative losses from the cavity were dominant and contributed 80 – 90% of the total heat loss. The results from the computational studies were used to obtain correlation between the average Nusselt number and its parameters and can be used for analysis of similar trapezoidal cavities.

Most of these articles involve Linear Fresnel Reflectors that are quite large for the purpose of this study. Considering the objective of the thesis information of flat plate collectors (also known as solar air heaters) was researched. Many studies and proposed designs for these collectors were found. These are used for drying of agriculture and textiles as well as for heating of water and air for building spaces [3], [7], [36], [37].

One example of agricultural use was a study by Pangavhane et al. (2002), where in it explains the design and development of a natural convection dryer [38]. A flat plate collector was used as the technology to heat air in a purely mechanical form, heating air to create a temperature gradient that then causes the air to flow and dries grapes through natural convection. Pangavhane et al. concluded that the designed solar dryer was capable of producing average temperatures of 50 and 55° C, optimal temperature range for dehydration of the grapes as for most fruits and vegetables, including coffee, for different flow rates. This reduced the time of drying by 43% when compared to open sun drying [38].

Designs of flat plates differ depending on its application, but mainly to increase its efficiency. There are many ways to do this, by increasing the fluid flow in the collector, increasing the surface area in contact with the fluid (air), decreasing heat loss, among others. Decreasing heat loss may be done using

different methods like increasing the number of glasses used (e.g. double glazing), by painting the plate with a special selective coating where it absorbs most of the radiation and has a very low emissivity, or by using insulation with high resistance to thermal conduction.

F.K. Forson et al.(2003) experimented with a single pass, double duct solar air heater. The study demonstrated that significant improvement can be obtained by an appropriate choice of collector parameters and channel depth ratio of the two ducts [37]. Another similar design is that of a double pass, single duct solar air heater. The thermal efficiency of the double pass air heater is greater to that of the single pass with the concepts of having double the area for heat transfer. Yeh et al.(2002) reported that the best thermal efficiency can be achieved in a double-flow solar air heater, where the upper and lower channels are equal in height and the mass flow rates in each channel are the same [39]. Chamoli et al. (2012) presents an extensive study of double pass solar air heaters where they discuss many mathematical models based on energy analysis of some configurations[40]. Another method to enhance the heat transfer is by adding some geometrical roughness.

Many studies address the geometrical roughness aspect of a flat plate collector due to its low convective heat transfer coefficient between the air and the absorber plate. This is due to the formation of a laminar sub layer on the heat-transferring surface. It is recommended to break this layer in order to augment the heat transfer at the surface. Artificial roughness may include transverse continuous and broken ribs, inclined ribs, V-shaped ribs, and those with a combination of different integral ribs.

Several comparative studies have been made with correlations of respected investigators. Gupta and Kaushik (2009) conducted a comparative study for various types of artificial roughness geometries. The performance evaluation was carried out for different values of Reynolds number for six different roughness geometries and one with smooth surface. They found the energy efficiency to be best for chamfered rib-groove and least for smooth surfaces [41]. M.K. Mittal et al. performed a similar study

and found that the effective efficiency increased by increasing the Reynolds number until a certain point, it attained a maxima and then started to decrease. This may be due to the mechanical power required to overcome the frictional forces. M.K. Mittal et al. also observed that certain geometry roughness performed better at high Reynolds number and others at low Reynolds number. They concluded that solar air heaters with inclined ribs had better effective efficiency in the high Reynolds number and expanded metal mesh for lower Reynolds number [42]. In the same line of thought, Bhushan and Singh (2010) categorized and reviewed reported roughness, as well as reported heat transfer coefficient and friction factors correlations for correlations developed by numerous investigators [43].

Other authors have written reviews to assist in the design of solar air heater systems. Tchinda (2009) reviewed several mathematical models. He classified them by the number of covers and the absorber's [44]. He also showed that the governing equations are based on the first law of thermodynamics. Dhariwal and Mirdha (2004) present analytical expressions for many cases of practical interest. The theory presented allows the performance prediction of the collector and can be applied to actual field conditions when storage and load are included [45].

All these were helpful in the development of the work presented in Chapter V. The procedure and methods used will be presented along with results of the different stages present in Chapter IV.

IV. Objectives

Our primary objective is to design and manufacture a Linear Fresnel Reflector prototype and test two collectors and evaluate their performance.

We will:

- Design two solar collectors for the system.
- Run simulations for the different designs of collectors to find their thermal performance in order to have another available tool to help in future designs and analysis.
- Build a Linear Fresnel Reflector prototype with the collector and make test if the collector can heat air to 50 °C.

V. Method and Results

This chapter outlines the method and procedures used in our work. Our work consisted of the design, simulation, and manufacture of a Linear Fresnel Reflector used to heat air. We also performed experiments to validate that our design objectives were achieved. Computational modeling was used to analyze the thermal performance of two conceptual receivers. Thru an iterative process of modeling and design we produced the final design of a collector set to heat air from ambient temperature to 55°C. An important restriction to our design was cost. We want to achieve the desired air temperature using locally available and inexpensive materials. We manufactured the concentrator and integrated it to an existing Linear Fresnel Reflector. Then, experiments were carried out to verify that our objectives were achieved. A more detailed description of these steps is described in the following sections, which follow the steps graphically depicted in Figure 10, below.

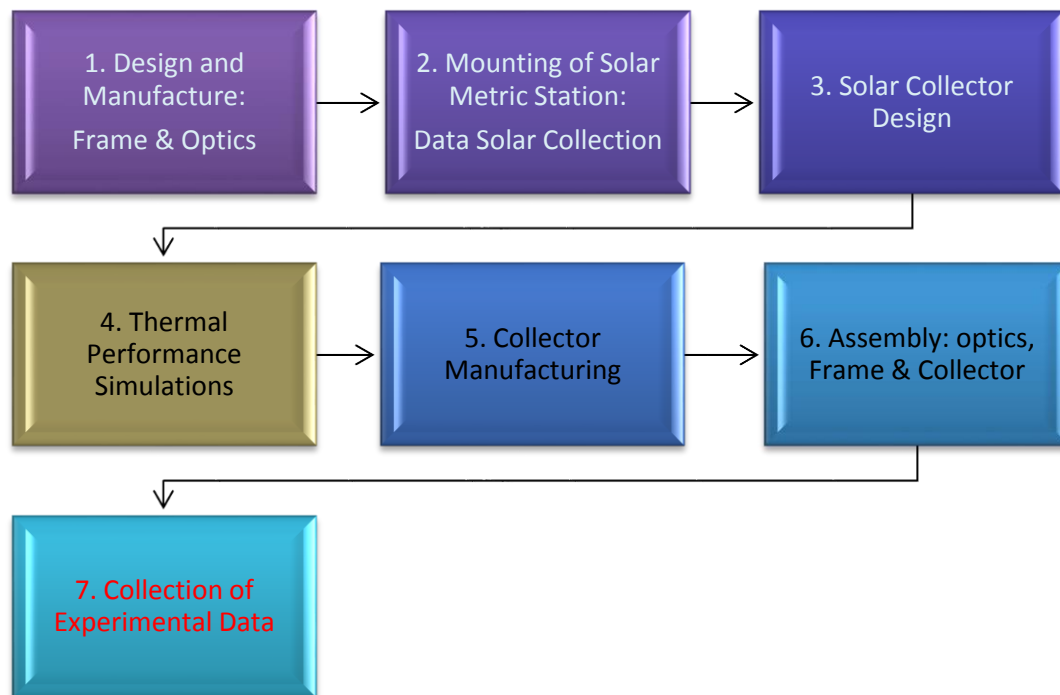


Figure 10: Methodology diagram

5.1 Design and Manufacture of Linear Fresnel Reflector

The Linear Fresnel Reflector prototype was designed and manufactured with contributions from Alexander Rivera and Christian Correa, undergraduate students of the Electrical Engineering Department at the University of Puerto Rico – Mayaguez campus. They [46] defined the dimensions and general shape of the Linear Fresnel Reflector (LFR). They also designed and performed laboratory tests of the sun tracking system for the LFR. We manufactured the Linear Fresnel Reflector after reviewing and modifying the original plans to ease the manufacturing process.

The first step of the review process was to select a suitable frame material, a material light but strong enough to carry the collector that was later to be mounted on it. At the moment of selecting materials, we considered strength and strain calculations, resistance to corrosion, thermal conductivity, thermal expansion, weight of the material (density), machinability and cost, among others. Based on this evaluation four different materials were considered as candidates.

The materials considered were iron, steel, stainless steel, and aluminum. Iron and steel were ruled out because of their high corrosiveness when compared to the other materials; they oxidize quickly, especially in the environment where the prototype was to be installed; close to the sea coast. Aside from this, Iron was hard to obtain locally in the dimensions needed and is quite expensive. This left us with stainless steel, for its corrosion resistance and strength, and aluminum, for its corrosion resistance and lower price. Table 1 shows a comparison of their physical properties.

Static equilibrium, bending, and deformation calculations were made for aluminum 6061 and stainless steel 304 to evaluate the design and find the maximum load it can withstand (Appendix 7.2).

Table 1: Material Properties of Stainless Steel 304 and Aluminum Alloy 6061

NAME	Composition (wt%)	Density		Modulus of Elasticity		Poisson's Ratio	Yield Strength	Tensile Strength	Elongation Percentage	Coefficient of Thermal Expansion		Thermal Conductivity		Specific Heat		Electrical Resistivity
		g/cm ³	Lb _m /in ³	GPa	10 ⁶ psi		(MPa[Ksi])	MPa[Ksi]		10 ⁻⁶ (°C) ⁻¹	10 ⁻⁶ (°F) ⁻¹	W/m-K	Btu/ft-h-°F	J/kg-°K	10 ⁻² Btu/lb _m -°F	Ω-m
STAINLESS STEEL (Stainless alloy 304)	66.4Fe 0.08C 19.0Cr 9.25Ni 2.0Mn	8.00	0.289	193	28	0.30	205[30]	515[75]	40	17.2	9.6	16.2	9.4	500	12	7.2x10 ⁻⁷
ALUMINUM ALLOY (Alloy 6061)	95.85Al 1.0Mg 0.6Si 0.30Cu 0.20Cr	2.70	0.0975	69	10	0.33	276[40]	310[45]	17	23.6	13.1	180	104	896	21.4	3.7x10 ⁻⁸

At Room Temperature

Afterwards, Siemens NX software was used to model the frame parts of the system. Each part of the system is modeled separately and then assembled using the assembly tool in the software, Figure 11. Some parts modeled did not need manufacturing: motors, gears, potentiometers, bearings, mirrors, nuts, and bolts. After modeling all parts, except the absorber, we carried out the manufacturing and assembly process at the Manufacturing Laboratory of the University of Puerto Rico at Mayaguez in the Mechanical Engineering Department.

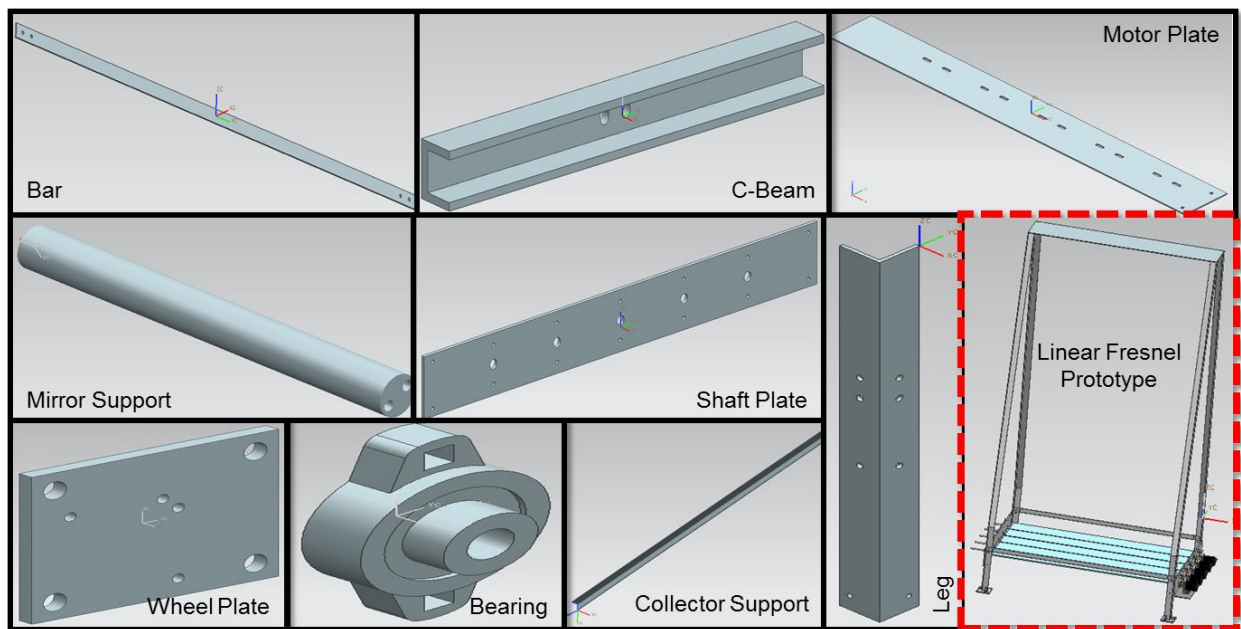


Figure 11: Modeled parts using Siemens NX software.

At the same time, the mirrors used as solar beam reflectors were purchased and the electric circuits to perform the solar tracking were built in the Electrical Engineering Department of the University of Puerto Rico by Carlos Garcia. The solar tracking system was assembled along with a computer that ran the solar tracking algorithms and the frame.

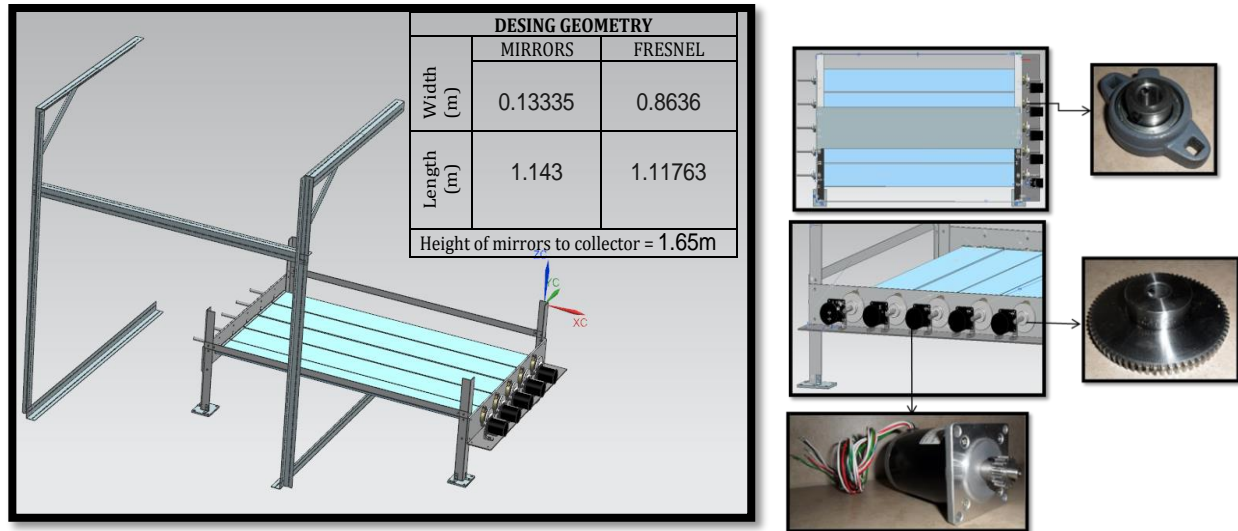


Figure 12: Design and manufacture of the frame and optics system. Prototype in Siemens NX software.

After several practical modifications to the original design ideas it was decided to work with the prototype shown in Figure 12. Its basic geometric data for the manufacture is tabulated in Figure 12.

5.2 Radiation and Temperature Measurements

In order to properly design the collector (absorber) for the system two important parameters should be measured, total radiation and temperature. These were collected by the use of sensors and were later processed in order for them to be used. This chapter explains the equipment used for the data collection and the process that was carried out in order to use them in the design.

5.2.1 Weather station measurements

A weather station was installed on the roof of Stefani Building located at the University of Puerto Rico at Mayaguez to record atmospheric conditions that were used to determine the thermal performance of the collectors. The atmospheric data collected included global solar radiation, ambient temperature and relative humidity. The weather station consist of a LP02-L pyranometer from Hukseflux, a HC2S3-L temperature and relative humidity probe manufactured by Rotronic, a solar panel from BP, and a CR100 measurement and control system data logger from Campbell Scientific, as shown Figure 13.



Figure 13: Weather Station

Solar radiation measured by the pyranometer consists of total solar radiation in the full solar spectrum range. Data are sampled at one-second interval and the average is then stored in the data logger. The data logger stores the measurement as solar radiation in Watts per square meters (W/m^2) and global solar insolation in mega Joules per square meters (MJ/m^2), for every ten seconds. With this short interval data, one can always sum or average it into longer intervals, giving some flexibility on how to use the data.

As mentioned, it is important to divide in different components the beam and diffuse radiation. The clearness index along with the Erbs et al. correlation explained in section 2.1.5 was used to fulfill this task. The global solar insolation measured, I , is used in equation (II-25), which follows:

$$k_T = \frac{I}{I_o}$$

where I_o is found by the relationship between the concepts and equations explained in section 2.1.2 for a specific time interval; here, the hour angles ω_1 and ω_2 are the limits of that mentioned time period (e.g. ω_1 represents the solar hour at 9:00:00 and ω_2 at 9:00:10 for 10 second interval). Knowing the clearness index, k_T , the diffuse insolation, I_d , was then determined by equation(II-26):

$$\frac{I_d}{I} = \begin{cases} 1.0 - 0.09k_T & \text{for } k_T \leq 0.22 \\ 0.9511 - 0.1604k_T + 4.388k_T^2 - 4.388k_T^3 + 12.336k_T^4 & \text{for } 0.22 \leq k_T \leq 0.80 \\ 0.165 & \text{for } k_T > 0.8 \end{cases}$$

The diffuse insolation, I_d , was then subtracted from the global solar insolation, I , to give the beam solar insolation, I_b . Both terms were converted from insolation, MJ/m², to solar radiation, W/m², by multiplying the insolation by the desired time interval. Subsequently, the beam radiation was used to estimate the radiation that reached the collector.

5.2.2 Radiation incident on the collector

The concentration of beam radiation on the collector is the result of the radiation reflected by the mirrors located below the collector. To estimate the beam radiation incident on the collector it was necessary to calculate the direct beam radiation, $G_{b,n}$, described in section 2.1.6. This is due to the fact that the beam radiation calculated in the previous section is beam radiation incident on a horizontal surface, G_b . This was possible by rearranging equation (II-27) to equation

$$G_{b,n} = \frac{G_b}{\cos \theta_z} \quad (\text{V-1})$$

The direct solar beam radiation, $G_{b,n}$, is also multiplied by the reflection of the mirrors, ρ , and the transmittance-absorptance product explained in section 2.1. The value for the transmittance of the glass was adopted from a study performed by Nicolau and Maluf [47], where they present the spectral radiative properties of commercial glass. The values of these properties are presented in Table 2. In addition, the absorptance value used for the collector was that of black paint (0.95).

Table 2: Spectral radiative properties for commercial glass

VISIBLE		
Transmittance	Absorptance	Reflectance
0.86	0.06	0.08
INFRARED		
0.78	0.15	0.07
VISIBLE + INFRARED		
0.82	0.11	0.07

The steps taken into consideration to calculate the beam radiation incident on the collector in this section have been generalized for the analysis of a single mirror for a specific time; with the objective of making it simple to the reader. But, in practice the data was worked with the algorithm present in Appendix 7.3, where each of the 5 mirrors was analyzed at specific time intervals. The data obtained from the algorithm was then tabulated for it to be used further. Since the analysis were done in steady state, the average of the peak radiation hours were calculated (from 9 am to 11, around noon it always got cloudy) and it was decided to use 650 W of irradiation.

5.3 Solar collector design

Currently different researchers have focused their attention and contributions to the design of collectors that heat liquid phase material. Many of them have presented designs with different geometries and materials, having various options offered by the literature. Our Linear Fresnel Reflector is a prototype used to analyze the feasibility of using air (a gas) as the working fluid. We desired to produce a collector that was simple and inexpensive to manufacture.

The prototype is a design combination of models described in the literature based on concepts studied over the years. The main frame was constructed with similar length and width of that of the mirrors. The material used for the frame was wood for its simplicity in manufacture and low cost. Its interior consisted of six one-inch (0.0254m) square aluminum tubes (1.1938 m long), where the working fluid was transported. This arrangement (six one-inch tubes) was preferred for two main reasons. Firstly, by the concept that the heat transfer rate may be increased by increasing the surface area where convection occurs. Having said that, six tubes have more surface area in contact with the fluid than an arrangement of less tubes and wider openings and is shown in section. Secondly, the pressure drop had to be considered, when it increases the power requirement from the fan also increases. Observing equation (V-2) and equation (V-3) one can appreciate this behavior, where the lower the diameter of the tube the greater the pressure drop would be by maintaining the same velocity.

$$\Delta p = f \frac{\rho u_m^2}{2D_h} (x_2 - x_1) \quad (V-2)$$

$$P = (\Delta p)V \quad (V-3)$$

where f is the friction factor of the tube, ρ is the density of the fluid (air in this situation), u_m is the mean velocity of the flow, and D_h is the hydraulic diameter of the tube. The term $x_2 - x_1$ is then the length of the tube, where x_2 is the axial position at the exit and x_1 is the axial position of the entrance of the tube. Lastly, for equation (V-3), P and V are the fan power and the volumetric flow rate, which may be expressed as $V = \dot{m}/\rho$, respectively.

The aluminum tubes were then painted with black spray paint in order to increase its absorption capabilities. At the same time, while increasing the absorption capability, the paint also increased the emittance, ϵ , of the collector, where the energy was emitted as long wave radiation. For this reason the collector was sealed with glass, which is opaque to long wave radiation, in order to decrease the loss

of energy. Moreover, glass has a high solar transmittance (Table 2) making it ideal for the use of solar energy[48].

Finally, the collector had insulation to decrease thermal conduction, which would have resulted in greater heat loss through convection to the environment. Glass wool was the material used for the insulation, a locally available material.

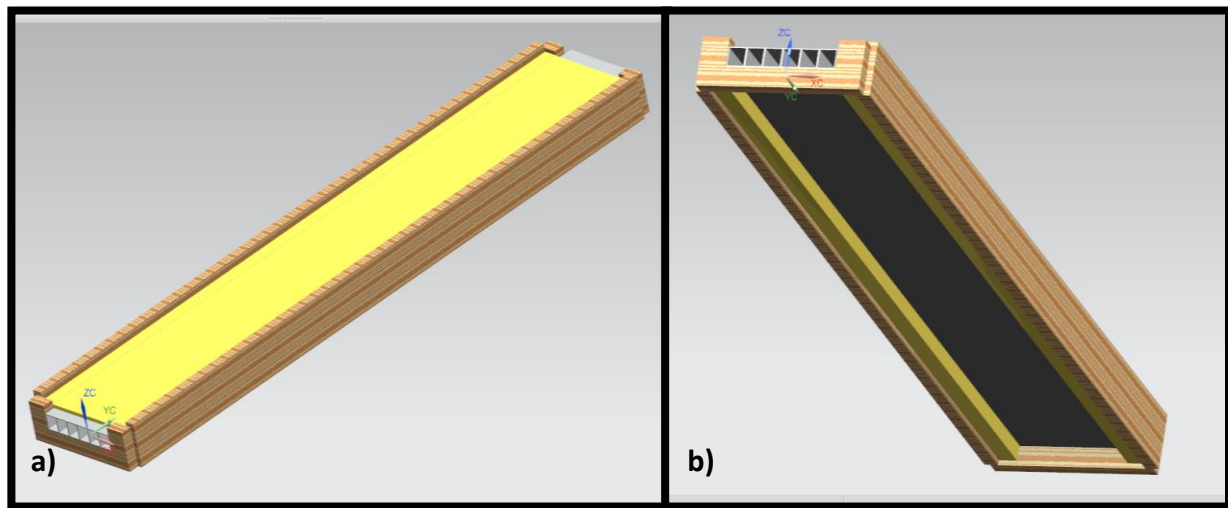


Figure 14: Siemens NX design of solar collector: a) Top view, b) Bottom view

The collector was modeled in Siemens NX software shown in Figure 14 and it was designed and manufactured to have an additional piece of glass installed on the top of the collector. This provided us with an additional collector by removing the insulation from the top and substituting it with a piece of glass. This allowed the entrance of solar radiation through the top of the collector.

In order to arrive to this particular design a set of calculations were formulated, solved, and analyzed. The method used, the assumptions, along with the results are explained in section 5.3.1.

5.3.1 Solar collector design - Flat-Plate equation formulation

The methods and formulation used in this section are based on the basic concepts mentioned in Chapter II. These methods can be simplified by using an equivalent thermal circuit or as in this case a thermal network. This type of representation, a thermal network, is useful for conceptualizing and quantifying heat transfer problems and are used for one-dimensional energy transfer.

The thermal network applied for the collector that was manufactured is used to explain the equations that were solved to analyze the thermal performance of the collector designs that were compared. To start, collectors with 3 two-inch, 6 one-inch, and 12 half-inch rectangular tubes were analyzed. Their thermal networks are similar to that of Figure 15, where the difference with each of them is in the calculation of the heat transfer, q , by convection, which is analyzed by applying fin theory.

In order to use the thermal network of Figure 15 a number of simplifying assumptions can be made without obscuring the basic physical situation of the problem. These may be numbered as follow

1. Steady-state performance
2. Uniform flow inside the tubes
3. One-dimensional heat flow through the cover and insulation
4. The sky is considered a blackbody for long-wavelength radiation at an equivalent sky temperature
5. The temperature gradients in the direction flow and between the tubes can be treated independently
6. Dust, dirt, and shading on the collector are negligible

Considering these assumptions it was possible to solve the steady state thermal performance of the collector. The material properties used for the tubes in this analysis is that of aluminum, it has a high conductivity (237 W/m-K) and is less expensive than copper (which has higher conductivity than

aluminum). For the insulation, glass wool for housing was used (2.365 W/m-K) and assuming uniform temperature in the glass, there is no need for a conduction resistance in the thermal network.

In any flat-plate solar collector the solar energy, S , is incident and absorbed by the plate, in the tubes in this particular case, where its temperature is T_p . S , is equal to the solar radiation calculated with the steps discussed in the subsequent section 5.2, which includes the optical losses by reflectivity of the mirrors and the absorptivity and transmissivity of the glass which can be summarized by equation (V-4).

$$S = G_{b,n}\rho(\text{abstrans}) \quad (\text{V-4})$$

where ρ is the reflectivity and *abstrans* is the absorption and transmissivity product. This energy is then transmitted to the working fluid, as useful energy, and is also distributed as thermal losses through the insulation and the glass. As mentioned before the value of S is of 650 W.

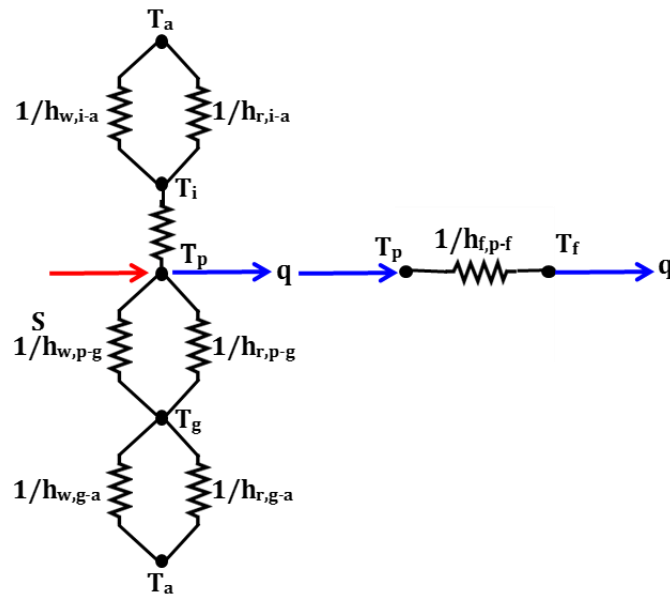


Figure 15: Thermal Network for a collector of 6 tubes, with a glass cover, and insulation in the back and sides of the tubes.

The thermal loss through the insulation is the result of conduction through the insulation and is equal to the steady state energy transfer from the top insulation temperature on the environment side at T_i to the environment temperature at T_a . Similarly, the steady state energy transfer between the

glass at T_g and the environment at T_a is equal to that of the thermal loss from the bottom of the tubes at T_p to the glass at T_g . The following equations, which also denote the T_i and T_g nodes, represent the thermal loss through the insulation and through the glass, respectively.

$$\varepsilon_l \sigma A_c (T_i^4 - T_a^4) + h_w A_c (T_i - T_a) = \frac{k_l}{L_l} A_c (T_p - T_i) \quad (\text{V-5})$$

$$A_c \frac{\sigma(T_p^4 - T_g^4)}{(\frac{1}{\varepsilon_p} + \frac{1}{\varepsilon_g} - 1)} + h_{nc} A_c (T_p - T_g) = h_w A_g (T_g - T_a) + \varepsilon_g \sigma A_g (T_g^4 - T_a^4) \quad (\text{V-6})$$

Here T is for temperature and the subscripts l , p , g , and a are for insulation, tubes, glass and ambient, respectively. The convective heat transfer coefficients, h , are for the wind, subscript w , and for natural convection, subscript nc , between the glass and the tubes. The node from where the energy that is transferred to the working fluid is expressed in the following equation (V-7).

$$S = \frac{k_l}{L_l} A_c (T_p - T_i) + A_c \frac{\sigma(T_p^4 - T_g^4)}{\frac{1}{\varepsilon_p} + \frac{1}{\varepsilon_g} - 1} + h_{nc} A_c (T_p - T_g) + \frac{2k_l}{L_l} A_s (T_p - T_{Is}) + q_c \quad (\text{V-7})$$

The solar energy, S , is distributed as conduction, through the insulation, radiation and convection, between the tubes and the glass, where they are represented as the first three terms of the right side of the equation. The fourth term equals to the thermal loss by conduction to the sides of the insulation (the sides of the collector), which is typically the same as the top insulation term in equation (V-5), with the area as A_s for the side of the tubes. The last term in the equation is that of the energy transfer to the working fluid and is expressed in the following equation

$$q_c = 2 \eta_o h_f A_t (T_p - T_f) \quad (\text{V-8})$$

where η_o is the overall fin efficiency, h_f is the convective coefficient heat transfer, A_t the total area used for the overall fin efficiency, and T_f is the fluid temperature. The overall fin efficiency can be expressed as equation (V-9), as seen below. Here, η_f is the fin efficiency, equation (V-10), and A_{sf} is the

area that consists of the sides of the fin, $L_s/2$, where L_s is the height of the sides of the tube channels (the length then, is the largest dimension of the tube).

$$\eta_o = 1 - \left(\frac{NA_{sf}}{A_t} \right) (1 - \eta_f) \quad (\text{V-9})$$

$$\eta_f = \frac{\tanh(m(L_s/2))}{m(L_s/2)} \quad (\text{V-10})$$

where $m = \sqrt{hP/kA_c}$, with h as the convective heat transfer coefficient of the fluid (air) inside the tube, P as the fin perimeter, k as the thermal conductivity coefficient, and A_c is the cross-sectional area of the fin.

These equations were solved using Engineers Equation Solver (EES) since it simplifies the iteration process necessary to solve them. This software also has built-in formulation that is used to calculate the convective heat transfer coefficient for constant heat flux, h_f , and to determine the fin efficiency, η_f . The complete formulation of these equations, along with the inputs needed to solve them, can be found in Appendix 7.5.

To start, the temperature desired for the air at the output couldn't be greater than 55°C, since coffee beans get damaged when the air temperature is higher than this. At the same time, knowing that the radiation of the Sun changes throughout the day varying the temperature output, it was decided to focus the outlet temperature of 50°C. This gave flexibility for the changes in temperature as the day passed by. With this in mind it was important to know the mass flow rate needed to maintain the temperatures mentioned. Figure 16 is a plot that shows the relationship of the output temperature to the total mass flow rate (sum from all tubes) in the tubes for the two-inch rectangular tubes design. The plot shows that for a temperature output between 50 and 55 the total mass flow rate should be between 0.016 - 0.023 kg/s for each tube.

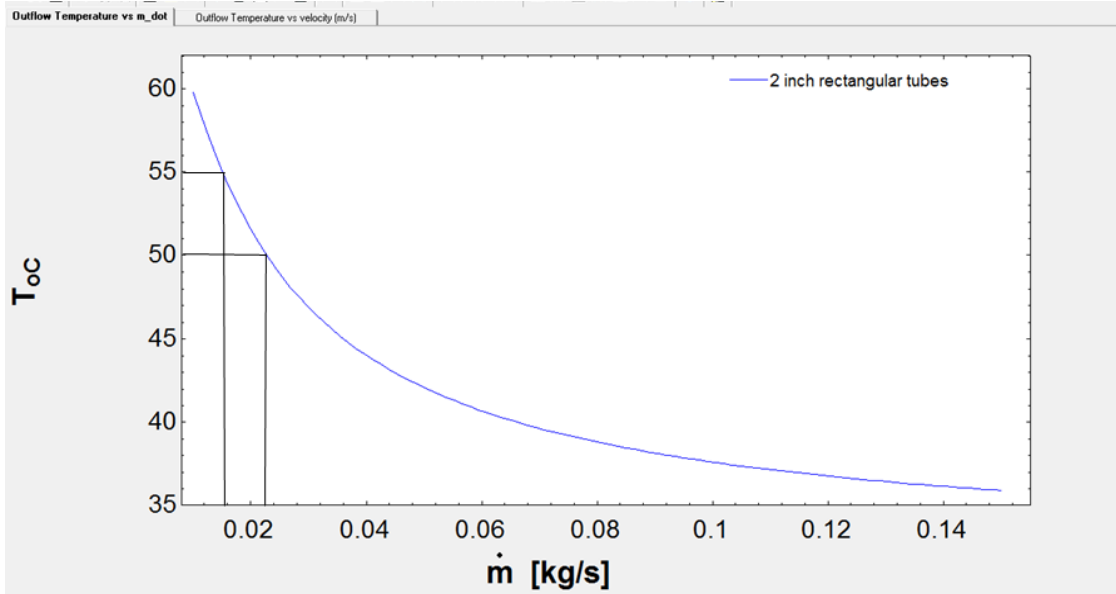


Figure 16: Output temperature vs total mass flow rate plot for the two-inch rectangular tubes design

The velocity inlet for each tube was also desired since the information of the equipment used in the experiments was given in velocity (m/s). For this reason an outlet temperature vs velocity plot was drawn and is shown in Figure 17, where the temperatures of interest lie between 2 m/s and 3 m/s for each tube.

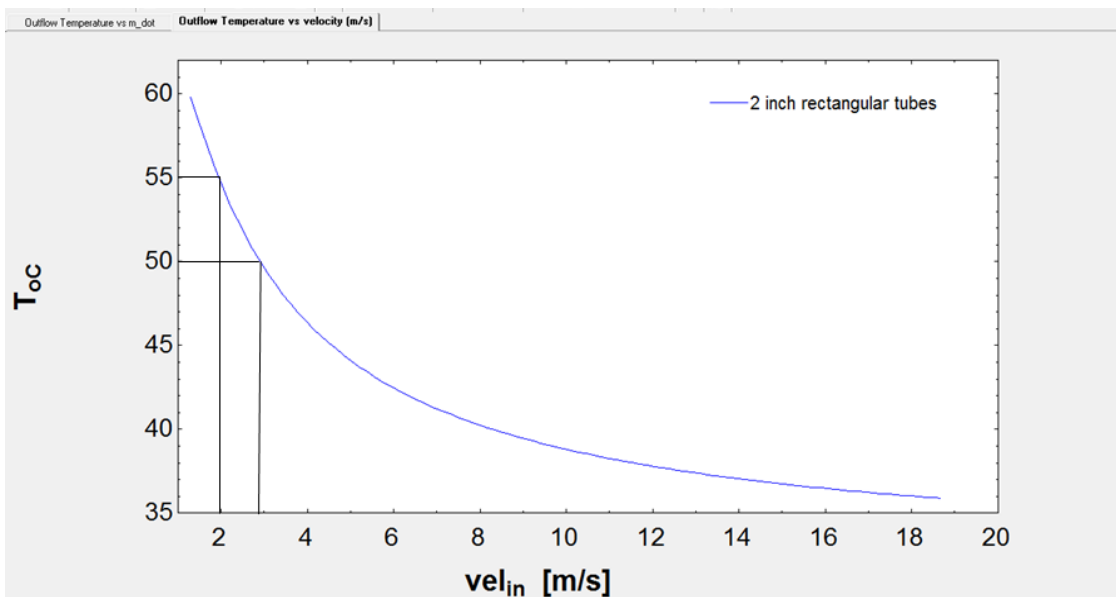


Figure 17: Output temperature vs velocity inlet plot for the two-inch rectangular tubes design

The figures were also plotted for the 6 one-inch rectangular tubes and the 12 half-inch rectangular tubes designs. The two figures below are for the one-inch rectangular tube design.

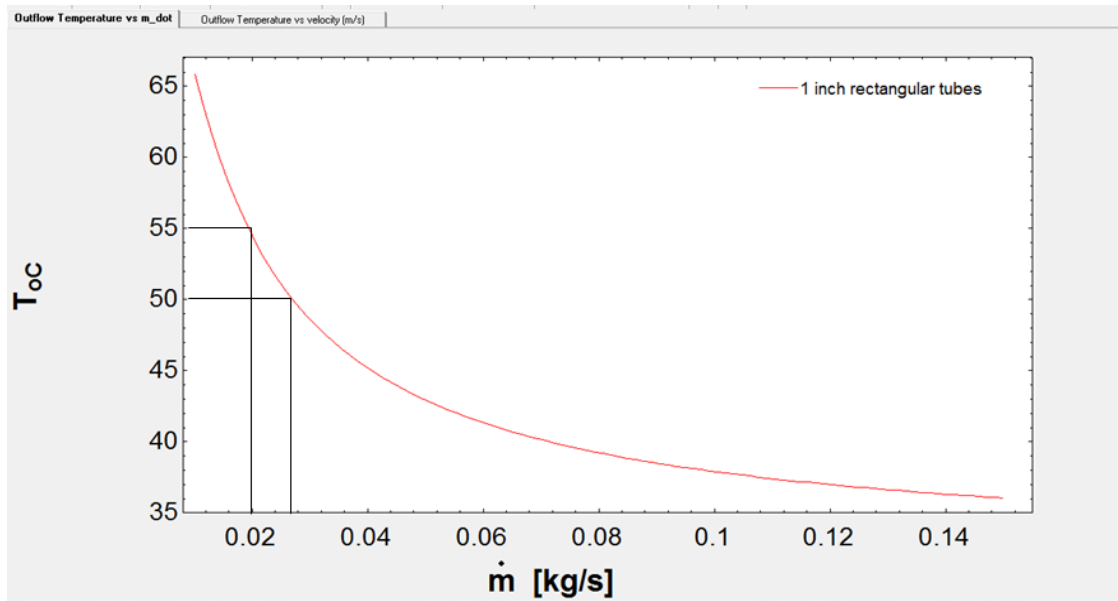


Figure 18: Temperature output vs total mass flow rate plot for the one-inch rectangular tubes design

Figure 18 shows that the range of total mass flow rate of interest is between 0.019 kg/s to 0.027 kg/s and Figure 19 shows the velocity is between 5.4 m/s and 7.5 m/s in order to reach the range of temperature desired.

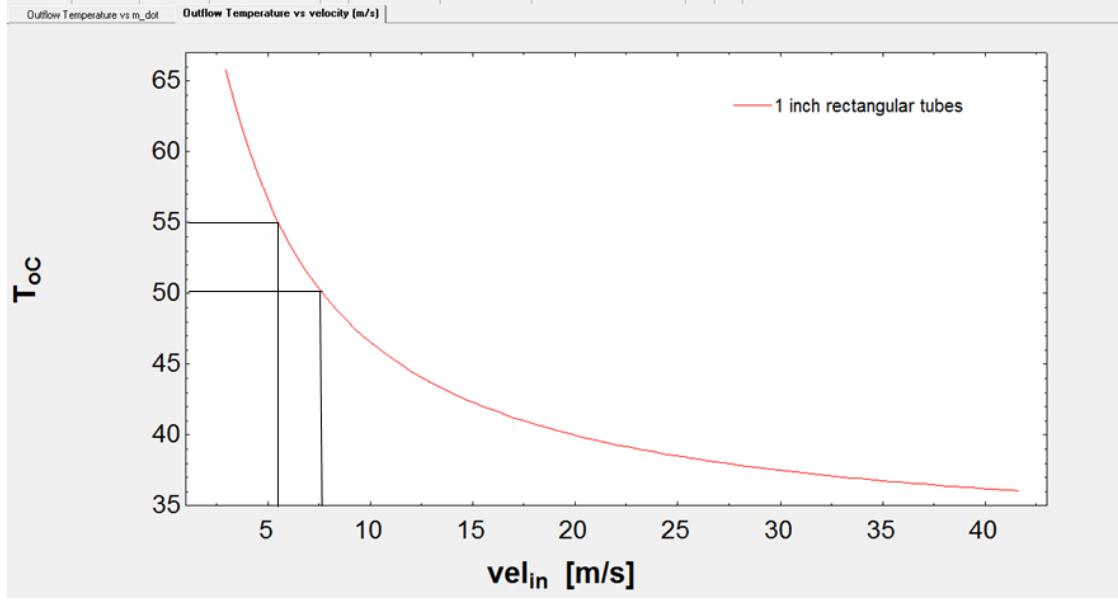


Figure 19: Temperature output vs velocity inlet for the one-inch rectangular tubes design

For the half-inch rectangular tube the total mass flow rate range is very similar to that of the one-inch rectangular tubes design, from 0.019 kg/s to 0.027 kg/s, shown in Figure 20.

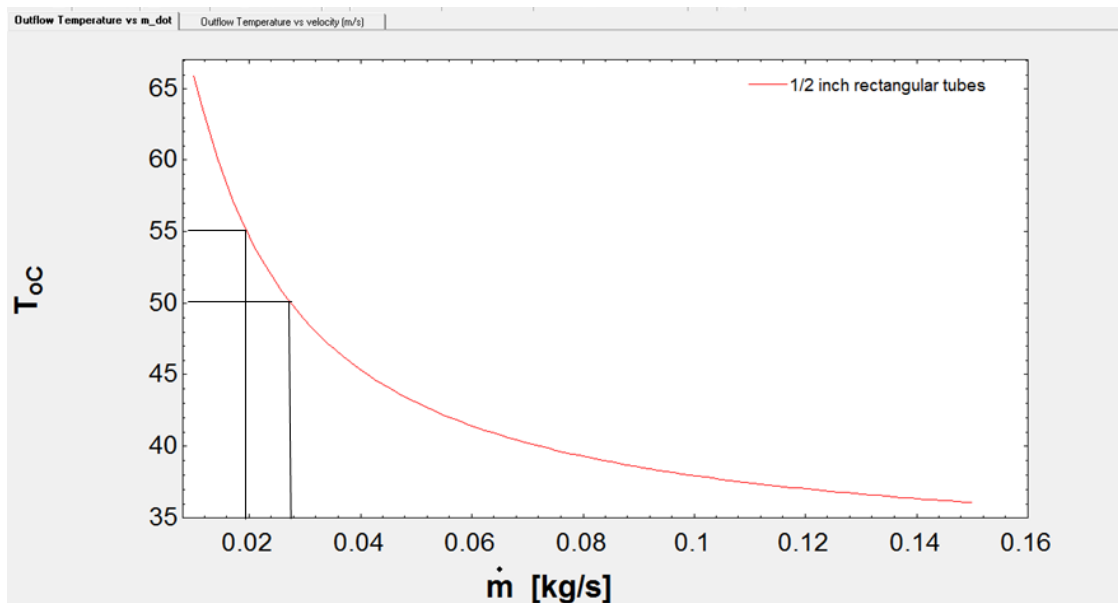


Figure 20: Temperature output vs total mass flow rate for the half-inch rectangular tubes design

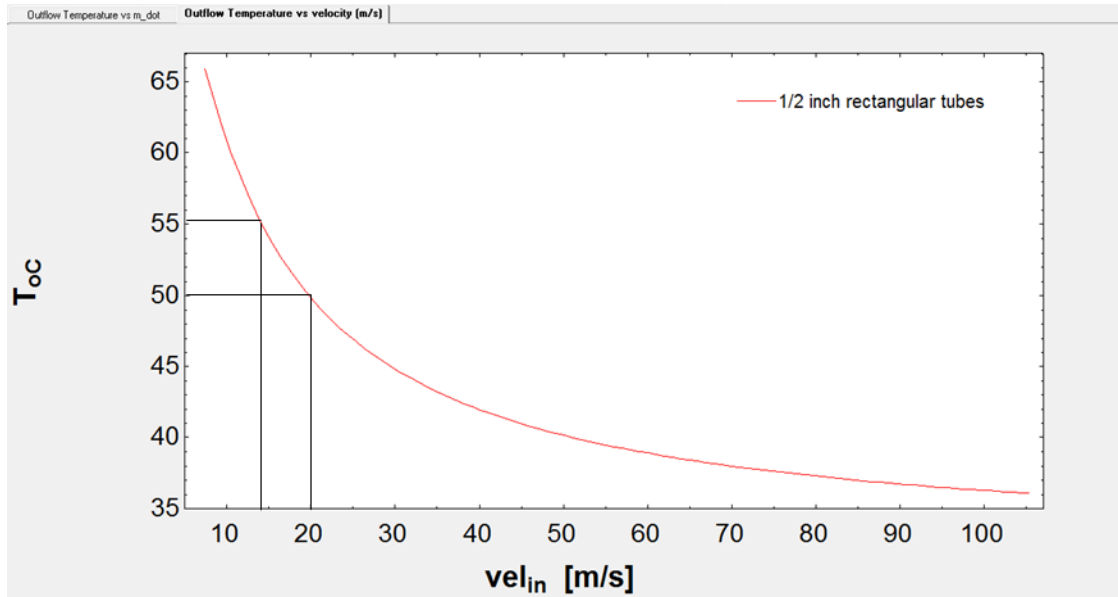


Figure 21: Temperature output vs velocity inlet for half-inch rectangular tubes design

The velocity inlet for each tube differs greatly for the half-inch rectangular tube as opposed to the total mass flow rate. Figure 21 shows that the velocity inlet for the range of 50 °C to 55 °C is from 14 m/s to 19.6 m/s. By observing these plots it is easy to see that the one-inch and half-inch rectangular tubes designs are better since their mass flow rate compared to that of the two-inch rectangular tubes design are greater for the temperature range of interest, 50 °C to 55 °C. In addition to these observations, temperature output vs pressure drop plots were drawn for the one-inch and half-inch rectangular tubes designs.

The total mass flow rates for these designs are virtually the same. Before choosing the 6 one-inch rectangular tubes design the temperature output vs pressure drop plots were compared. Figure 22 and Figure 23 show these plots for the one-inch and the half-inch rectangular tubes designs, respectively.

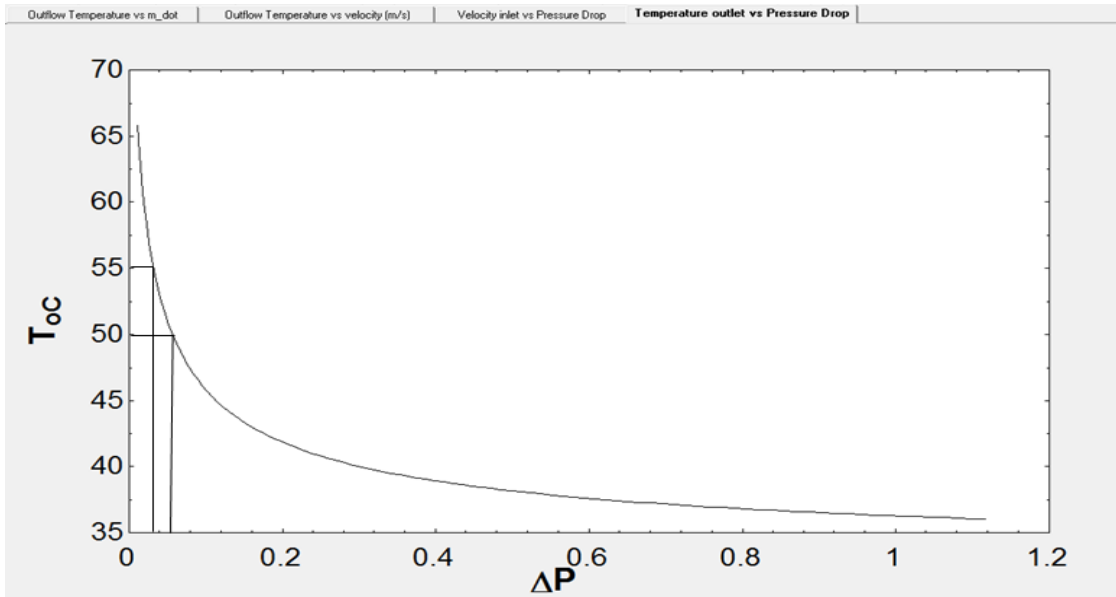


Figure 22: Temperature output vs pressure drop for each one-inch rectangular tube in atm.

When observing both figures, Figure 22 and Figure 23, it is easy to appreciate the difference in pressure drop when comparing them. Figure 22 demonstrates a lower pressure drop than that shown in Figure 23.

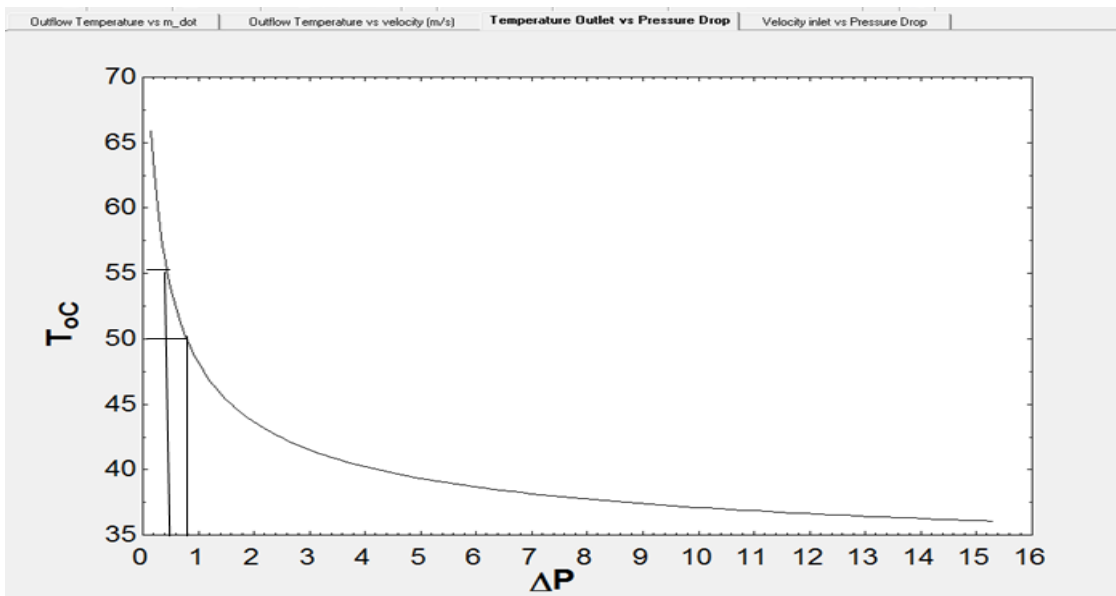


Figure 23: Temperature output vs pressure drop for each half-inch rectangular tube in atm.

It is easy to relate these temperatures to their respective velocities by observing Figure 19, for the one-inch rectangular tube design, Figure 21, for the half-inch tube design. The velocities are 5.4 m/s to 7.5 m/s, for the one-inch tube design, and 14 m/s to 19.6 m/s, for the half-inch tube design. These pressure drops are for a single tube and by pure observation the power required by a fan for the one-inch rectangular tube design is then less than that of the half-inch rectangular tube design. With this in mind, in addition to the motives mentioned earlier in this chapter, the 6 one-inch tubes design was chosen for additional analysis, a thermal model in Star-CCM+.

5.3.2 Solar Collector design - Computational modeling of the receivers

The involvement of radiation, convection, and conduction in the heat loss process makes it difficult to develop a purely analytical model, the interaction of these three modes is possible by using a numerical analysis approach, hence computational modeling [34]. The physical parameters of the model are consistent with those of the design in the thermal network analysis, which are shown in Appendix 7.6. The solution to this model gave extra support to the thermal network analysis solved in the previous section (5.3.1).

The boundary conditions for the fluid and solid region were applied, a mass flow rate input boundary and a pressure outlet for the fluid region, and environment boundary conditions for the external boundaries of the solid region. The latter permits the specification of the heat transfer coefficient for the convection occurring in the external side to the environment and the specification of the optical properties of the external side of the solids, emissivity, reflectivity and transmissivity (for the glass). Lastly, the input for the solar radiation is set at the interface between the air and the tubes (the set of tubes will be mentioned as the plate in this section) as a heat source.

These boundary conditions belong to a three dimensional steady state simulation. This simulation consists of the realizable $k - \epsilon$ turbulence model, along with the grey thermal radiation model available

in the Star-CCM+ software, which were explained in section 2.4. The turbulence flow model is solved in an uncoupled manner, or segregated, along with the segregated temperature model. In turn the energy model used for the solid is a segregated energy model, known in Star-CCM+ as segregated solid energy model. In order to solve these model a volume mesh had to be created and it can be observed in Figure 24. It has a base size of 0.008 m per element with a total of 2,800,928 elements.

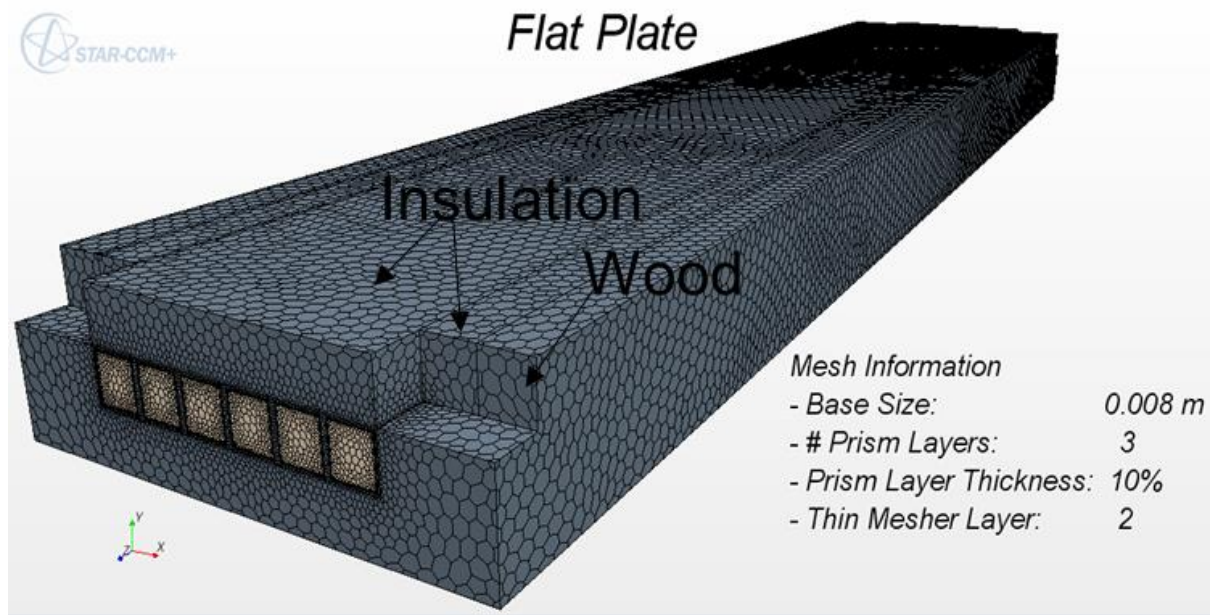


Figure 24: Three dimensional representation model of the volume mesh.

The solution for this simulation gave very close results to those given by the thermal network model. Figure 26 shows the temperature distribution in the outlet of each of the one-inch rectangular tubes and shows a very close similarity to the temperature outlet given in the thermal network analysis for a mass flow rate entrance of 0.003215 kg/s. The results for the thermal analysis are shown in Figure 25 and can be compared with simulation results shown in this section.

1	\dot{m}	2	\dot{V}	3	k_w	4	ϵ_w	5	vel_{in}	6	U_L	7	Re	8	T_{mp}	9	T_{pmC}	10	Q_u	11	$q_{convection}$	12	T_{oC}	13	ΔP
	[kg/s]		[m ³ /s]		[W/m-K]				[m/s]						[K]		[C]		[W]		[W]		[C]		[kPa]
	0.01929		0.00289		2.365		0.75		5.53		47.34		7260		328.9		55.72		445.7		531.4		54.97		0.03179

Figure 25: Results for the thermal network analysis for a total mass flow rate of 0.01929 kg/s (0.003215 kg/s for each tube). These results are obtained from the Equations Engineer Solver (EES) software

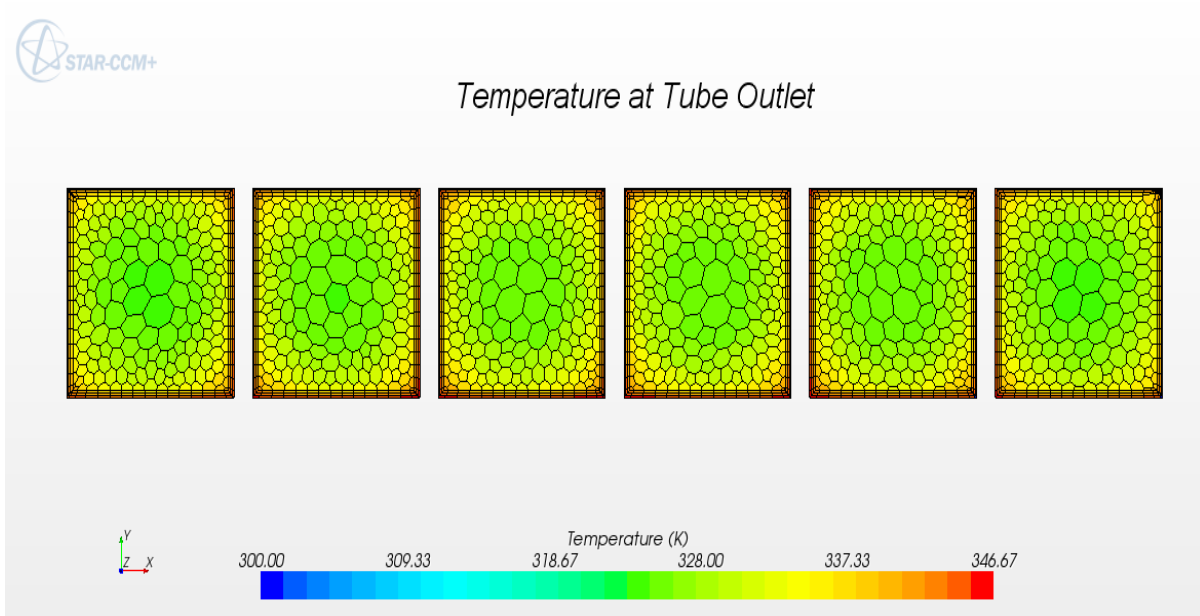


Figure 26: Temperature distribution at outlet of each one-inch tube.

The figure below (Figure 27) shows the air temperature change when it passes through the tubes. A clearer view is given in Figure 28.

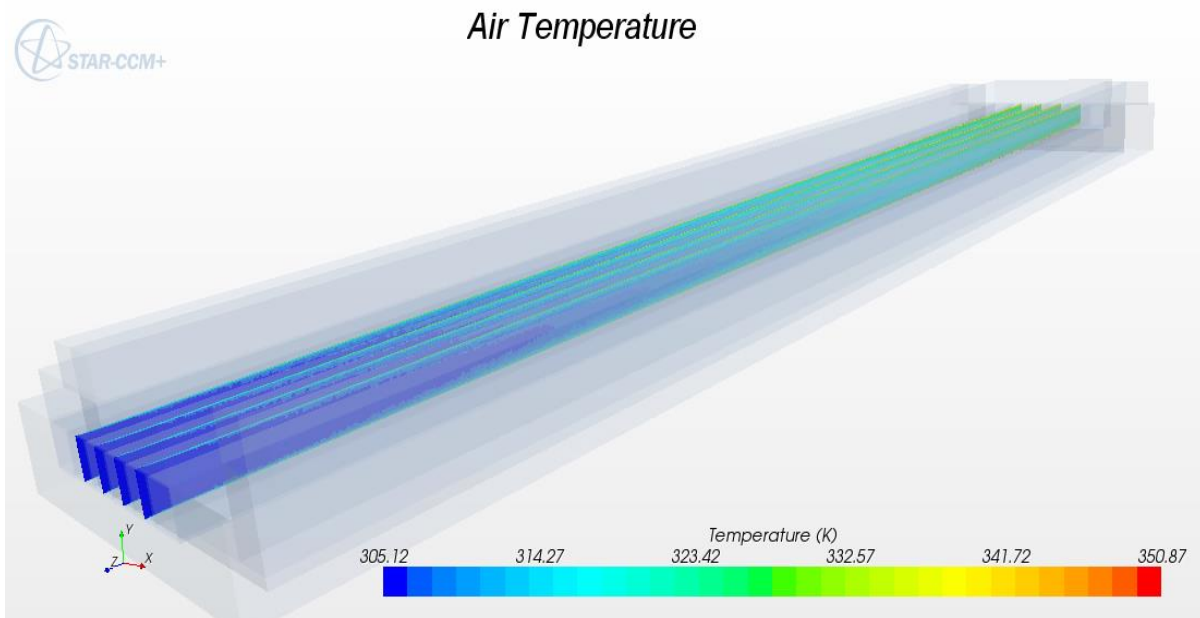


Figure 27: Shows how the temperature of the air changes when it passes through the tubes.

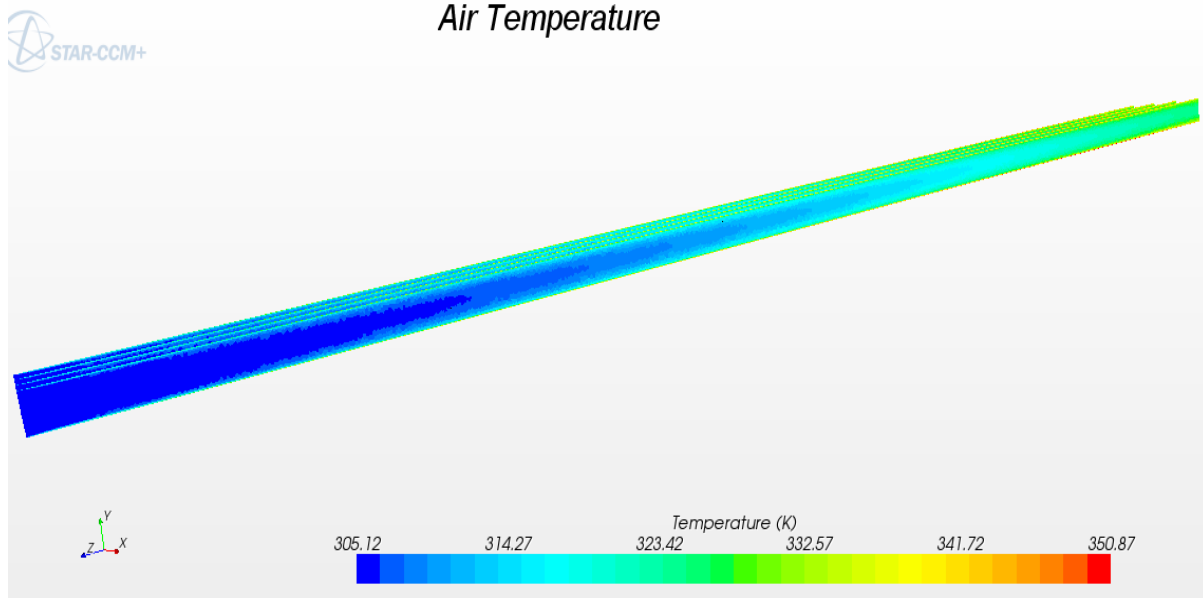


Figure 28: Air temperature when passing through the tubes, without the geometric outline of the collector.

Other results to compare are that of the velocity inlet and the pressure drop that occurs inside the tubes. The velocity inlet is shown to be around the same value as for the thermal network analysis (5.53 m/s for thermal network). The same happens with the pressure drop, where in the thermal network the pressure drop is of 31.79 Pa, while in the simulation is of 32.06 Pa. These results are best appreciated in Figure 29 and in Figure 30, respectively.

Knowing that the simulation functions properly, a second design was simulated. The same model was used, along with all its inputs and initial values. Only a small geometrical modification was implemented, the top insulation was deleted in order to install a second glass cover. In the model, a region of air was added on top of the tubes. The second glass cover then was placed on top of this new air region, this may be observed in Figure 31. All the values for the mesh generation were the same as the first model.

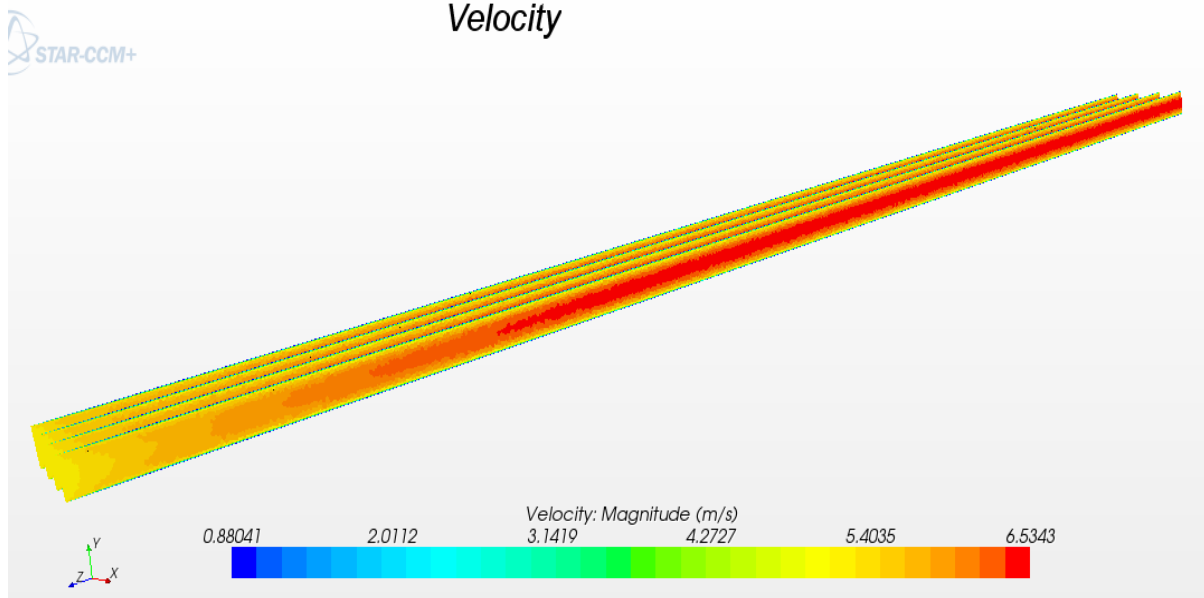


Figure 29: Velocity behavior inside the tubes.

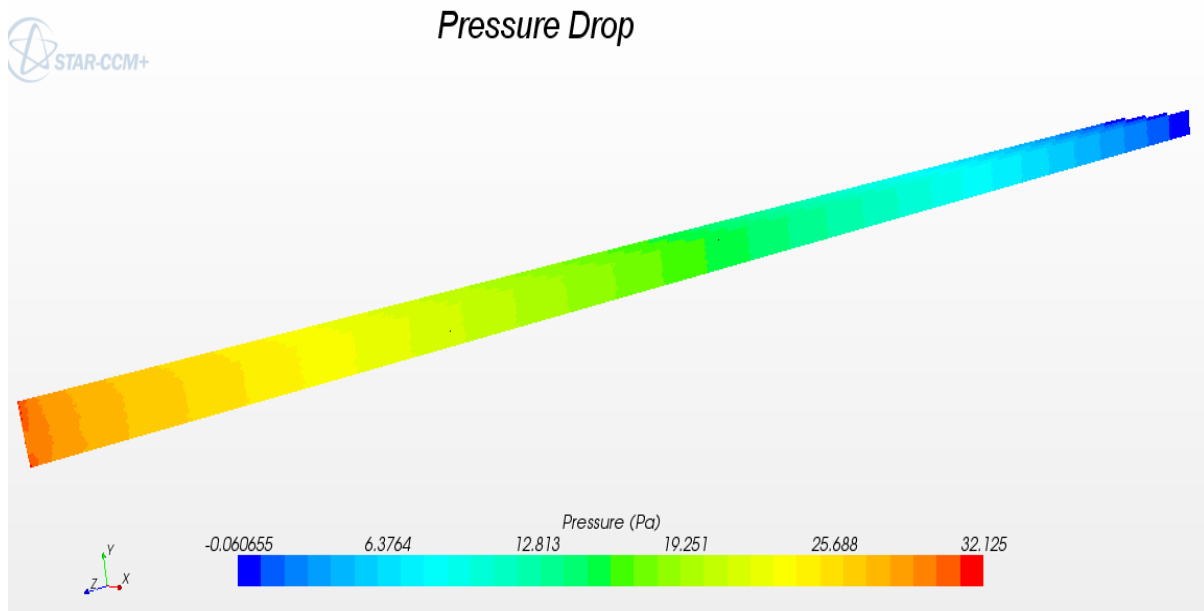


Figure 30: Pressure Drop

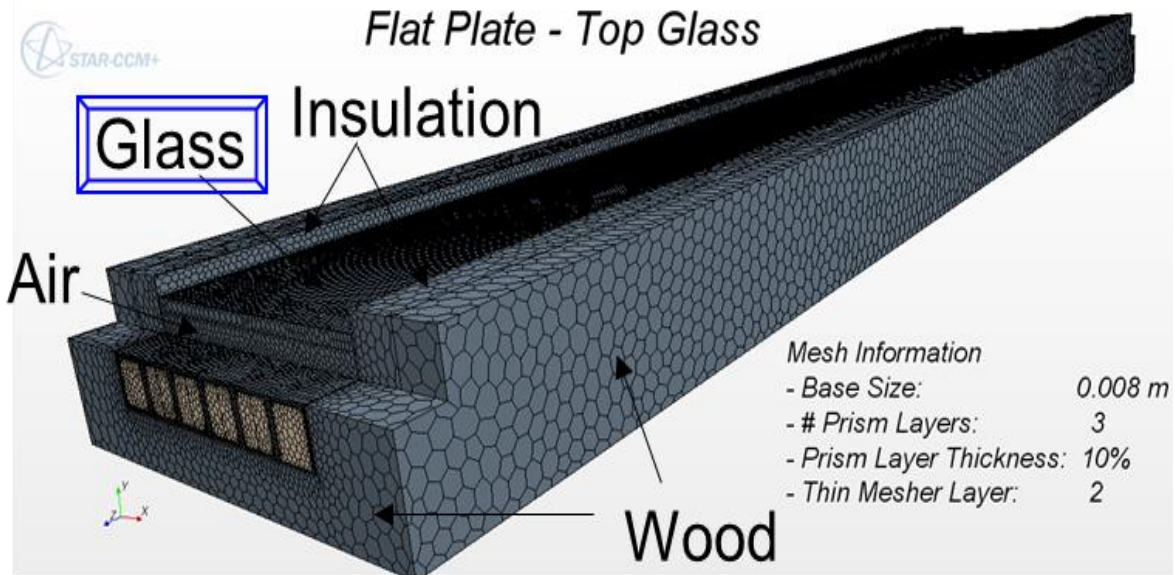


Figure 31: Volume mesh three dimensional representation of the second model (with glass in the top).

The temperature distribution for air at the outlet of each tube for this second collector is shown in Figure 32. By observing and comparing the mentioned figure with that of Figure 26, for the first collector, it is easily observed that the outlet air temperature for the second collector is greater than that for the first collector.

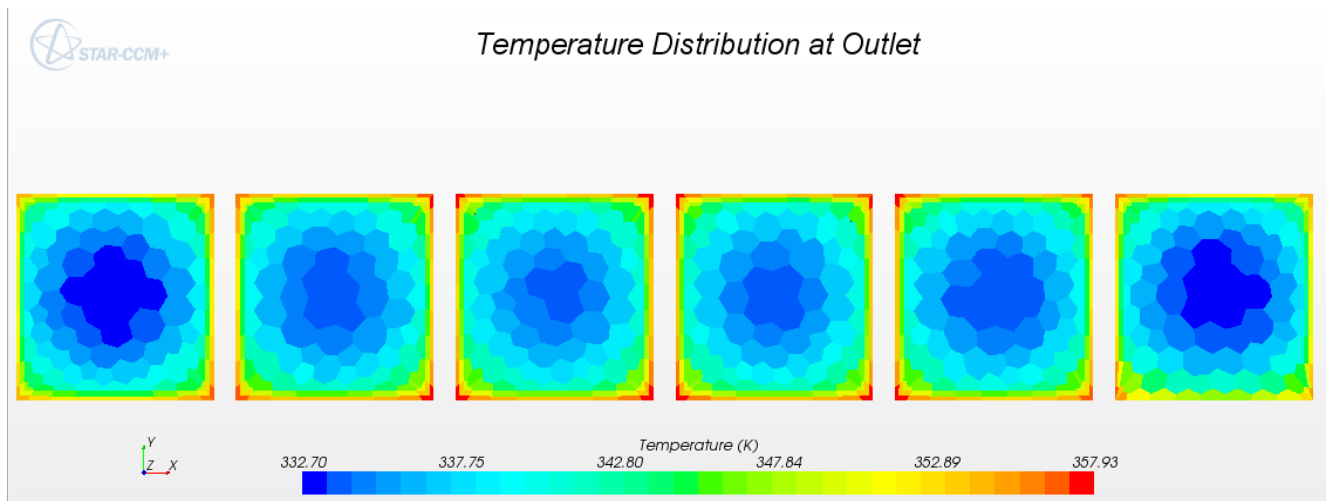


Figure 32: Air temperature at the outlet of each tube for the collector that has glass cover on the bottom and at the top.

To verify that the simulation is working properly the velocity and the pressure drop inside the tubes were compared. Figure 33 and Figure 34 show the velocity and the pressure drop, respectively.

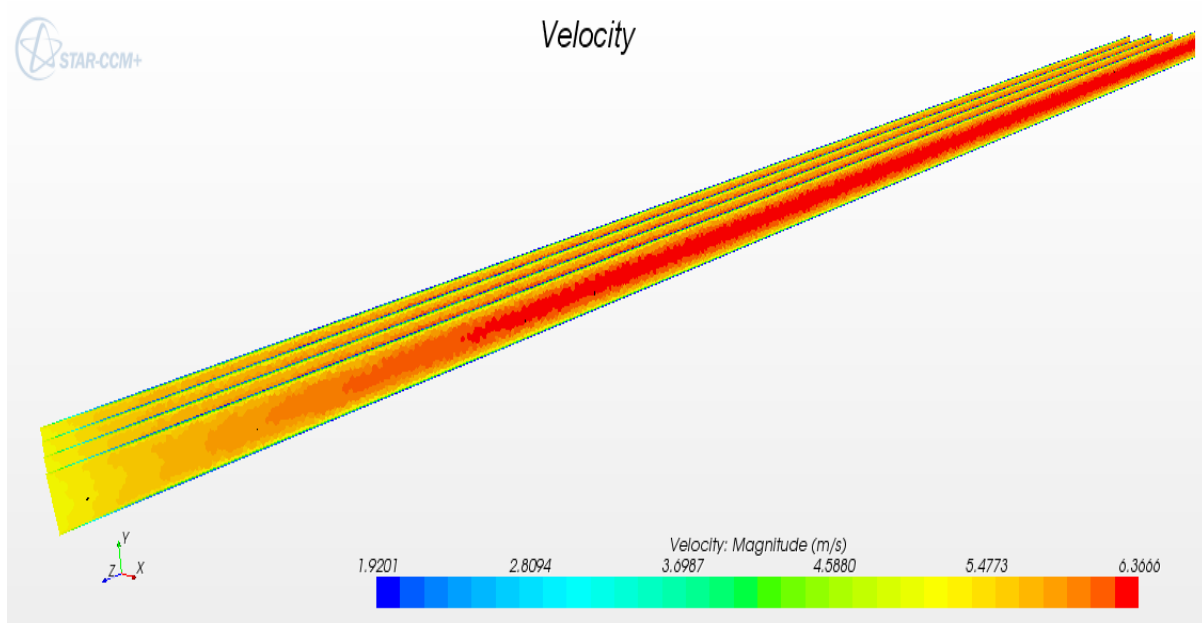


Figure 33: Velocity inside the tube.

These values should not and did not change when compared to the values of the first collector. Looking at Figure 33 it is observed that the inlet velocity lies around 5.2 m/s, the same as the first collector. The same was said for the pressure drop, where in the second collector it is of 33.56 Pa while the first is of 32.06 Pa. The difference are small enough to say that they agree with each other.

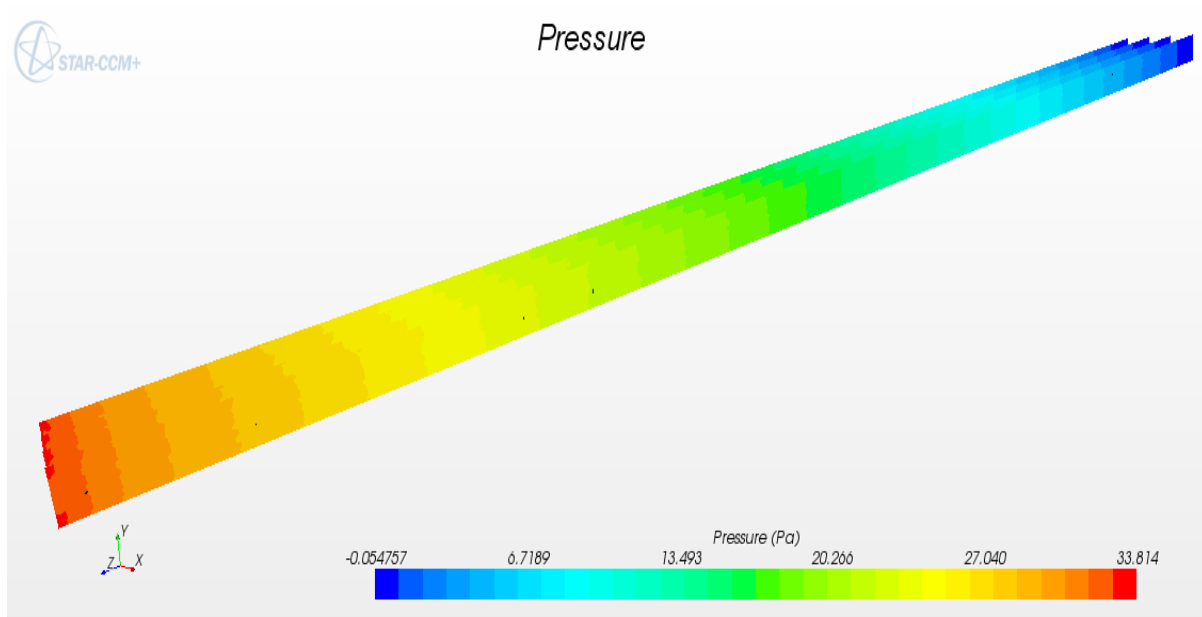


Figure 34: Pressure drop that occurs inside the tube.

These results show that the second collector, the collector with two cover glasses, might have a better thermal performance than the first collector. To prove this an experimentation was carried out, but before this a collector had to be manufactured. The purpose this second design was designed this way was for its convenience. By switching the glass for the insulation one creates a whole new collector. Chapter 5.4 discusses more about the manufacturing process.

5.4 Solar collector design – Collector manufacturing

As mentioned earlier, the collector was manufactured with materials that were easy to handle and to obtain. This included three ninety-six inch (96 in.) which were cut to six forty-seven inch tubes. The insulation was that of glass wool and the frame was made from wood. The thickness was of $\frac{3}{4}$ inch while its length varied depending on the part of the collector. The glass is regular commercial glass that was cut in a local shop. The images below (Figure 35 and Figure 36) show the collector during its manufacturing.



Figure 35: One end of the collector during the process of manufacturing



Figure 36: The collector during the process of manufacturing.

After finishing the manufacturing process the collector was finally assembled in the roof of the Stefani Building located at the University of Puerto Rico at Mayaguez. It was painted and installed along with an aluminum duct and a foam icebox. The icebox served as a flume, here two computer fans were installed in a way that air was being drawn out of the foam icebox. The foam and the duct were installed in the outlet of the collector, as shown in Figure 37 and Figure 38. The aluminum duct was covered with the same insulation material as the collector in order to minimize thermal losses to the environment. Finally, after testing the system experiments were conducted in order to proof the systems functionality. Section 5.5 discusses the results from the experiments carried out.



Figure 37: Complete assembly of the Linear Fresnel Reflector System situated in the roof of Stefani Building at the University of Puerto Rico at Mayaguez.



Figure 38: Solar air collector. The image shows the incident radiation that is reflected from the mirrors.

5.5 Experiment and results

Experiments were carried out during the days of the 13th of October 2014 through the 15th of October 2014 and on the 16th of October 2014. Two sets of experiments were taken each day from eight in the morning until Noon. The data collected included the total radiation, the ambient temperature, and the air temperature at the output of the collector which is at the end of the aluminum duct.

The velocity at the entrance of each tube was also measured, using an anemometer. These measurements were taken at the beginning of each experiment, before the motors were turned on (No radiation incident on the plate), and at the end of them. They were also measured between the sets of experiments; in other words, these measurements were measured three times. This was done to ensure that the velocities were in fact constant or nearly constant. Figure 39 shows an image measuring the inlet velocity for one of the tubes.



Figure 39: Measuring the inlet of the tubes with an anemometer probe.

On the first two days the second design was installed, where the glass was located on the top part of the collector as shown in Figure 40. This meant that total radiation was also incident on the top part of the plate increasing the overall solar energy incident on the plate (tubes).

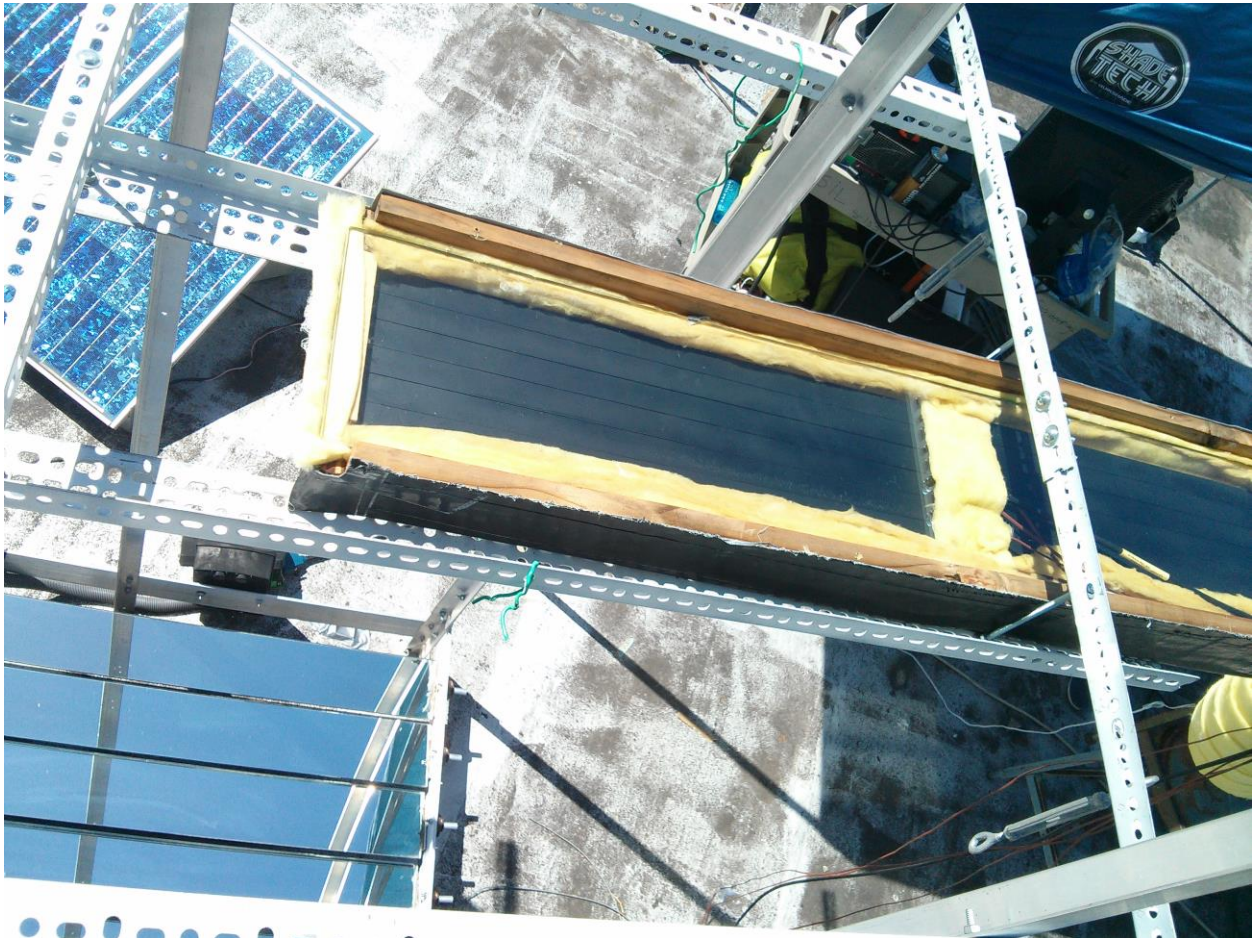


Figure 40: Collector with a glass cover on the top.

The results for this collector are shown in Figure 41 and Figure 42, for the first and second set for the experiments carried on the 13th of October of 2014, respectively. In the plot there are two sets of data, the blue is for the temperature at the outlet of the duct, in Celsius, and the red is for the total radiation, in kW/m². Both data are for the same time allowing an appreciation of the behavior of the collector throughout the day.

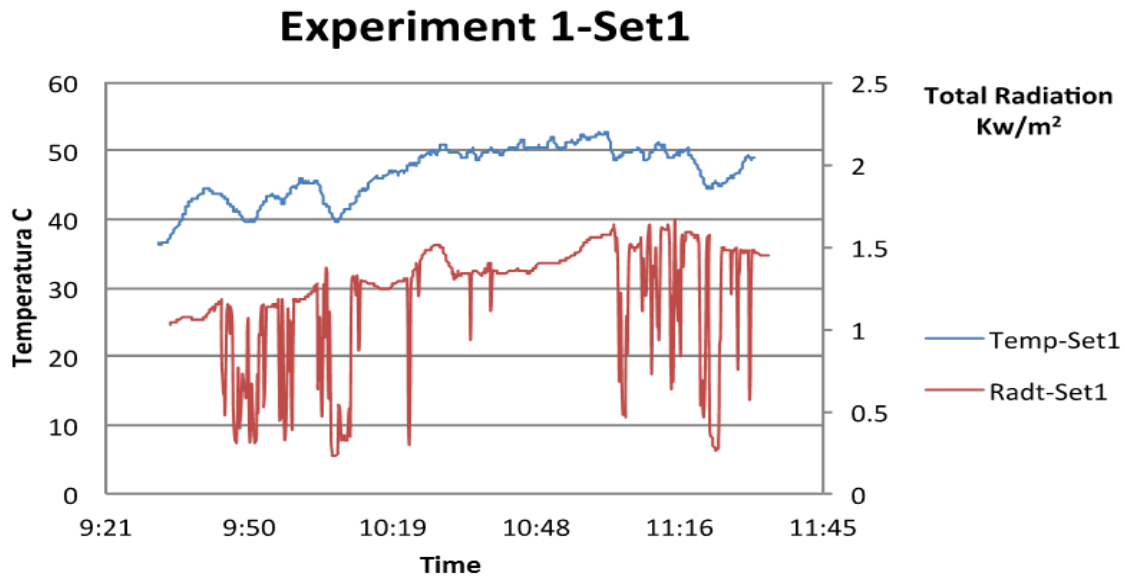


Figure 41: First set of experimental results for the collector with 2 glasses (on the bottom and on top of the plate) for the 13th of October, 2014. The blue data indicates the air temperature at the outlet of the duct and the red represents the total radiation.

The first set of experiment one shows that it reaches the desired 50°C at around 10:25 am, about an hour from when the system started. For set 2, the temperature of the air was already high due to the fact that the system kept running while the inlet velocities were being measured. An important observation that can be appreciated when observing Figure 41 Figure 42 is that the collector reacts quickly to the solar radiation. When the solar radiation is low, the collector loses heat almost at an instant. This is seen in Figure 41 at around 9:50 am, 10:10 am, and again after 11 am. In between 10:19 and 11 am the air temperature had a steady small increment, behaving very similar to that of the solar radiation for that period of time.

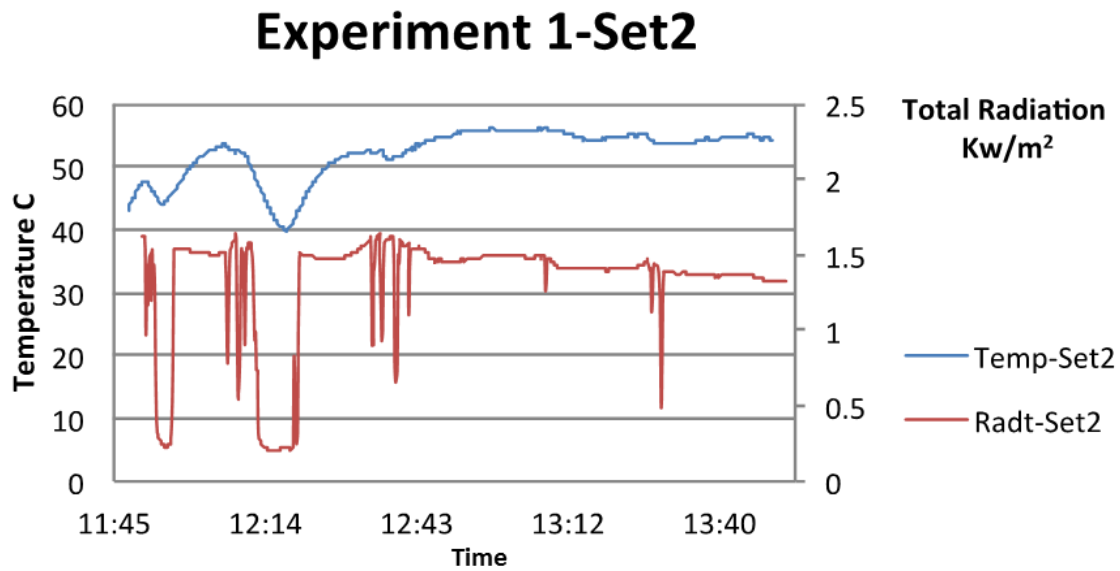


Figure 42: Second set of experimental results for the collector with 2 glasses (on the bottom and on top of the plate) for the 13th of October 2014. The blue data indicates the air temperature at the outlet of the duct and the red represents the total radiation.

The same behavior is seen in set two of the first experiment, especially around 12:14 pm. Now, something interesting happened after 12:43, the plot shows how the solar radiation starts decreasing steadily for the remainder of the time, yet, the air temperature maintained its temperature at around 55°C. To see if this behavior is typical for this collector the plots for the second experiment should be analyzed. Figure 43 plots the data of the first set for the second experiment.

The data for this second experiment, shown in Figure 43 and Figure 44, demonstrates the same behavior shown in both sets of the first experiment. A quick reaction to the solar radiation and a steady increase in the air temperature as long as there is no sudden changes in the amount of solar radiation. The second set of experiment has the same behavior as the second set of experiment one, where after 12 noon the solar radiation steadily decrease, but the air temperature in the outlet maintains a steady temperature, this time closer to 60°C. This temperature is perfect since it means that an increase in the mass flow rate is needed in order to lower the temperature to the desired value of 55°C, which in turn

equals to a greater quantity of air with the desired temperature to remove the humidity of the coffee beans for this particular case.

Experiment 2-Set1

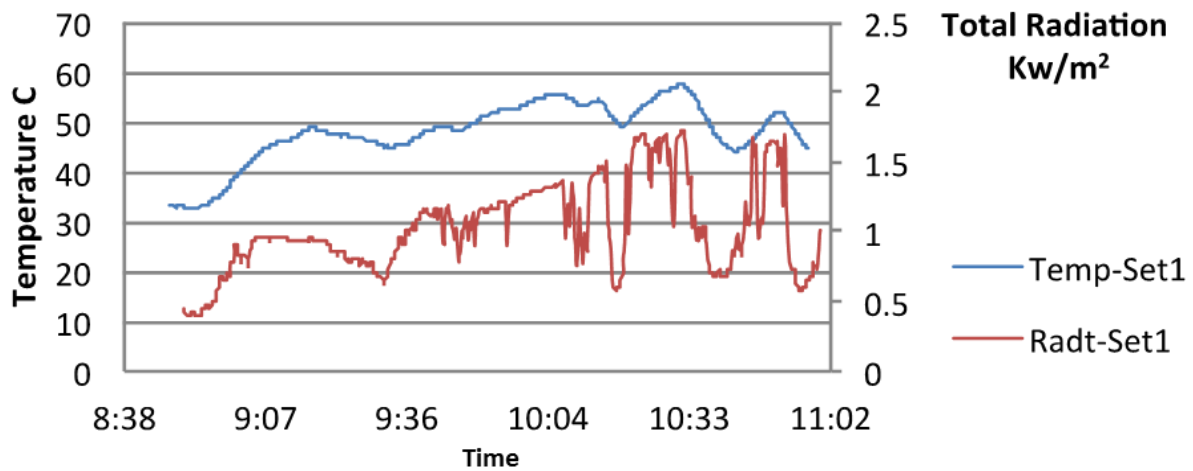


Figure 43: Outlet air temperature and solar radiation data for the first set of experiments two. This experiment was carried out the 14th of October of 2014. Blue line represents the outlet air temperature while the red represents the total solar radiation.

Experiment 2-Set2

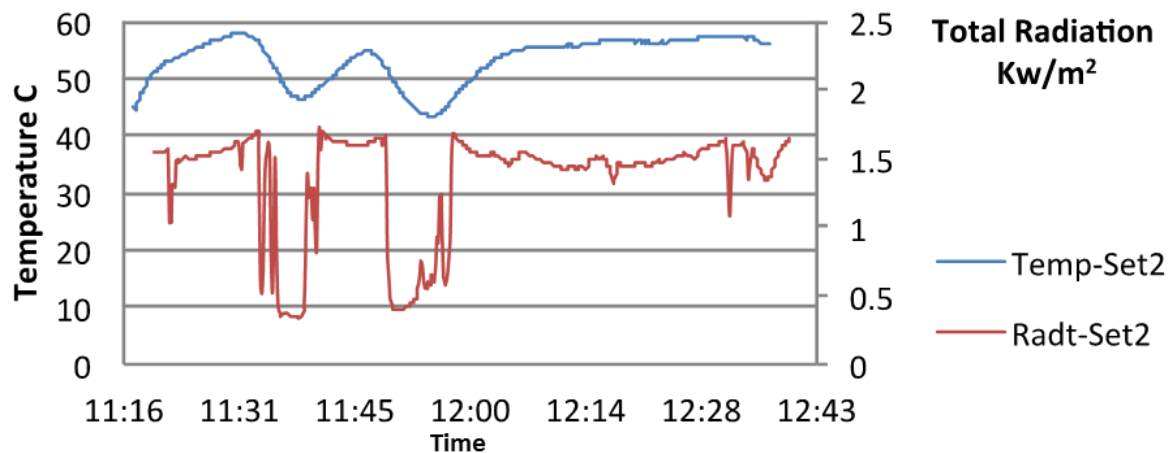


Figure 44: Outlet air temperature and solar radiation data for the second set of experiments two, with the two cover glass collector. This experiment was carried out the 14th of October of 2014. Blue line represents the outlet air temperature while the red represents the total solar radiation.

For the third experiment the collector was changed, it had only one glass cover (in the bottom) and the top was covered by insulation. The first observation when analyzing these plots is that the temperature of the air does not reach the same value as the collector with the two glass covers. It is hard to analyze if this is due to the design of the collector by examining the first set of the three experiments. If we consider Figure 45 we can appreciate the steady increasing ramp of total radiation that hits the 1 kW/m^2 at around 9:10 am, about 50 minutes after the start of the experiment. When observing set one of experiment two, one sees that it gets closer to the 1 kW/m^2 faster and maintains this value for 10 to 15 minutes, it does not have a slow steady increase like seen in Figure 45 and by looking at Figure 41 it is easy to see that it has many radiation drops, making it incomparable with the other first sets.

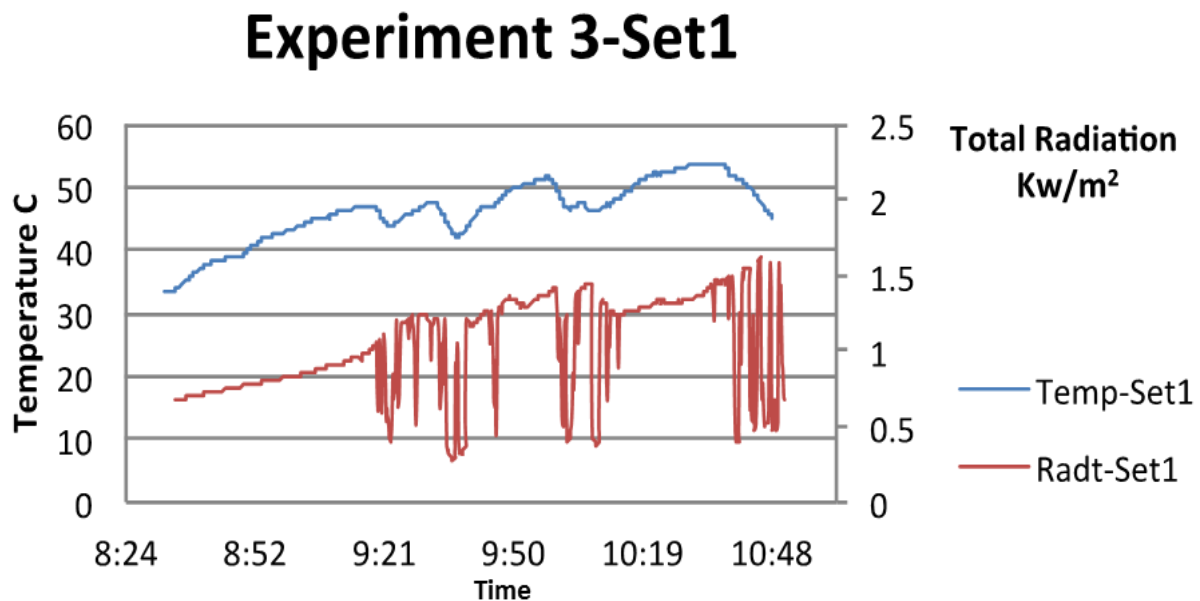


Figure 45: Outlet air temperature and solar radiation data for the first set of experiments three, with the collector with one glass cover, in the bottom. This experiment was carried out the 15th of October of 2014. Blue line represents the outlet air temperature while the red represents the total solar radiation.

Aside from this, the collector does reach the desired temperature value, 50°C . It does so at around 9:50 am. It might have reached it sooner but there were many total radiation drops before this time. The other time interval where the air temperature reached 50°C was around 10:19 am until close to

10:48, when the total radiation starts changing dramatically. During this time the air temperature exceeds the 50°C, it reached close to 53°C. If these sudden drops of total radiation were not present, instead a steady value of it like seen in the first two experiments, this air temperature might have stayed steady also, it might have increased close to those temperatures shown in the first two experiments.

When turning our attention to the second set of the third experiment, Figure 46, we see that it is not possible to justify that the reason the collector with only one cover glass, in the bottom of the collector, reaches lower temperature compared to the two glass cover collector is due to its design. In fact, the air temperature reaches 50°C at around 11:31 am even after the total radiation suffered several drops before this time.

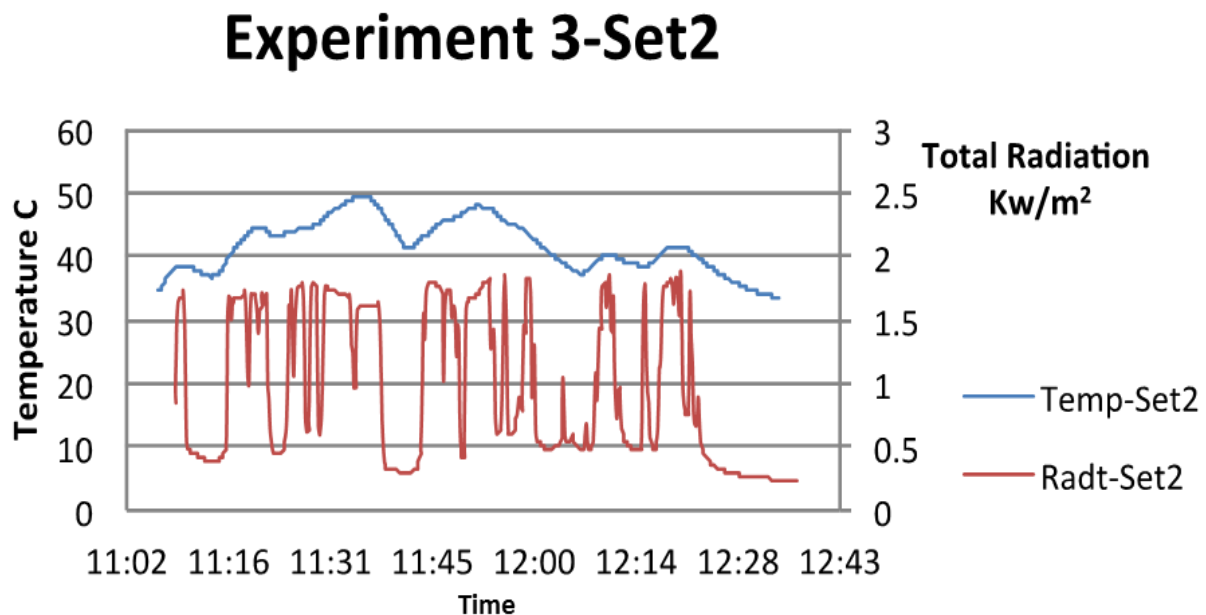


Figure 46: Outlet air temperature and solar radiation data for the second set of experiments three, with the collector with one glass cover, in the bottom. This experiment was carried out the 15th of October of 2014. Blue line represents the outlet air temperature while the red represents the total solar radiation.

It almost reaches the 50°C mark at a little before Noon, again, even when the total radiation was not stable. It is not possible to compare the data from Figure 46 to those from the second set of the first two experiments, Figure 42 and Figure 44, since by clear observation the total radiation in Figure 46 varies too much when compared to the other two. Even if one grabs specific data groups, for example:

data that lie between 1 kW/m^2 and 1.25 kW/m^2 for a similar amount of time, there are other variables in that affect the results, making it very difficult to make a direct comparison.

Other than that Figure 47 shows a nice smooth ramp for virtually all the morning. We can see how the air temperature gradually rises as the total radiation steadily increases. The air temperature rises until $50 \text{ }^\circ\text{C}$, its maximum, and if this data is closely examined one can observe that it maintained a steady temperature reading, from 49°C to 50°C , between 10:15 am up till 10:50 am, the second total radiation drop. This is similar to the data demonstrated in Figure 45, which is an expected behavior since it is the same collector.

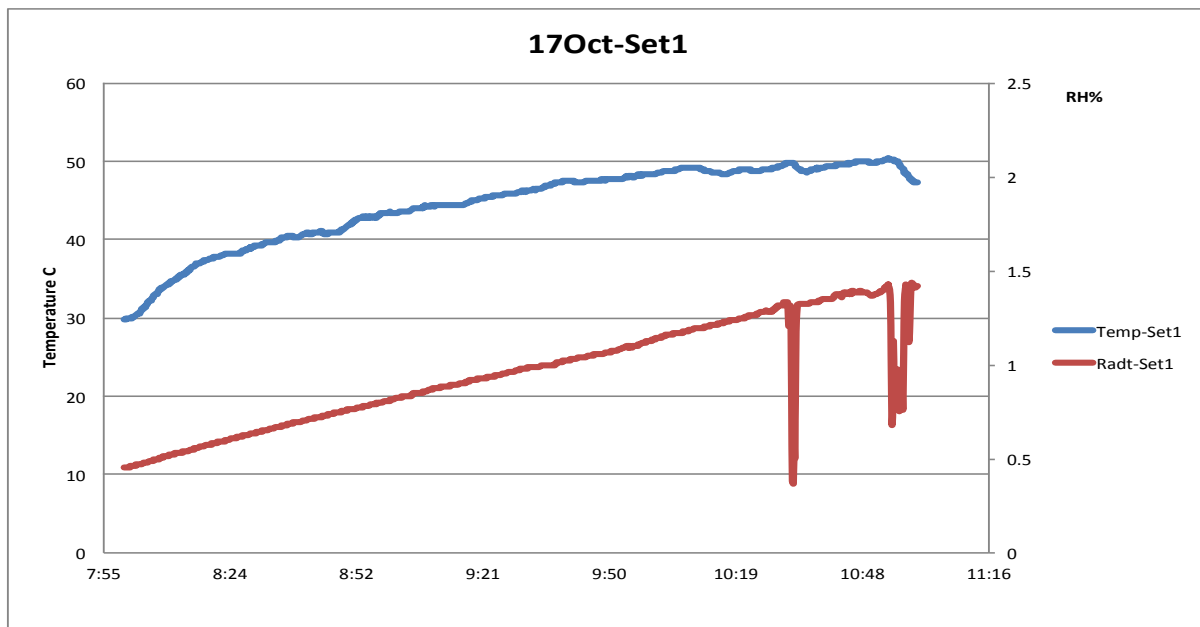


Figure 47: Outlet air temperature and solar radiation data for the first set of experiment four, with the collector with one glass cover, in the bottom. The experiment was carried out on the 17th of October of 2014. Blue line represents the outlet air temperature while the red represents the total solar radiation.

The data from the second set of the fourth experiment is shown in Figure 48. The total radiation data for this second set is well below the desired values. Two distinct drops can be perceived when analyzing this data set. One starts from the beginning of the set until around 11:35 and the other from around 11:38 am to 11:48 am. In addition, after this time the total radiation varies throughout the rest of the run. Even with this variation the air temperature was risen until the last total radiation drop

demonstrating that the collector may still have the opportunity to rise to the desired temperature of 50°C if these variations in total radiation are constant, although the best scenario will always be to have constant data as shown in Figure 47.

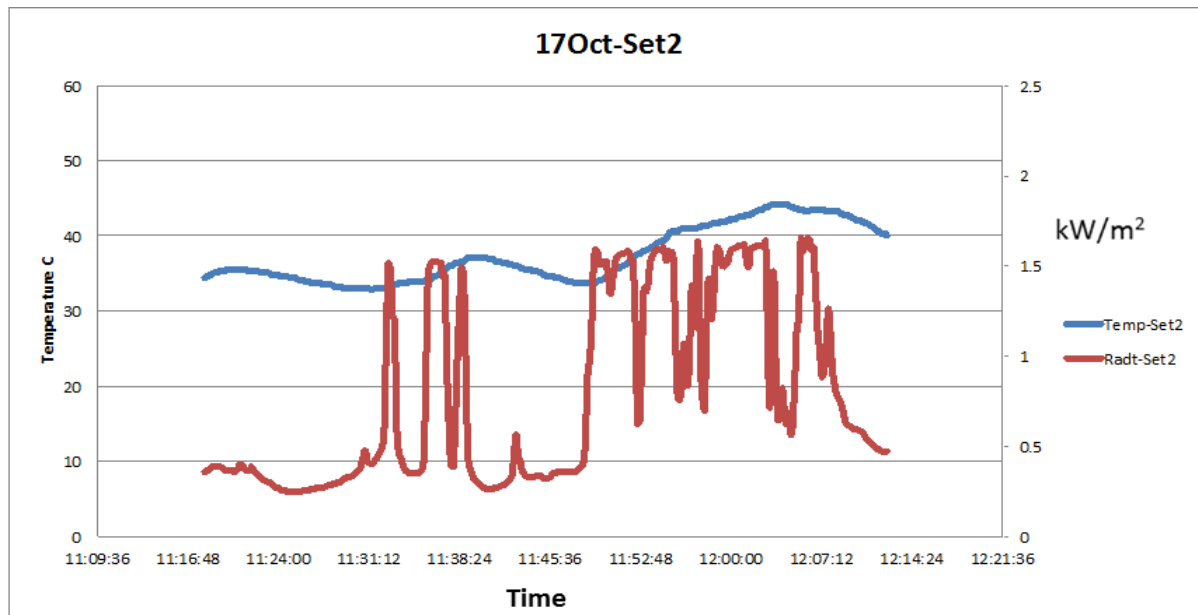


Figure 48: Outlet air temperature and solar radiation data for the second set of experiment four, with the collector with one glass cover, in the bottom. This experiment was carried out on the 17th of October of 2014. Blue line represents the outlet air temperature while the red represents the total solar radiation.

It is very important to mention that for these collectors is that both collectors reached the 50 °C when the total radiation reached a threshold of 1.25 kW/m². This is observed in all four experiments. Both collectors reached the desired temperature mentioned, thus the Linear Fresnel Reflector, can be considered a viable system to dry coffee.

VI. Conclusion

An extensive overview of the development of a Linear Fresnel Reflector prototype was presented in the present document. It was designed, manufactured, and tested with two collectors.

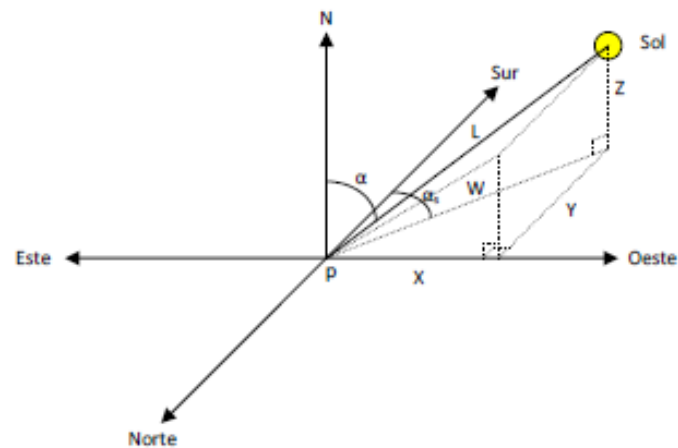
A steady-state thermal network analysis was used to compare several design ideas for the collectors. Three different designs were analyzed and compared. The prevailing design, consisting of 6 one-inch rectangular tubes, was then modeled using Star-CCM+ software. The results of this simulation came into good agreement with the thermal network solution. Knowing that the simulation was working properly a second design was simulated. According to the simulation this second design had better thermal performance than the first

Experiments were carried out to test the thermal performance of these collectors and see if the second design outperformed the first design. These experiments showed that both collectors used in the Linear Fresnel System reached temperatures of 50°, fulfilling the final objective.

VII. Appendix

7.1 Solar Tracking Angles

. The following are the equations used to calculate the inclination angles for the mirrors. This formulation and graph were created by Alexander Rivera Jiménez and Christian J Correa Torres and was completed as a requirement for a class given by Dr. Agustin Irizarry.

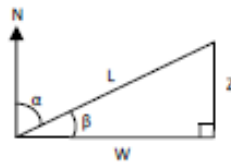


Nomenclatura:

α_s = Ángulo de azimuto

α = Ángulo de zenith

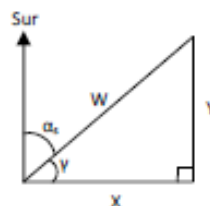
θ_l = Ángulo entre la normal de la tierra y la proyección de la luz incidente en un plano vertical visto de norte a sur



$$\beta = 90 - \alpha$$

$$W = L * \cos(\beta)$$

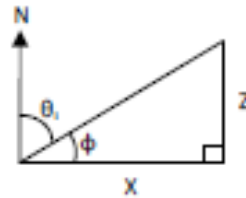
$$Z = L * \sin(\beta)$$



$$\gamma = 90 - \alpha_s$$

$$X = W * \cos(\gamma)$$

$$Y = L * \sin(\gamma)$$



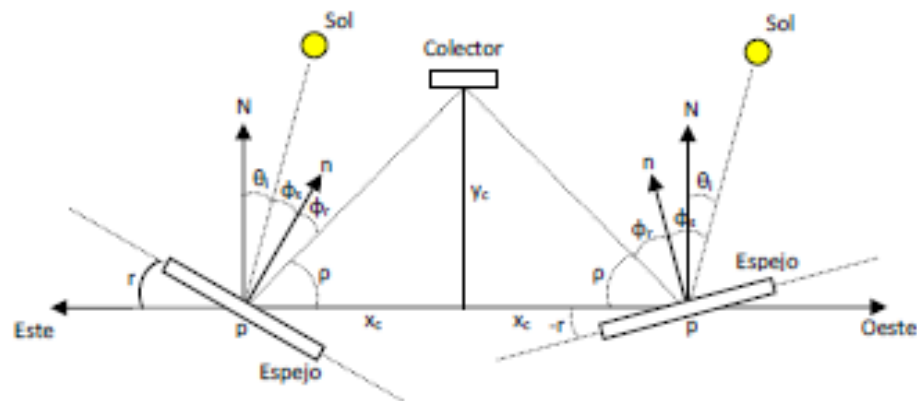
$$\emptyset = 90 - \theta_i$$

$$\tan(\emptyset) = \tan(90 - \theta_i) = \cot(\theta_i) = \frac{Z}{X}$$

$$\tan(\theta_i) = \frac{X}{Z} = \frac{[W * \cos(\gamma)]}{[L * \sin(\beta)]} = \frac{[L * \cos(\beta) * \cos(\gamma)]}{[L * \sin(\beta)]} = \frac{[\cos(\beta) * \cos(\gamma)]}{[\sin(\beta)]} = \cot(\beta) * \cos(\gamma)$$

$$\tan(\theta_i) = \cot(\beta) * \cos(\gamma) = \cot(90 - \alpha) * \cos(90 - \alpha_s)$$

$$\tan(\theta_i) = \tan(\alpha) * \sin(\alpha_s) \quad [1]$$



Caso 1: Espejo en un punto p al este del colector.

$$\emptyset_s = \emptyset_r$$

$$r - \theta_i = 90^\circ - r - \rho$$

$$r = \frac{(\theta_i - \rho + 90^\circ)}{2} \quad [2.1]$$

Caso 2: Espejo en un punto p al oeste del colector.

$$\emptyset_s = \emptyset_r$$

$$\theta_i + (-r) = 90^\circ - (-r) - \rho$$

$$r = \frac{(\theta_i + \rho - 90^\circ)}{2} \quad [2.2]$$

7.2 Solar Tracking Algorithm

The following algorithm was created for the sole purpose of tracking the Sun with the Linear Fresnel Reflector's mirror.

```

clc

xc(1)=0.28; xc(2)=0.14; xc(3)=0.28; xc(4)=0.42; xc(5)=0.60; %Horizaontal
distance(m) from the center of the collector to the center of the mirrors,
positive being the West.
yc=1.6; %Vertical distance from the center of the central mirror to the
collector.

hh=08; mm=00; ss=0; %Initial hour
c=fix(clock);
i=0; %Number of iterations

archivo(1)=fopen('C:\Documents and Settings\Administrator\Desktop\MATLAB
Data\Data1.txt','w');
archivo(2)=fopen('C:\Documents and Settings\Administrator\Desktop\MATLAB
Data\Data2.txt','w');
archivo(3)=fopen('C:\Documents and Settings\Administrator\Desktop\MATLAB
Data\Data3.txt','w');
archivo(4)=fopen('C:\Documents and Settings\Administrator\Desktop\MATLAB
Data\Data4.txt','w');
archivo(5)=fopen('C:\Documents and Settings\Administrator\Desktop\MATLAB
Data\Data5.txt','w');

d=0;
for ite=1:5
    while hh<16

        time.year=c(1); %Year
        time.month=c(2); %Month
        time.day=c(3); %Day
        time.hour=hh; %Hour
        time.min=mm; %Minute
        time.sec=ss; %Seconds
        time.UTC=-4; %Zone difference with respect to Greenwich
        location.latitude=18.21;
        location.longitude=-67.14;
        location.altitude=12; % (m)

        sun_position(time, location); % Reda, I., Andreas, A. (2003)
program to calculate zenith and azimuth angle.
        zenith=ans.zenith;
        hisazimuth=ans.azimuth; %Angle with respect to the north, East
of North is positive.
        azimuth=(hisazimuth-180); %Angle is corrected, positive to the
West from South.
    end
end

```

```

    angulo_incidente=atan(tan(d2r(zenith))*sin(d2r(azimuth)));
%Projection in vertical plane from incident solar ray

    if ite==1|ite==2      %for the xc with negative distance.
        r=r2d(angulo_incidente-atan(yc/-xc(ite))+(pi/2))/2;
%Reflection angle with respect to the horizontal of the planet, positive
looking to the east.

    elseif ite==4|ite==5
        r=r2d(angulo_incidente+atan(yc/xc(ite))-(pi/2))/2;      %r2d
converts radiants to degree.

    elseif ite==3
        r=r2d(angulo_incidente/2);

    end

    if i~=0      % To calculate the error between each r
        error(i)=r-d;
    end

    d=r;

    %Results are written in a file with extension .txt:

    fprintf(archivo(ite), '%5.4f\r\n', r);

    mm=mm+4;      %Increment of 4 minutes

    if mm==60

        hh=hh+1;
        mm=0;
    end
    i=i+1;
end
hh=15; mm=16; ss=0;
i=0;
end
    fprintf('Cambio maximo %g, Cambio minimo
%g\n', max(abs(error)), min(abs(error)));
fclose(archivo(1)); fclose(archivo(2)); fclose(archivo(3));
fclose(archivo(4)); fclose(archivo(5));

```

7.3 Solar beam radiation algorithm

The following algorithm was developed for the purpose of using the Erbs. Correlation to separate the diffuse radiation with the direct radiation.

```

clear all
clc

xc(1)=-0.28; xc(2)=-0.14; xc(3)=0; xc(4)=0.14; xc(5)=0.28; %Distancia
horizontal (m) del centro del colector al centro del reflector (+oeste)
yc=1.65; %Distancia vertical del centro del colector al centro del
reflector

hh=8; mm=0; ss=0; %Hora inicial
c=fix(clock);
i=0; %Numero de iteraciones
zeniths=zeros(120,1);

d=0;
for ite=1:5
    j=0;
    while hh<16

        %Cambiar las siguientes variables para calcular el zenith y azimuto
        %para el dia deseado.

        time.year=c(1); %Año actual
        time.month=10; %Mes actual o dia en el que se tomaron los
datos
        time.day=7; %Dia actual o dia en el que se tomaron los
datos
        time.hour=hh; %Hora
        time.min=mm; %Minuto
        time.sec=ss; %Segundo
        time.UTC=-4; %Correccion de hora con respecto al
Greenwich
        location.latitude=18.21;
        location.longitude=-67.14;
        location.altitude=12; %Con unidades de metros (m)

        sun_position(time, location); %Uso del programa de Reda, I.,
Andreas, A. (2003) para calcular zenith y azimuto actual del Sol
        zenith=ans.zenith;

        j=j+1;
        zeniths(j)=zenith;

        hisazimuth=ans.azimuth; %Este angulo es con respecto al norte,
donde es positivo al este del norte
    end
end

```

```

    azimuth=(hisazimuth-180);    %Es corregido para que el angulo sea con
respecto al sur, positivo al oeste del sur.
    azimuth1(j)=azimuth;
    angulo_incidente=atan(tan(d2r(zenith))*sin(d2r(azimuth))); %angulo
incidente con respecto a un plano horizontal
    angulo_incidente_plano(j,1)=r2d(angulo_incidente);
    %Proyeccion en plano vertical del rayo incidente solar

    if ite==1|ite==2    %Para tomar en cuenta las xc con distancia
negativa
        r=r2d(angulo_incidente-atan(yc/-xc(ite))+(pi/2))/2;    %Angulo
del reflector con respecto a la horizontal del planeta,
        r1(j,ite)=r;
    %positivo mirando hacia el este
        anguloincidente_espejo(j,ite)=r2d(((pi/2)-angulo_incidente-
atan(yc/-xc(ite)))/2); %angulo incidente al espejo

    elseif ite==4|ite==5
        r=r2d(angulo_incidente+atan(yc/xc(ite))-(pi/2))/2;    %r2d
convierte de radianes a grados
        anguloincidente_espejo(j,ite)=r2d(((pi/2)+angulo_incidente-
atan(yc/xc(ite)))/2);
    elseif ite==3
        r=r2d(angulo_incidente/2);
        anguloincidente_espejo(j,ite)=r;
    end

    if i~=0    %Para calcular el error entre cada angulo r subsiguiente
        error(i)=r-d;
    end

    d=r;

    mm=mm+4;    %Aumento en minutos de 4, tener cuidado con este
cambio

    if mm==60    %Si se acumulan 60 minutos de cambio, cambiar la
variable de la hora
        hh=hh+1;
        mm=0;
    end
    i=i+1;
end
hh=8; mm=0';
i=0;
end

%% Este codigo es para calcular el promedio de irradiacion para cada 4
minutos. Hay que estar pendiente de la cantidad de datos que tenga
% el documento, este puede tener datos de cada 10 segundos como por cada
% minuto. El codigo esta hecho para obtener 480 datos, para tener un dato
% cada minuto.

```

```

irradiation_fromeightttofour=xlsread('irradiation_fromeightttofour.xlsx');
%reads the data of irradiation from 8:00:10am to 4pm
count=1;
irradata=0;
irradata2=0;
data=1;

    for sec=1:length(irradiation_fromeightttofour);

        irradata=irradiation_fromeightttofour(sec,1)+irradata;    % suma la
irradiation
        irradata2=irradiation_fromeightttofour(sec,2)+irradata2; % suma la
insolacion
        if count==6; % Como la data es cada 10 segundos, la cantidad de
datos por minuto serian 6.

            irradavg=irradata/6; % divide la irradiacion para sacar un
promedio. Seria un promedio de cada 6 datos.

            irradiation(data,1)=irradavg; % se va formando una matriz del
promedio de irradiacion para un intervalo de tiempo
            insolacion(data,1)=irradata2; % se va formando una matriz de la
insolacion para un intervalo de tiempo
            data=data+1;
            count=1;
            irradata=0;
            irradata2=0;
        else
            count=count+1; % Para contar los datos que se estan sumando. La
cuenta que lleva aqui seria el numero de datos que se sumaria cuando vuelva
al tope del "loop".
        end
    end
    hh
    nn=280; % el numero del dia en que se va a calcular el "clean index".
Es tambien el dia en que la data fue obtenida.
    k_T=clearindex(nn,length(insolacion),insolacion,hh); % Esta funcion es
para calcular el "clear index" usando la ecuacion del capitulo 2.9 del libro
de Duffie.
    % para esta funcion se utiliza la insolacion medida y la insolacion
% extraterrestre (I_o), la cual es calculada.

%% EsteCodigo es para calcular la difusa con la ecuacion utilizada por
Duffie en el capitulo 2.10, ecuaciones de Erbs et al.
title={'time','Insolacion MJ/m^2','I_o MJ/m^2','k_T','Irradiacion medida
kW/m^2','difusa MJ/m^2 (1 minuto)','difusa kW/m^2','Directa
kW/m^2','Irradiacion Total en el Colector W'}; % matriz de los titulos de
las columnas.

I2(2:481,2)=insolacion(:,1); % I2 es la matriz donde se incluye la
insolacion, insolacion extraterrestre calculada, k_T "clean index y otros
(todos los que estan en el 'array' de title).
I_ocalculated=xlsread('I_o.xlsx');

```

```

I2(2:481,3)=I_ocalculated(:,1);
I2(2:481,4)=k_T(:,1);

dif(480,1)=zeros;

for ll=1:480; % 480 minutos desde las 8 am hasta las 4 pm

    if k_T(ll,1)<=0.22
        dif(ll,1)=insolation(ll,1)*(1.0-0.9*k_T(ll,1));

    elseif 0.22< k_T(ll,1)&& k_T(ll,1)<=0.80;
        dif(ll,1)=insolation(ll,1)*(0.9511-
0.1604*k_T(ll,1)+4.388*k_T(ll,1)^2-16.638*k_T(ll,1)^3+12.336*k_T(ll,1)^4);

    else
        dif(ll,1)=insolation(ll,1)*.165;
    end
end
I2(2:481,5)=irradiation;
I2(2:481,6)=dif(:,1);
I2(2:481,7)=(dif(:,1)./60)*10^3; % Se divide la difusa entre 60 (60
segundos) para convertirlo a MW y se multiplica por 10^3 para convertirlo en
kW
I2(2:481,8)=irradiation(:,1)-I2(2:481,7);

%% El proximo codigo es para calcular la irradiacion en el colector
% utilizando data obtenida en el campo, esta puede variar de tiempo.

rho=.8; %reflectividad de los espejos, puede cambiar por espejo.
transmittance=.8; %Glass transmittance
absorptance=.8; % absorber's absorptance
abstrans=transmittance*absorptance*1.01; %transmittance-absorptance product
ll=0;
l=0;
s=0;
for c=1:5;
    for k=1:j;
        for p=1:4; %Since j=120, because the mirrors move every 4 minutes, I
needed this step to account for the full 480 minutes (8am to 4pm). (120 x 4 =
480).2.

            ll=ll+1;
            l=l+1;
            %Don't know which one is the correct one. Book says should be
            %divided by zenith. Students say should be divided by incident
            %angle, which it is the zenith in their plane view.

I_collector(ll,c+1)=(I2(l+1,8)/cosd(angulo_incidente_plano(k,1)))*rho*abstran
s; %Irradiation on collector for each mirror, depending on the data
available

```

```

%I_collector(l1,c+1)=(I2(l+1,8)*cosd((anguloincidente_espejo(k,c)))/cosd(zeniths(k,1)))*rho; %it is either per minute, per 5 minute, per hour, etc.

    end
end
s=l1;
l1=0;
l=0;
end

I_collector(:,1)=I2(2:481,8);

figure(1)
plot(linspace(0,s,s),I_collector)
ylabel(('Radiation (kW/m^2)'), 'FontSize',12)
xlabel(('Time (1=60s)'), 'FontSize',12)
%title('Theoretical Direct on the Collector (kW/m^2)', 'FontSize',12)

figure(2)
plot(linspace(0,s,s),irradiation)

ylabel(('Radiation (kW/m^2)'), 'FontSize',12)
xlabel(('Time (1=60s)'), 'FontSize',12)
%title(('Measured Irradiation from pyranometer (kW/m^2)'), 'FontSize',12)

I_collector_concentrated=I_collector(:,2:6).*1.143*0.13335; % Se multiplica
por el area de los espejos para calcular kW de kW/m^2, Radiacion que caera en
el colector ya que los espejos son mas pequenos que el colector.
I_collector_total=I_collector_concentrated(:,1)+I_collector_concentrated(:,2)
+I_collector_concentrated(:,3)+I_collector_concentrated(:,4)+I_collector_conc
entrated(:,5);
Direct_theoretical(:,2:7)=I_collector; % Es la directa teorica por la razon
de que se utilizan ecuaciones teoricas (incluyendo empiricas)
%para calcular la directa utilizando irradiacion medida por la estacion.
I2(2:481,9)=I_collector_total.*1000;
I3(:,1)=zeniths(:,1);
I3(:,2)=angulo_incidente_plano(:,1);

xlswrite('Direct_theoretical_irradiation.xlsx',Direct_theoretical); % Se
escribe en excel la radiacion directa que recibe el colector por cada espejo.
xlswrite('Diffusion_Calculation.xlsx',I2);
xlswrite('Diffusion_Calculation.xlsx',title);

figure(3)
plot(linspace(0,s,s),I_collector_total)

ylabel(('Irradiation (kW)'), 'FontSize',12)
xlabel(('Time (1=60s)'), 'FontSize',12)
%title(('Total Radiation incident on the Collector (kW)'), 'FontSize',12)

```

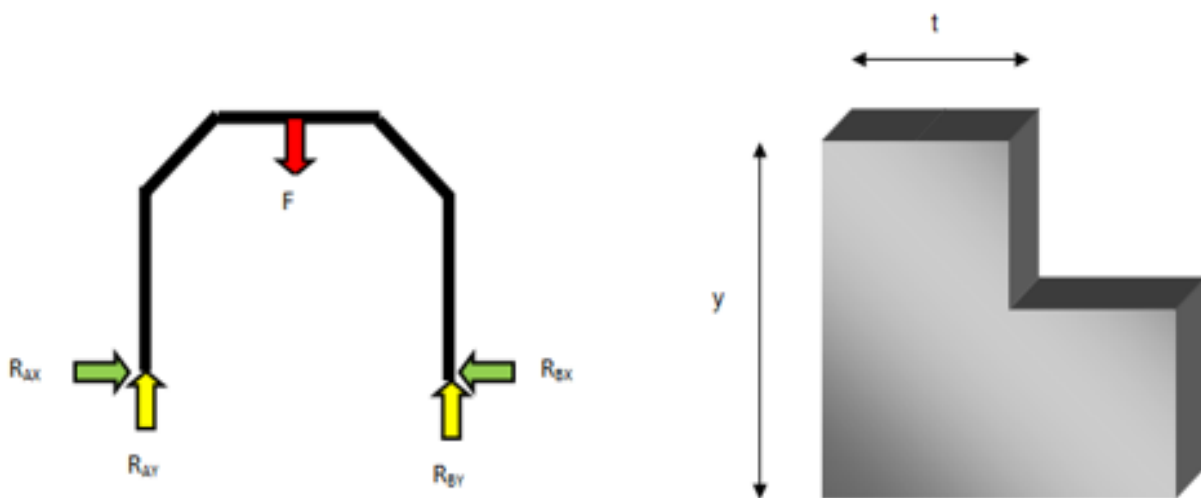
7.4 Bending and Deformation Calculations

These equations were evaluated using MathCad, an engineering tool that simplified the bending and deformation calculations.

Static Equilibrium, Bending, and Deformation Calculations

Calculations

By the free body diagram we have the angle and the lengths of the beams.



$$\alpha := \frac{\pi - 80}{180} \quad h := 197.068 \text{ m}$$

$$l := h \cdot \sin(\alpha) \quad l = 1.94 \text{ m}$$

$$a := \sqrt{h^2 - l^2} \quad a = 0.342 \text{ m}$$

Where h is the hypotenuse and l is the height from the bottom part of the angular beam until the top of the same angular beam.

The following notations are the allowable normal stress (δ) and the allowable shear stress (τ). With these we calculate the maximum Force the structure can hold.

$$\delta_{\text{allow}} := 5.25 \text{ MPa}$$

$$\tau_{\text{allow}} := 0.413 \text{ MPa}$$

$$\delta_{\text{allow}} = 1.275 \times 10^8 \text{ Pa}$$

$$\tau_{\text{allow}} = 5.24 \times 10^7 \text{ Pa}$$

Centroid of the beam

t is equal to the thickness of the L beam and y is the height and the base of the beam, which are 1/16 and 1 inch, respectively. The following calculations are used to calculate the centroid.

$$t := 3.175 \text{ mm}$$

$$y := 25.4 \text{ mm}$$

$$A_1 := t \cdot y$$

$$A_2 := (y - t) \cdot t$$

$$A_1 = 8.064 \times 10^{-5} \text{ m}^2$$

$$A_2 = 7.056 \times 10^{-5} \text{ m}^2$$

$$A_{\text{all}} := A_1 + A_2$$

Y and X are the distance from the y and x axis, respectively, to the centroid of the angular beam "L".

$$Y_1 := \frac{t(y^2 + ty - t^2)}{2 \cdot A_{\text{all}}}$$

$$X_1 := \frac{t(ty + y^2 - t^2)}{2 \cdot A_{\text{all}}}$$

$$Y_1 = 7.514 \times 10^{-3} \text{ m}$$

$$X_1 = 7.514 \times 10^{-3} \text{ m}$$

Next the moment of Inertia is calculated

$$I_1 := t \cdot \frac{y^3}{12}$$

$$I_2 := (y - t) \cdot \frac{t^3}{12}$$

$$I_{c1} := I_1 + A_1 \left[\left(\frac{y}{2} \right) - Y_1 \right]^2$$

$$I_{c2} := I_2 + A_2 \left(Y_1 - \frac{t}{2} \right)^2$$

$$I_{c1} = 6.505 \times 10^{-9} \text{ m}^4$$

$$I_{c2} = 2.538 \times 10^{-9} \text{ m}^4$$

$$I := I_{c1} + I_{c2}$$

$$y = 0.025 \text{ m}$$

C_c is the perpendicular distance from the neutral axis to a point farthest away from the neutral axis.

$$I = 9.042 \times 10^{-9} \text{ m}^4 \quad c_c := y - Y_1$$

$$c_c = 0.018 \text{ m}$$

The maximum force the beam can hold is calculated by calculating the reaction forces by using a free body diagram and the allowable normal and shear stresses.

Forces

$$M_D := \delta_{\text{allow}} \frac{I}{c_c} \quad M_D = 64.45 \text{ N}$$

$$R_{ay} := \frac{M_D}{\cos(\alpha) \cdot h} \quad Q := t(y^2 + t \cdot y - t^2)$$

$$R_{ay} = 188.36 \text{ N}$$

$$F := 2 \cdot R_{ay}$$

$$V_D := R_{ay} \cdot \cos(\alpha)$$

$$W_{\text{allow}} := \frac{F}{9.31 \frac{\text{m}}{\text{s}^2}}$$

$$W_{\text{allow}} = 40.46 \text{ kg}$$

$$V_D = 32.70 \text{ N}$$

$$W_{\text{allow}} := \frac{W_{\text{allow}}}{1 \text{ beam}}$$

$$1 \text{ beam} = 0.454 \text{ kg}$$

$$\tau_1 := V_D \frac{Q}{I \cdot t}$$

$$\tau_1 = 2.589 \times 10^6 \text{ Pa}$$

$$W_{\text{allow}} = 89.21$$

Weight allowed is 89.21 lb per beam.

7.5 EES equations

knowns

$$L = 0.015 \text{ [m]}$$

$$L_{in1} = 0.02286 \text{ [m]} \text{ length in duct 1}$$

$$\text{width1} = 0.02286 \text{ [m]} \text{ duct width for fluid flow}$$

$$CL_{bottom} = 1.143 \text{ [m]} \quad LL = 1.1938 \text{ [m]} \text{ Critical Length for wind coefficient for the bottom of the collector} \quad \text{length of collector}$$

$$CL_{top} = LL \text{ Critical Length for wind coefficient for the top of the collector}$$

$$A_{ff} = L_{in1} \cdot \text{width1} \text{ Area of fluid flow}$$

$$A_m = 0.1397 \text{ [m]} \cdot 1.143 \text{ [m]} \text{ Area of Mirrors, in order to calculate real } q$$

$$A_c = 6 \cdot (\text{width1} + 0.00254 \text{ [m]}) \cdot LL \text{ Area of Collector}$$

$$A_g = CL_{bottom} \cdot (6 \cdot (\text{width1} + 2 \cdot 0.00254) + 2 \cdot 0.0254 \text{ [m]}) \text{ Area of glass}$$

$$A_{oc} = (6 \cdot (\text{width1} + 2 \cdot 0.00254 \text{ [m]}) + 2 \cdot 0.0254 \text{ [m]}) \cdot LL \text{ Area of Collector, including insulation}$$

$$A_{qconv} = 6 \cdot 2 \cdot (\text{width1} + L_{in1}) \cdot LL \text{ Heat Transfer Area inside the Duct}$$

$$A_s = LL \cdot 0.0454 \text{ [m]} \text{ Area of the side of the collector (all the collector, wooden part), height x length}$$

$$L_s = 0.02286 \text{ [m]} \text{ Height of sides of the channels of the tube}$$

$$A_{sp} = (0.00254 + L_s) \cdot LL \text{ Area of the side of the aluminum tubes}$$

$$A_{ch} = \text{width1} \cdot LL$$

$$vel_{in} = \frac{\frac{\dot{m}}{6}}{\rho_f \cdot A_{ff}}$$

$$\dot{V} = \frac{\dot{m}}{6 \cdot \rho_f}$$

Temperatures and Solar Radiation

$$T_a = 305.15 \text{ [K]}$$

$$T_f = 305.15 \text{ [K]}$$

$S = 650$ [W] irradiation (W) coming from the mirrors

$S_{1\text{flux}} = \frac{S}{A_c}$ Solar irradiation on the collector, these sets of equation are done since the mirrors are smaller than the collector and it is not incident in all the collector

$C_{p\text{f1}} = C_p$ (Air , $T=T_{mf}$)

$\epsilon_p = 0.95$ $\epsilon_g = 0.9$

$\sigma = 5.670\text{E}-08$ [W/m²-K⁴]

$k_p = 237$ [W/(m²K)] conductivity of the plate

$L_e = 0.0254 \cdot 1$ [m] edge thickness

$L_w = 0.0254 \cdot 1$ [m] Length of back of collector, wood

$Q_{\text{back}} = \frac{k_w}{L_w} \cdot (T_p - T_w)$ heatloss through the back of the collector

$Q_{\text{back}} = U_b \cdot (T_p - T_a)$

$Q_{\text{sides}} = \frac{k_w}{L_w} \cdot (T_p - T_{ws})$

$Q_{\text{sides}} = U_{\text{sides}} \cdot (T_p - T_a)$

$Q_{\text{top}} = \sigma \cdot \epsilon_g \cdot (T_g^4 - T_a^4) + h_{\text{wbot}} \cdot (T_g - T_a)$

$Q_{\text{top}} = U_{\text{top}} \cdot (T_p - T_a)$

$U_L = U_{\text{top}} + U_b + 2 \cdot U_{\text{sides}}$ Overall heatloss

T_m between plate and cover

$T_{mc} = \frac{T_p + T_g}{2}$

$T_{mf} = T_f + \frac{Q_u}{F_R \cdot U_L} \cdot (1 - f_2)$

Mean Plate Temperature, Duffie Equation

$T_{mp} = T_f + \frac{Q_u}{F_R \cdot U_L} \cdot (1 - F_R)$

Convection on top and bottom Collector

$vel = 2$ [m/s]

$Re\#_{\text{wtop}} = vel \cdot \frac{CL_{\text{top}}}{\text{viscosity}_w}$

$Nu\#_{\text{wtop}} = 0.664 \cdot Re\#_{\text{wtop}}^{0.5} \cdot Pr_w^{(1/3)}$ $Nu\#_{\text{wtop}} = h_{\text{wtop}} \cdot \frac{CL_{\text{top}}}{k_a}$

$Re\#_{\text{wbot}} = vel \cdot \frac{CL_{\text{bottom}}}{\text{viscosity}_w}$

$Nu\#_{\text{wbot}} = 0.664 \cdot Re\#_{\text{wbot}}^{0.5} \cdot Pr_w^{(1/3)}$ $Nu\#_{\text{wbot}} = h_{\text{wbot}} \cdot \frac{CL_{\text{bottom}}}{k_a}$

$Pr_w = Pr$ (Air , $T=T_a$) $dyn_w = Visc$ (Air , $T=T_a$) $k_a = k$ (Air , $T=T_a$)

$\rho_w = \rho$ (Air , $T=T_a$, $P = 101.32501$ [kPa]) $\text{viscosity}_w = \frac{dyn_w}{\rho_w}$

$g = 9.807$ [m/s²]

$dyn_{f1} = Visc$ (Air , $T=T_{mf}$) $k_{\text{airf1}} = k$ (Air , $T=T_{mf}$)

$Pr_{f1} = Pr$ (Air , $T=T_{mf}$) $\rho_f = \rho$ (Air , $T=T_{mf}$, $P = 101.32501$ [kPa])

7.6 Input Values for EES and Star CCM+ Simulation

Unit Settings: SI K kPa J mass deg

(Fiberglass Wool Insulation, Run 100)

$\alpha_{nc} = 0.00002514$ [W·m ² /J]	$A_b = 0.1637$ [m ²]	$A_c = 0.1819$ [m ²]	$A_{cc} = 0.2426$ [m ²]	$A_{ch} = 0.02729$ [m ²]
$A_{f1} = 0.0005226$ [m ²]	$A_g = 0.2323$	$A_m = 0.1597$ [m ²]	$A_{qconv} = 0.655$ [m ²]	$A_s = 0.0542$ [m ²]
$A_{sf} = 0.02729$ [m ²]	$A_{sp} = 0.03032$	$A_t = 0.3275$ [m ²]	$\beta = 0$ [deg]	$CL_{bottom} = 1.143$ [m]
$CL_{top} = 1.194$ [m]	$C_{pf1} = 1006$ [J/kg·K]	$C_{p,nc} = 1006$ [J/kg·K]	$\Delta P = 0.03179$ [kPa]	$dynf1 = 0.00001937$ [kg/m·s]
$dyn_{nc} = 0.00001971$ [kg/m·s]	$dyn_w = 0.00001881$ [kg/m·s]	$\epsilon_g = 0.9$	$\epsilon_p = 0.95$	$\epsilon_w = 0.75$
$\eta = 0.9839$	$\eta_o = 0.9919$	$f = 0.03578$	$f1 = 0.8176$	$f2 = 0.8386$
$F_R = 0.6856$	$g = 9.807$ [m/s ²]	$h_H = 28.4$ [W/m ² ·K]	$h_{nc} = 1.832$	$h_T = 28.4$ [W/m ² ·K]
$h_{wbot} = 5.096$	$h_{wtop} = 4.987$	$k_a = 0.02603$ [W/m·K]	$k_{airf1} = 0.02693$ [W/m·K]	$k_{air,nc} = 0.02748$ [W/m·K]
$k_p = 237$ [W/(m·K)]	$k_w = 2.365$ [W/m·K]	$L = 0.015$ [m]	$Le = 0.0254$ [m]	$LL = 1.194$ [m]
$L_{in1} = 0.02286$ [m]	$L_s = 0.02286$ [m]	$L_w = 0.0254$ [m]	$\dot{m} = 0.01929$ [kg/s]	$N = 6$
$Nu_{nc} = 1$ [m]	$Nu_{wbot} = 223.8$ [m ² ·K/W]	$Nu_{wtop} = 228.7$ [m ² ·K/W]	$Nusselt_T = 24.11$	$Pr_{f1} = 0.7235$
$Pr_{nc} = 0.7217$	$Pr_w = 0.7264$	$q_1 = 531.4$ [W]	$q_{back} = 349$ [K]	$q_{convection} = 531.4$ [W]
$q_{sides} = 446.9$ [K]	$q_{top} = 120.5$ [K]	$Q_u = 445.7$ [W]	$Ra = 4030$ [m ⁴ /s ²]	$Re = 7260$
$Re_{wbot} = 140570$	$Re_{wtop} = 146817$	$RelRough = 0$	$pr = 1.112$ [kg/m ³]	$\rho_{nc} = 1.086$ [kg/m ³]
$\rho_w = 1.157$ [kg/m ³]	$S = 650$ [W]	$S1_{flux} = 3573$ [W/m ²]	$S1_{irradiation} = 4071$ [W/m ²]	$\sigma = 5.670E-08$ [W/m ² ·K ⁴]
$th = 0.00254$ [m]	$T_a = 305.2$ [K]	$T_f = 305.2$ [K]	$T_g = 315.9$ [K]	$T_{mc} = 324.9$ [K]
$T_{mf} = 317.3$ [K]	$T_{mp} = 328.9$ [K]	$T_o = 328.1$ [K]	$T_{oC} = 54.97$ [C]	$T_{oF} = 131$ [F]
$T_p = 333.9$ [K]	$T_{pC} = 60.8$ [C]	$T_{pF} = 141.4$ [F]	$T_{pmC} = 55.72$ [C]	$T_{pmF} = 132.3$ [F]
$T_w = 330.2$ [K]	$T_{ws} = 329.1$ [K]	$U_b = 12.12$	$U_L = 47.34$	$U_{sides} = 15.52$
$U_{top} = 4.184$	$vel = 2$ [m/s]	$vel_{in} = 5.53$ [m/s]	$viscosity_{nc} = 0.00001815$ [m ² /s]	$viscosity_w = 0.00001626$ [m ² /s]
$\dot{V} = 0.00289$ [m ³ /s]	$width1 = 0.02286$ [m]			

VIII. References

- [1] R. Borkhataria, J. A. Collazo, M. J. Groom, and A. Jordan-Garcia, "Shade-grown coffee in Puerto Rico: Opportunities to preserve biodiversity while reinvigorating a struggling agricultural commodity," *Agriculture, Ecosystems & Environment*, vol. 149, pp. 164–170, Mar. 2012.
- [2] "Diseño de un equipo para secado mecánico de café," *Scribd*. [Online]. Available: <http://www.scribd.com/doc/62339679/Diseno-de-un-equipo-para-secado-mecanico-de-cafe>. [Accessed: 17-Aug-2012].
- [3] A. Sharma, C. R. Chen, and N. Vu Lan, "Solar-energy drying systems: A review," *Renewable and Sustainable Energy Reviews*, vol. 13, no. 6–7, pp. 1185–1210, Aug. 2009.
- [4] J. Muñoz, J. M. Martínez-Val, and A. Ramos, "Thermal regimes in solar-thermal linear collectors," *Solar Energy*, vol. 85, no. 5, pp. 857–870, May 2011.
- [5] F. P. Incropera and D. P. DeWitt, *Fundamentals of heat and mass transfer*. John Wiley & Sons, Inc., 2007.
- [6] Dictionary.com, "solar energy," *The American Heritage® Science Dictionary*. Houghton Mifflin Company, 01-Oct-2014.
- [7] J. A. Duffie and W. A. Beckman, *Solar Engineering of Thermal Processes*, 3rd ed. Hoboken, New Jersey: John Wiley & Sons, Inc., 2006.
- [8] J. D. Pye, "System modeling of the Compact Linear Fresnel Reflector," Doctor of Philosophy, University of South Wales, Sydney, Australia, 2008.
- [9] D. R. Mills and G. L. Morrison, "Compact Linear Fresnel Reflector Solar Thermal Power Plants," *Solar Energy*, vol. 68, no. 3, pp. 263–283, Mar. 2000.
- [10] P. L. Singh, S. Ganesan, and G. C. Yàdav, "Technical note: Performance study of a linear Fresnel concentrating solar device," *Renewable Energy*, vol. 18, no. 3, pp. 409–416, Nov. 1999.
- [11] P. L. Singh, R. M. Sarviya, and J. L. Bhagoria, "Thermal performance of linear Fresnel reflecting solar concentrator with trapezoidal cavity absorbers," *Applied Energy*, vol. 87, no. 2, pp. 541–550, Feb. 2010.
- [12] C. J. Dey, "Heat transfer aspects of an elevated linear absorber," *Solar Energy*, vol. 76, no. 1–3, pp. 243–249, Mar. 2004.
- [13] J. D. Nixon and P. A. Davies, "Cost-exergy optimisation of linear Fresnel reflectors," *Solar Energy* (2011).
- [14] N. Velázquez, O. García-Valladares, D. Saucedo, and R. Beltrán, "Numerical simulation of a Linear Fresnel Reflector Concentrator used as direct generator in a Solar-GAX cycle," *Energy Conversion and Management*, vol. 51, no. 3, pp. 434–445, Mar. 2010.

- [15] G. Morin, J. Dersch, W. Platzer, M. Eck, and A. Häberle, “Comparison of Linear Fresnel and Parabolic Trough Collector power plants,” *Solar Energy*, vol. 86, no. 1, pp. 1–12, Jan. 2012.
- [16] J. T. Holmes, D. J. Alpert, T. R. Mancini, L. M. Murphy, and P. O. Schissel, “Development of concentrating collectors for solar thermal systems,” in *Energy Conversion Engineering Conference, 1989. IECEC-89., Proceedings of the 24th Intersociety*, 1989, pp. 1971–1978 vol.4.
- [17] A. Häberle, C. Zahler, H. Lerchenmuller, M. Mertins, C. Wittwer, F. Trieb, and J. Dersch, “The Solarmundo line focussing Fresnel collector. Optical and thermal performance and cost calculations.,” presented at the International SolarPACES Symposium, Zurich, Switzerland, 2002.
- [18] J. D. Pye, G. L. Morrison, P. L. Lievre, and M. Behnia, “Steam-circuit Model for the Compact Linear Fresnel Reflector Prototype,” in *ANZSES Solar 2004*, Perth, 2004.
- [19] F. J. Pino, R. Caro, F. Rosa, and J. Guerra, “Experimental validation of an optical and thermal model of a linear Fresnel collector system,” *Applied Thermal Engineering*.
- [20] R. Abbas, J. Muñoz, and J. M. Martínez-Val, “Steady-state thermal analysis of an innovative receiver for linear Fresnel reflectors,” *Applied Energy*, vol. 92, pp. 503–515, Apr. 2012.
- [21] W. M. Rohsenow, J. P. Hartnett, and Y. I. Cho, *Handbook of heat transfer*. McGraw-Hill, 1998.
- [22] R. Siegel and J. R. Howell, *Thermal radiation heat transfer*. Taylor & Francis, 2002.
- [23] “sun_position.m - File Exchange - MATLAB Central.” [Online]. Available: <http://www.mathworks.com/matlabcentral/fileexchange/4605-sun-position-m>. [Accessed: 07-Sep-2014].
- [24] I. Reda and A. Andreas, “Solar position algorithm for solar radiation applications,” *Solar Energy*, vol. 76, no. 5, pp. 577–589, 2004.
- [25] B. Y. H. Liu and R. C. Jordan, “The interrelationship and characteristic distribution of direct, diffuse, and total solar radiation,” *Solar Energy*, vol. 4, no. 3, pp. 1–19, 1960.
- [26] F. Lanini, “Division of Global Radiation into Direct Radiation and Diffuse Radiation,” Master’s Thesis, University of Bern, 2010.
- [27] D. G. Erbs, S. A. Klein, and J. A. Duffie, “Estimation of the diffuse radiation fraction for hourly, daily and monthly-average global radiation,” *Solar Energy*, vol. 28, no. 4, pp. 293–302, 1982.
- [28] J. F. Orgill and K. G. T. Hollands, “Correlation equation for hourly diffuse radiation on a horizontal surface,” *Solar Energy*, vol. 19, no. 4, pp. 357–359, 1977.
- [29] D. T. Reindl, W. A. Beckman, and J. A. Duffie, “Diffuse Fraction Correlations,” *Solar Energy*, vol. 45, no. 1, pp. 1–7, 1990.
- [30] R. J. Bonilla Alicea, “Reynolds Averaged and Large Eddy Simulations of the Turbulent Flow in a Channel with Inclined and V-Shaped Turbulators on the Walls,” Master’s Thesis, University of Puerto Rico - Mayaguez Campus, Mayaguez, 2012.
- [31] H. K. Versteeg and W. Malalasekera, *An introduction to computational Fluid Dynamics. The Finite Volume Method*, Second. Pearson Prentice Hall, 2007.

- [32]P. L. Singh, R. M. Sarviya, and J. L. Bhagoria, "Heat loss study of trapezoidal cavity absorbers for linear solar concentrating collector," *Energy Conversion and Management*, vol. 51, no. 2, pp. 329–337, Feb. 2010.
- [33]C. Choudhury and H. K. Sehgal, "A fresnel strip reflector-concentrator for tubular solar-energy collectors," *Applied Energy*, vol. 23, no. 2, pp. 143–154, 1986.
- [34]D. J. Reynolds, M. J. Jance, M. Behnia, and G. L. Morrison, "An experimental and computational study of the heat loss characteristics of a trapezoidal cavity absorber," *Solar Energy*, vol. 76, no. 1–3, pp. 229–234, Jan. 2004.
- [35]J. Facão and A. C. Oliveira, "Numerical Simulation of a Trapezoidal Cavity Receiver for a Linear Fresnel Solar Collector Concentrator," *Renewable Energy*, vol. 36, no. 1, pp. 90–96, Jan. 2011.
- [36]A. Hobbi and K. Siddiqui, "Experimental study on the effect of heat transfer enhancement devices in flat-plate solar collectors," *International Journal of Heat and Mass Transfer*, vol. 52, no. 19–20, pp. 4650–4658, Sep. 2009.
- [37]F. . Forson, M. A. . Nazha, and H. Rajakaruna, "Experimental and simulation studies on a single pass, double duct solar air heater," *Energy Conversion and Management*, vol. 44, no. 8, pp. 1209–1227, May 2003.
- [38]D. R. Pangavhane, R. L. Sawhney, and P. N. Sarsavadia, "Design, development and performance testing of a new natural convection solar dryer," *Energy*, no. 27, pp. 579–590, 2002.
- [39]H. M. Yeh and J. Z. Ho, "Collector efficiency of double-flow solar air heaters with fins attached.," *Energy*, vol. 27, no. 1, pp. 715–727, 2002.
- [40]S. Chamoli, R. Chauhan, N. S. Thakur, and J. S. Saini, "A review of the performance of double pass solar air heater," *Renewable and Sustainable Energy Reviews*, vol. 16, no. 1, pp. 481–492, Jan. 2012.
- [41]M. K. Gupta and S. C. Kaushik, "Performance evaluation of solar air heater for various artificial roughness geometries based on energy, effective and exergy efficiencies.," *Renewable Energy*, vol. 34, no. 1, pp. 465–476, 2009.
- [42]M. K. Mittal, Varun, R. P. Saini, and S. K. Singal, "Effective efficiency of solar air heaters having different types of roughness elements on the absorber plate," *Energy*, vol. 32, no. 1, pp. 739–745, 2007.
- [43]B. Bhushan and R. Singh, "A review on methodology of artificial roughness used in duct of solar air heaters," *Energy*, vol. 35, no. 1, pp. 202–212, 2010.
- [44]R. Tchinda, "A review of the mathematical models for predicting solar air heater systems," *Renewable and Sustainable Energy Reviews*, vol. 13, pp. 1734–1759, 2009.
- [45]S. R. Dhariwal and S. R. Mirdha, "Analytical expressions for the response of flat-plate collector to various transient conditions," *Energy Conversion and Management*, vol. 46, pp. 1809–1836, 2005.
- [46]A. Rivera Jimenez and C. J. Correa Torres, "Diseño de un sistema lineal Fresnel," Departamento de Ingeniería Eléctrica, Universidad de Puerto Rico Recinto de Mayaguez, Investigación Subgraduada, Aug. 2010.

- [47] V. P. Nicolau and F. P. Maluf, "Determination of Radiative Properties of Commercial Glass," presented at the The 18th Conference on Passive and Low Energy Architecture, Florianopolis, Brazil, 2001.
- [48] F. Giovannetti, S. Foste, N. Ehrmann, and G. Rockendorf, "High transmittance, low emissivity glass covers for flat plate collectors: Applications and performance," *Solar Energy*, vol. 104, pp. 52–59, 2014.